CURRENT DISTRIBUTION AND METAL FLOW

IN AN

ELECTRIC ARC FURNACE

CURRENT DISTRIBUTION AND METAL FLOW IN AN ELECTRIC ARC FURNACE

by

MILTON MARLBOROUGH MUNROE, B.A.Sc.

A Thesis

Submitted to the Faculty of Graduate Studies

in Partial Fulfilment of the Requirements

for the Degree

Master of Engineering

McMaster University

March 1972

MASTER OF ENGINEERING (1972)
(Electrical Engineering)

McMASTER UNIVERSITY
Hamilton, Ontario

TITLE: Current Distribution and Metal Flow in an Electric Arc Furnace

AUTHOR: Milton Marlborough Munroe, B.A.Sc. (University of Toronto)

SUPERVISOR: Dr. R.T.H. Alden

NUMBER OF PAGES: 139, X

SCOPE AND CONTENTS:

Current Distribution and Metal Flow in the crucible of an Electric Arc Furnace is investigated using a small-scale, three dimensional model. Results obtained indicate that current distribution for furnaces of different sizes and ratings may be predicted using one model. Naturally occurring metal flow is shown to be related to phase rotation of the supply voltage. A two-phase, four-electrode design is proposed as an alternative to the present three-phase, three-electrode design.

ACKNOWLEDGEMENTS

I would like to express my sincere thanks to Dr. R.T.H. Alden for suggesting and supervising the topic.

I am also grateful to Dr. D.A.R. Kay and Mr. M. Ghosh of the Metallurgy Department for the many discussions on the metallurgical aspects of the subject.

The assistance and helpful suggestions given by Mr. Blythe Williams and the staff of the Electrical Engineering Workshop in the construction of the apparatus for this project is gratefully acknowledged.

TABLE OF CONTENTS

LIST OF FIGURES

LIST OF TABLES

CHAPTER 1

THE ELECTRIC ARC FURNACE

1.1 INTRODUCTION

The electric arc is a source of heat with a controllable concentration of energy that is not found in conventional melting processes. Power densities in the range of 1500 kW per cubic inch (91.5 kW per cubic centimetre), combined with a thermal potential of about 4000°C, go a long way towards making the electric arc an ideal source for melting metals. These properties are utilised in the Electric Arc Furnace, as used in steel production, and also in the melting of such non-ferrous metals as copper and brass.

The main raw material in electric furnace steelmaking is scrap iron and steel. The major advantage of the arc furnace is that the composition of the final product can be almost completely controlled by use of a suitable slag. Slags are substances, (e.g. oxides, carbonates), which on account of their fusibility, chemical activity, dissolving power and low density, furnish the means by which impurities are separated from the metal and removed from the furnace (2). This gives the electric arc furnace such flexibility over all other furnaces, that with it, one may proceed to make the best grade of steel from almost the worst grade of scrap. Further, as

an all-electric device, its operation is more easily controlled directly by a computer (1). At the present time, electric furnace steel accounts for only a small percentage (14% in the U.S.) of the total supply. However, as indicated in Table 1.1, this figure is steadily rising (2).

1.2 HISTORY AND DEVELOPMENT OF THE ELECTRIC ARC FURNACE

Though the phenomenon of the electric arc was first studied scientifically by Sir Humphrey Davey in 1800, the electric arc furnace had its origin in 1878, when William Siemens first applied an electric current to the melting of steel (2).

In the Siemens model, two horizontal carbon electrodes inserted through the furnace walls above the crucible melted the charge by radiation from the horizontal arc. This design was very wasteful in electric energy as the furnace walls were also consumed at the same time.

In 1892 De Laval patented a furnace for refining iron, but this proved impracticable. In about the same period, Héroult developed an electric furnace for the manufacture of ferro-alloy and calcium carbide (3, 4).

Another furnace was invented in 1898 by Stassano. This was

TABLE 1.1

ANNUAL PRODUCTION OF ELECTRIC-FURNACE STEELS[1]

(Raw Steel and Steel for Castings - Thousands of Net Tons)[2]

Year	Electric-Furnace Steel	Total All Processes, Including Electric	Percentage Represented by Electric-Furnace Steel	Year	Electric-Furnace Steel	Total All Processes, Including Electric	Percentage Represented by Electric-Furnace Steel
1969	20,132	141,262	14.3	1952	6,798	93,168	7.3
1968	16,814	131,462	12.8	1951	7,142	105,200	6.8
1967	15,089	127,213	11.9	1950	6,039	96,836	6.2
1966	14,870	134,101	11.1	1949	3,783	77,978	4.9
1965	13,804	131,462	10.5	1948	5,057	88,640	5.7
1964	12,678	127,076	10.0	1947	3,788	84,894	4.5
1963	10,920	109,261	10.0	1946	2,563	66,603	3.8
1962	9,013	98,328	9.2	1945	3,457	79,702	4.4
1961	8,664	98,014	8.8	1944	4,238	89,642	4.7
1960	8,379	99,282	8.4	1943	4,589	88,837	5.2
1959	8,533	93,446	9.1	1942	3,975	86,032	4.6
1958	6,656	85,255	7.8	1941	2,869	82,839	3.5
1957	7,971	112,715	7.1	1940	1,700	66,983	2.5
1956	8,641	115,216	7.5	1939	1,029	52,799	1.9
1955	8,050	117,036	6.9	1938	566	31,752	1.8
1954	5,436	88,312	6.2	1937	947	56,637	1.7
1953	7,280	111,610	6.5	1936	865	53,500	1.1
				1935	606	38,184	1.6

[1] From Annual Reports of American Iron and Steel Institute.

[2] The figures include only that portion of the capacity and production of steel for castings used by foundries which were operated by companies also producing raw steel for subsequent processing into wrought-steel products.

so constructed that it could be rocked slightly to agitate the bath, and was heated by arcs from horizontal electrodes (3).

In 1900, Héroult made changes to his furnace to adapt it to the melting of steel, and in 1904 installed the first single phase electric steel furnace in the United States.

Girod (3) produced a furnace in 1904, with a conducting bottom acting as one electrode.

Lindblad of Sweden in 1910, invented a furnace having two or more electrodes at the top and one in the bottom, the circuit being made through the heated refractory (3).

Nathusius (3, 4) put a furnace in operation in 1911, operating on three phases, each phase connected to a vertical top electrode and a bottom electrode.

Rennerfelt (3) in 1912 developed a design operating on two phases, with two inclined electrodes, and one vertical between them to force the arc downwards against the bath.

In 1915, Greaves and Etchells (3) introduced a furnace using three phase currents, with two phases entering through vertical top electrodes, and the third through a bottom electrode, the resistance of the hot refractory bottom being used to generate heat.

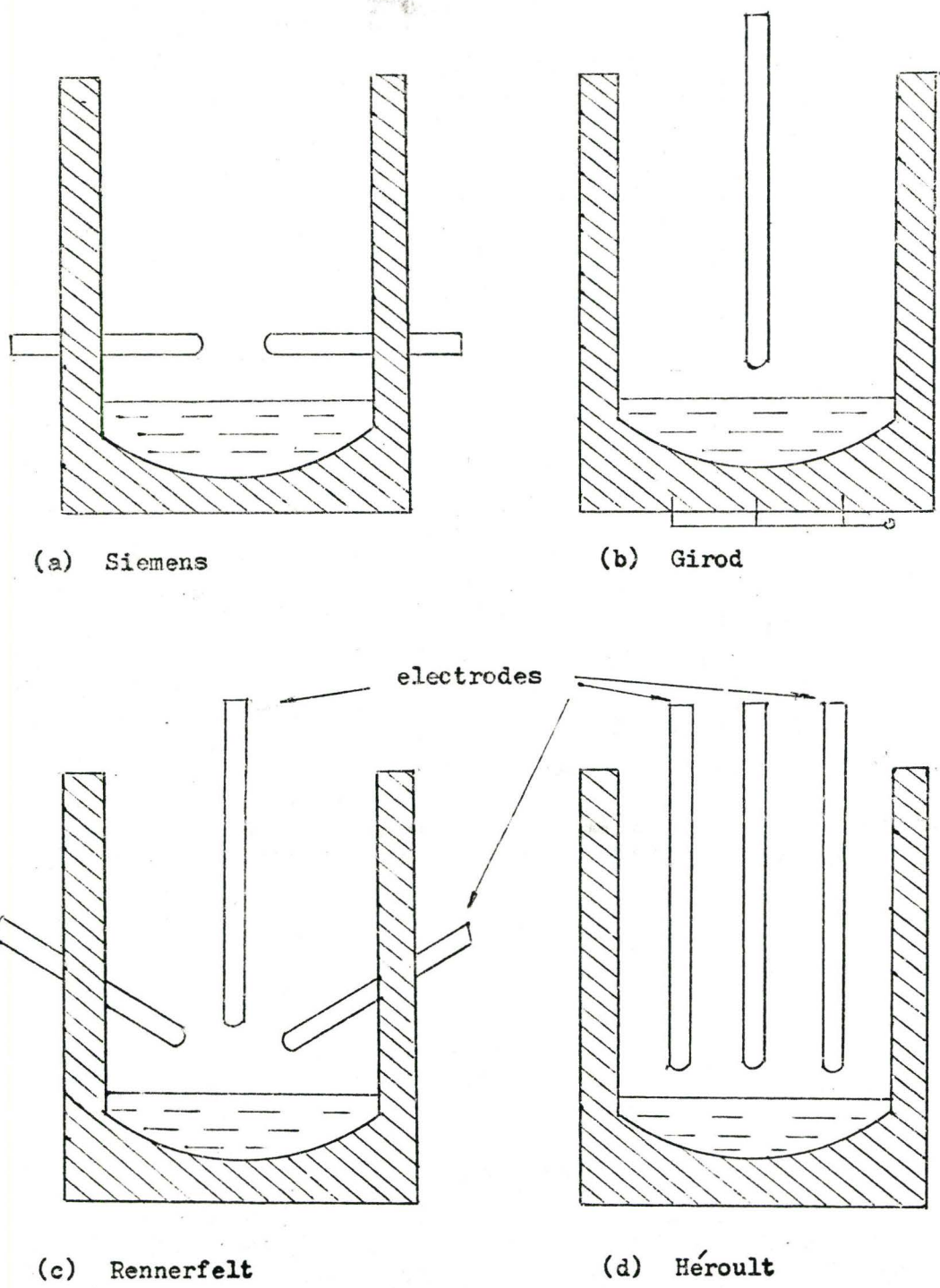

Fig. 1.1: Early Designs of the Electric Arc Furnace

Of the many designs, only the three-phase Héroult furnace has stood the test of time, and evolved as a steel producing tool comparable to any other.

Fig. 1.1 shows some of the many configurations of the early electric arc furnace.

1.3 OPERATION AND CONTROL OF THE ELECTRIC ARC FURNACE

As a result of technological progress, better time utilisation and improved refractories, the electric arc furnace has made striking progress in the last decade 1960 - 1970. In the early 50's, the advent of the basic oxygen process and the use of oxygen in the open hearth with productivity rates of upwards of 200 tons per hr made electric furnace figures look rather poor. The new concept of Ultra High Power (U.H.P.), introduced in 1964 by W.E. Schwabe (4) and associates, greatly increased productivity of electric furnace steelmaking.

The basic idea of U.H.P. operation was to increase the power input to the furnace. This is coupled with better time utilisation and careful scheduling of materials and services. Table 1.2 gives a chronological evaluation of a 150-ton electric arc furnace (6).

As explained above, the design of the modern electric arc

TABLE 1.2

CHRONOLOGICAL EVALUATION OF A 150-TON ELECTRIC ARC FURNACE

Period	Transformer Rating MVA	Power Input MW	Power Factor	Kilowatt Hours per Ton	Tons per Hr	Tons per Day	Changes in Operation
1956	25	17	0.80+	550	27	650	Increased time utilisation
1957	25	20	0.75	550	31	750	New Powerline
1958	25	23	0.75	500	35	850	Power factor reduced
1959/64	48	34	0.70	490	46	1100	Addition of water cooled cables and 48 MVA transformer
1964/66	80	52	0.68	480	58	1400	New 80 MVA transformer
1968	80	52	0.64	480	63	1500+	Increased power demand and low power factor

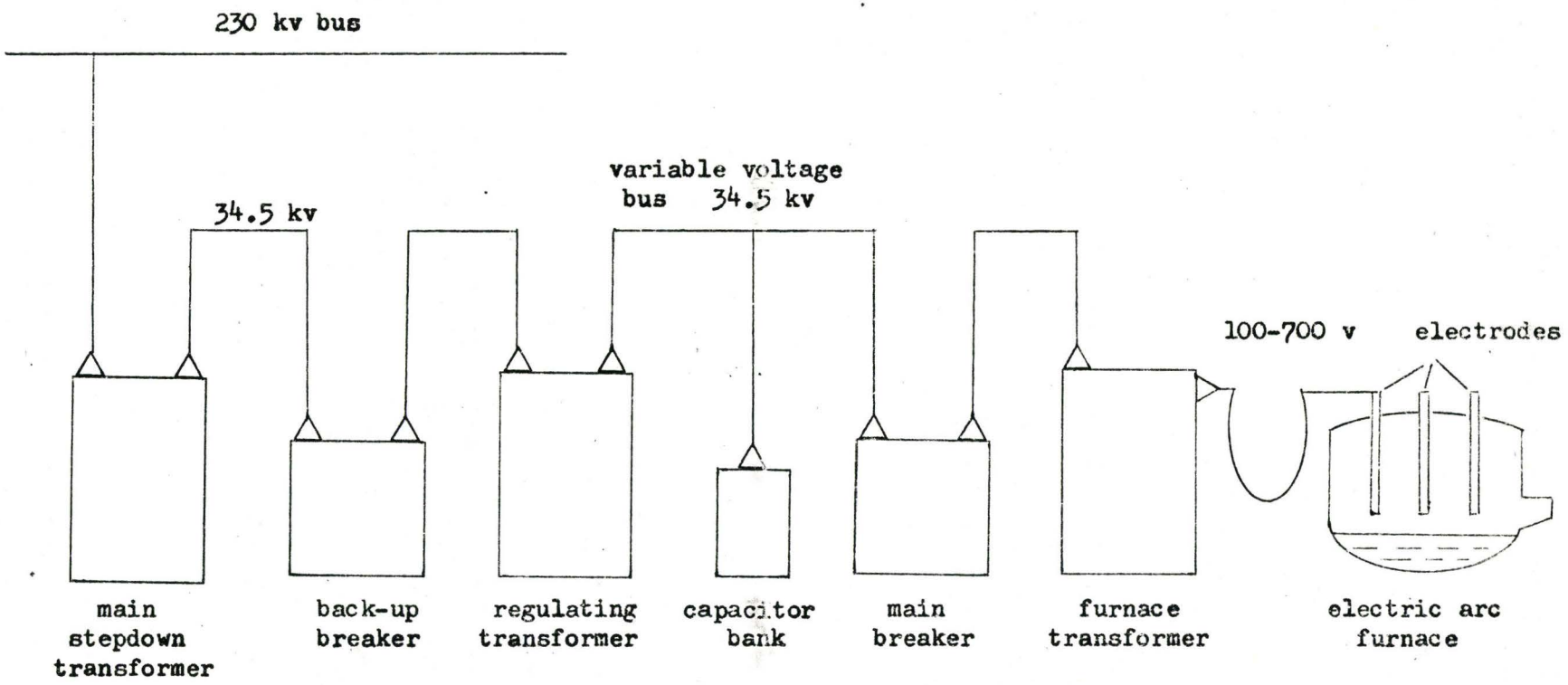

Fig. 1.2: Electrical Supply System of an Electric Arc Furnace

furnace is exclusively Héroult, and has remained basically unchanged since its inception. The principle of operation is rather simple. The furnace is charged with scrap iron and steel, and an electric arc is struck between the carbon electrodes and the charge. The electrodes bore down into the scrap, melting it from the bottom up by radiation. During this meltdown period, the sidewalls are shielded from the destructive radiation and are not as quickly consumed as in the previous designs. For efficient radiation of arc heat, the furnace is operated on a long arc during this meltdown phase.

After meltdown, when the walls are clear of scrap, the arc length and power are reduced to minimise the formation of 'hot spots'. These are extremely worn areas caused by the prolonged exposure of the sidewalls to the arc after meltdown and appear where the sidewall is nearest to the arc.

Refining of the molten metal then takes place under an appropriate slag. It is the controllability of slag in the electric arc furnace that sets the process apart from the other conventional methods (2). Whereas, in the induction furnace, and other methods of steelmaking, the composition of the finished product is dependent on careful selection of raw materials, in the arc furnace this is done by slag control. The slag may be made oxidising or reducing as desired to remove selected impurities (2).

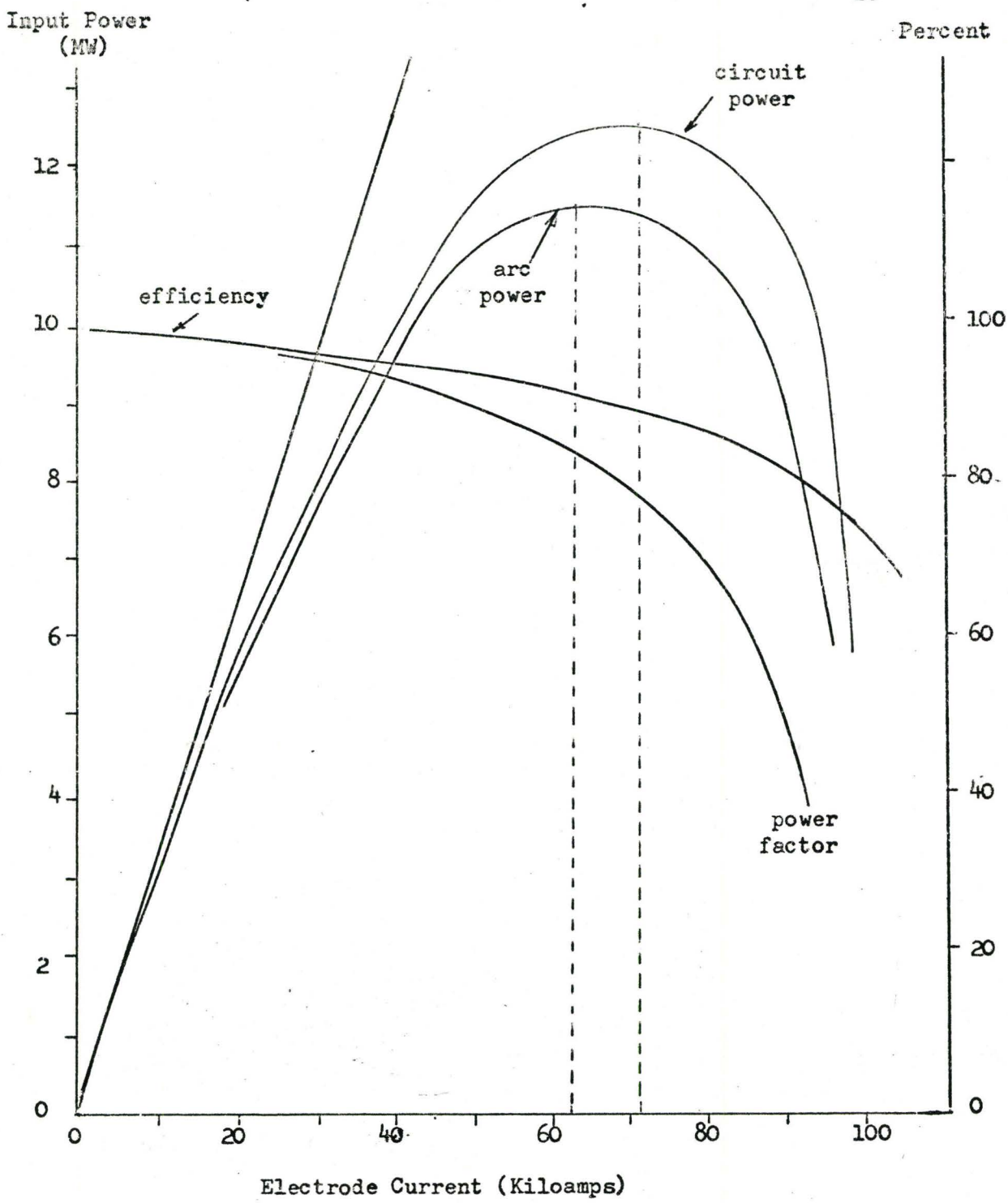

Fig. 1.3: Power Characteristics of a 150-Ton Electric Arc Furnace

During this period it is very beneficial to the quality of the finished product if stirring or agitation of the bath occurs, as in addition to producing homogenization, it promotes the necessary chemical reactions (5). The chemistry of the final product is determined through slag control. The thermal energy input control is via the arc itself.

An understanding of the electrical operation of the furnace demands a knowledge of the properties of the arc and its associated circuitry. Fig. 1.2 shows a diagram of the entire electrical circuit of an arc furnace. Though the arc itself is purely resistive, its characteristic is negative, i.e. increasing the current lowers the voltage across it. To operate stably, the circuit containing the arc should have sufficient reactance to make the volt-amperes characteristic of the total circuit a rising characteristic. In large furnaces, the inherent reactance of the transformers etc, is sufficient, but in smaller versions, additional reactance must be added. Fig. 1.3 shows the power characteristics of an electric arc furnace.

Up to the secondary output terminals of the furnace transformer, the circuit is symmetrical. If the arc power were obtained from this point, the distribution over the three phases would be balanced. However, the power is distributed via the secondary furnace circuit.

There are two basic secondary designs to be considered. These are the coplanar or side by side arrangement of conductors (furnace pre-1970) and the equilateral triangulation of conductors (the modern arc furnace concept). Triangulation of electrode arms and also of the flexible water-cooled cables connecting the electrode arms to the furnace transformer minimises, though not completely eliminates unbalances in the secondary circuit. The electrodes also enter the furnace triangulated, such that the imaginary lines joining their centres form the sides of an equilateral triangle.

Automatic electrode positioning mechanisms serve to raise and lower electrode columns independently, so as to maintain an arc at the power level selected, and to raise the electrodes to clear the top of the shell for charging. Modern furnaces are of the roof charged variety and may be charged twice or thrice to acheive full capacity. The furnace roof is raised and swung aside for this phase.

Almost without exception, the design of every proposed new electric arc furnace installation includes consideration of an acceptable fume control system. The roof of the arc furnace usually contains a fume exhaust aperture connected to an appropriate exhaust system. Since air pollution codes vary regionally, the extent of fume collection and disposal is dependent on the location of the furnace and prevailing codes. Fig. 1.4 illustrates the construction of a modern Héroult electric arc furnace.

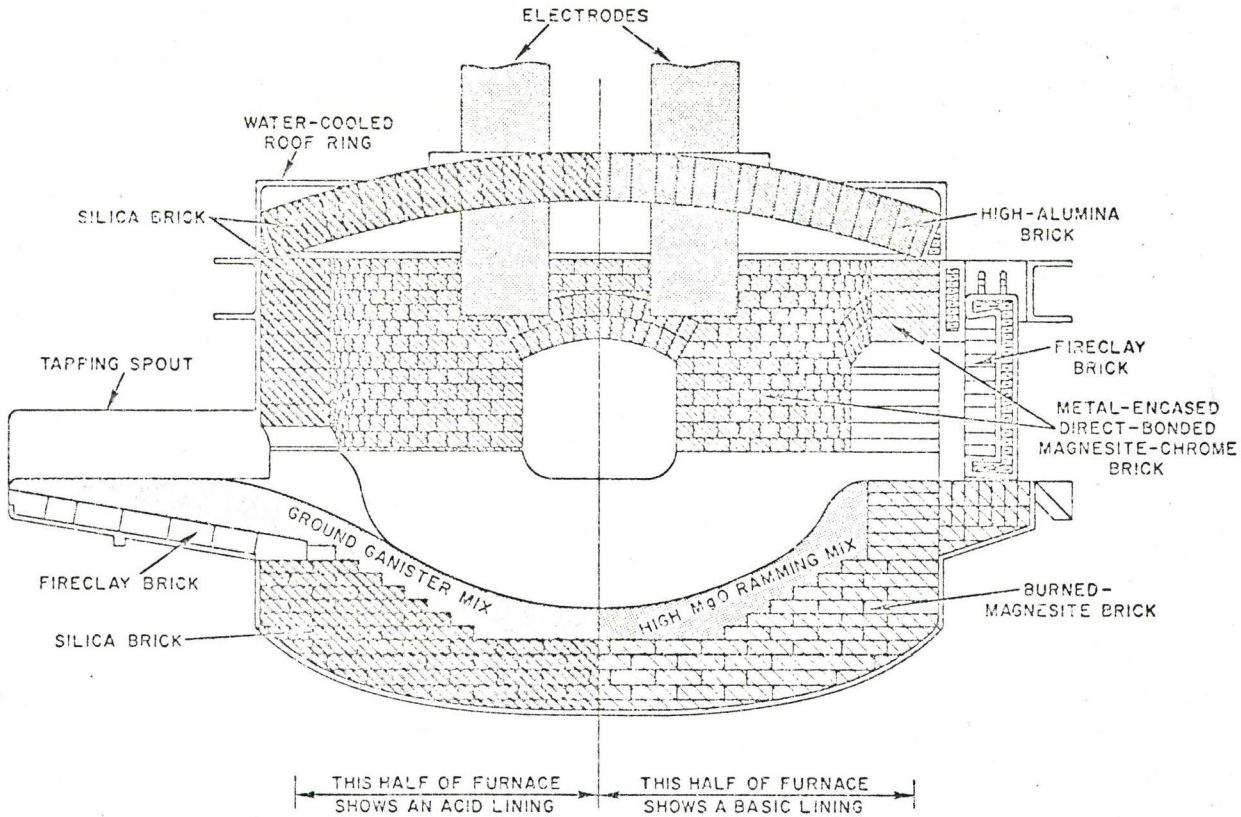

Fig. 1.4: Construction of the Three-Phase Héroult Electric Arc Furnace

1.4 AIM AND SCOPE OF THESIS

The electric arc furnace utilises the heat radiated from the arcs to melt the charge in the furnace. The arc, being a stream of hot ionised gases, or a plasma, is also a good conductor of electricity, allowing currents to flow from the electrodes through the charge. These currents in the molten charge produce electric and magnetic fields, which give heating (J^2/σ) and stirring ($J \times B$) effects.

This additional heating effect is well known in arc furnace technology, but its value or relative value is unknown. At present it is estimated to be small in terms of the heat input of the arc.

The natural stirring that occurs in the crucible is also well known, and sometimes exploited. High current operation of the arc furnace has been termed the poor man's induction stirrer. The magnitude and direction of these stirring forces are again a matter of speculation.

Stirring produced by any means in the electric arc furnace is metallurgically beneficial to the final product, as it produces homogeniety and promotes the chemical reactions important and necessary to the refining processes.

At the present time, if stirring is desired, a two phase induction stirrer is available. This costly device is mounted at the bottom of the furnace, which means that the bottom of the furnace shell must be made of non-magnetic steel. The induction stirrer works on the principle of the linear induction motor, and for adequate penetration of the field into the furnace, requires a special power supply of 0.7 - 1.0 hz.

The problem of current distribution and metal movement has been examined in detail by Alden (7, 8) for the channel-type induction furnace.

Russian literature (9, 10) indicated that similar study has been undertaken for the submerged arc furnace, though the treatment appears to be far less rigorous. The coreless induction furnace has also received full treatment in this regard by Lavers (11).

The present investigation involves a similar study of the electric arc furnace. Since no simple analytical solution at present is available for the geometry of the electric arc furnace, the method chosen was analogue. The author however, estimates that use of tri-polar cyclindrical co-ordinate system could yield good results. A computer program presently in development based on the tri-polar system has predicted the basic current distribution

pattern. Further results of this effort would be reported at some future date.

The aim of the thesis is to measure the current distribution in a suitably chosen model of the electric arc furnace, and to observe the intensity and extent of fluid movement for different electrode configurations, with a view to exploiting the inherent stirring effects.

Any other effects, except those directly influenced by or related to the current distribution and metal movement are beyond the scope of this thesis.

CHAPTER 2

DEVELOPMENT OF MODEL

2.1 CHOICE OF MODEL

No known mathematical model exists at the present time for the electric arc furnace. An analytic or numerical solution was therefore not yet applicable. The method decided on was a straightforward analogue one.

The analogue model presented many alternatives. One was the use of conducting paper to model the furnace in two dimensions. Another was the use of an R-C network with sufficient elements to suitably approximate the continuum. This model could then be completely simulated on a digital computer. These alternatives however suffered from the disadvantage that digitising or reducing to two dimensions introduced errors.

The best model was considered a three-dimensional one, using a conducting liquid to simulate the molten metal. Because of the high temperature ($\geq 2000\ ^{\circ}C$) of the electric arc, an actual small scale, working model of the furnace was considered unsuitable.

In the model finally chosen for laboratory use, mercury modelled the liquid steel, and all measurements were conveniently taken at room temperature. The electrodes were modelled by copper rods which were bright chrome plated to prevent contamination of the mercury. This was considered an important step, since it was unknown to what extent dissolved metallic impurities could change the electrical conductivity of the mercury, a parameter on which subsequent scaling in the model depended. The slag cover on the molten steel was simulated by a layer of dilute (5 percent) nitric acid on the surface of the mercury. The crucible was modelled by a circular dish whose inner contour was a section of a sphere. This was made from a single slab of plexiglass machined out to given specifications, especially for this investigation.

2.2 SCALING

2.2.1 DIMENSION SCALING IN MODEL

Previous work (7, 8, 12) has shown that one important parameter in scaling is the skin or penetration depth which is the depth below the surface of a good conductor, in which electromagnetic fields established at the surface, decay to 1/e of the surface value.

The solutions to both the current distributions in infinitely long cylindrical conductors, and infinitely large

rectangular plates have been shown to be dependent on the ratio x/δ (12). Here x is a linear dimension, and δ is the skin depth defined by

$$\delta = (\pi f \sigma \mu)^{-1/2} \qquad \ldots\ldots\ldots 2.1$$

where f is the frequency of operation and σ and μ, the electrical conductivity and permeability respectively of the medium.

If the model is to exhibit an identical current and flux distribution to the actual furnace, then, in addition to possessing geometrical similarity, it must possess the same x/δ ratio. This gives rise to an electromagnetic scaling criterion

$$(x^2 f \sigma \mu)_M = (x^2 f \sigma \mu)_P \qquad \ldots\ldots\ldots 2.2$$

(where M and P represent model and prototype respectively), defining the parameter constraints for similar current distribution in a device and its electromagnetic model (8).

2.2.2 FLOW SCALING

In the discipline of Fluid Mechanics it has been shown (13) that two flows are similar if geometrical similarity is maintained and certain dimensionless parameters and variables are the same, regardless of the size of the flow pattern. These parameters are

the Reynolds Number, N_R, and the Froude Number, N_F. The Reynolds Number is a measure of the ratio of the inertia to the viscous force and is defined as

$$N_R = (\rho x V/\nu) \qquad \ldots\ldots\ldots 2.3$$

where ρ is the mass density, x the linear dimension, V the velocity and ν the dynamic viscosity of the fluid.

The Froude Number is a measure of the ratio of inertia to the gravity force and is defined by

$$N_F = (V^2/gx) \qquad \ldots\ldots\ldots 2.4$$

where V is fluid velocity, g is the acceleration due to gravity, and x the linear dimension.

It has been further shown (13) that only certain of these dimensionless parameters are important for a given flow, and the fact that all the parameters cannot be made the same does not matter. In this type of flow, gravity is unimportant (13) and the model flow becomes a function of the Reynolds Number only.

Hence, in modelling the flow, we can set

$$(N_R)_M = (\rho x V/\nu)_M = (\rho x V/\nu)_P = (N_R)_P \qquad \ldots\ldots 2.5$$

i.e. the model (M) and the actual furnace (P) should have the same Reynolds Number. The modelling, strictly speaking, may not always be exact, because of the inherent limitations in scaling a situation that depends on several physical quantities. These physical quantities (electrical conductivity, viscosity, density, etc.) cannot be selected independently for a given liquid, and compromises have to be made. For example, mercury chosen here for suitability with regards to electromagnetic scaling, does not possess a sufficiently high mass density to viscosity ratio to simultaneously model the motion of liquid steel. However, the results obtained on the model should still lead to a better understanding of flow in an electric arc furnace.

2.2.3 THERMAL SCALING

The source of heating in the furnace is the electric arc. Since an arc has been dispensed with in the model, no thermal effects are taken into account, except those caused by the passage of the electric current through the metal (J^2/σ effect). It is here assumed that the current distribution (and also the flow) is temperature independent, and the heating and metal flow by current in the model is correspondingly reproduced in the furnace.

The basis of justification of the above assumption regarding current distribution lies in Maxwell's equations, which are

$$\nabla \times E = \frac{\partial B}{\partial t} \qquad \ldots\ldots \quad 2.6$$

$$\nabla \times H = J + \frac{\partial D}{\partial t} \qquad \ldots\ldots \quad 2.7$$

$$\nabla \cdot J = \frac{-\partial q}{\partial t} \qquad \ldots\ldots \quad 2.8$$

$$\nabla \cdot B = 0 \qquad \ldots\ldots \quad 2.9$$

Here, J may further be expressed as

$$J = \sigma(E + V \times B) \qquad \ldots\ldots \quad 2.10$$

These equations describe the electromagnetic field, and are temperature dependent only to the extent to which the relevant physical properties are temperature dependent. The only strong function of temperature here is the electrical conductivity σ, whose temperature variation may be expressed as

$$\sigma_1 = \sigma_2(1 - \alpha_2(T_1 - T_2)) \qquad \ldots\ldots \quad 2.11$$

where σ_1 is conductivity at temperature T_1 degrees centigrade, σ_2 is electrical conductivity at temperature T_2 degrees centigrade and α_2 is the temperature coefficient of conductivity at temperature T_2 degrees centigrade.

It should be noted however, that σ_M is known for the model at its temperature of operation, and σ_P for the prototype, also at its temperature of operation, hence any scaling of current distribution which includes this parameter should present no difficulties.

Preservation of similarity of flow depends on the Reynolds Number, N_R. Here, as above, the variable parameters density (ρ) and viscosity (ν) are known in both cases, at the particular operating temperatures. Relation of flow in the model to that in the furnace is thus possible.

2.3 DESIGN CONSTRUCTION AND OPERATION OF MODEL

2.3.1 DESIGN

Having decided on a small scale model of the furnace, there still remained an important choice to make - that of size and shape. Literature requested from manufacturers of electric arc furnaces, yielded some idea of furnace diameter in relation to capacity, though this varied somewhat with the manufacturer. Observation of this variation has led to the development of a systematic method of the optimal design of electric arc furnace shells, which take into consideration the density of the scrap charged and the number of charges to the furnace. Application of the Calculus of Variations to the present geometry of the electric arc furnace indicated that the hearth should be a section of a sphere, and

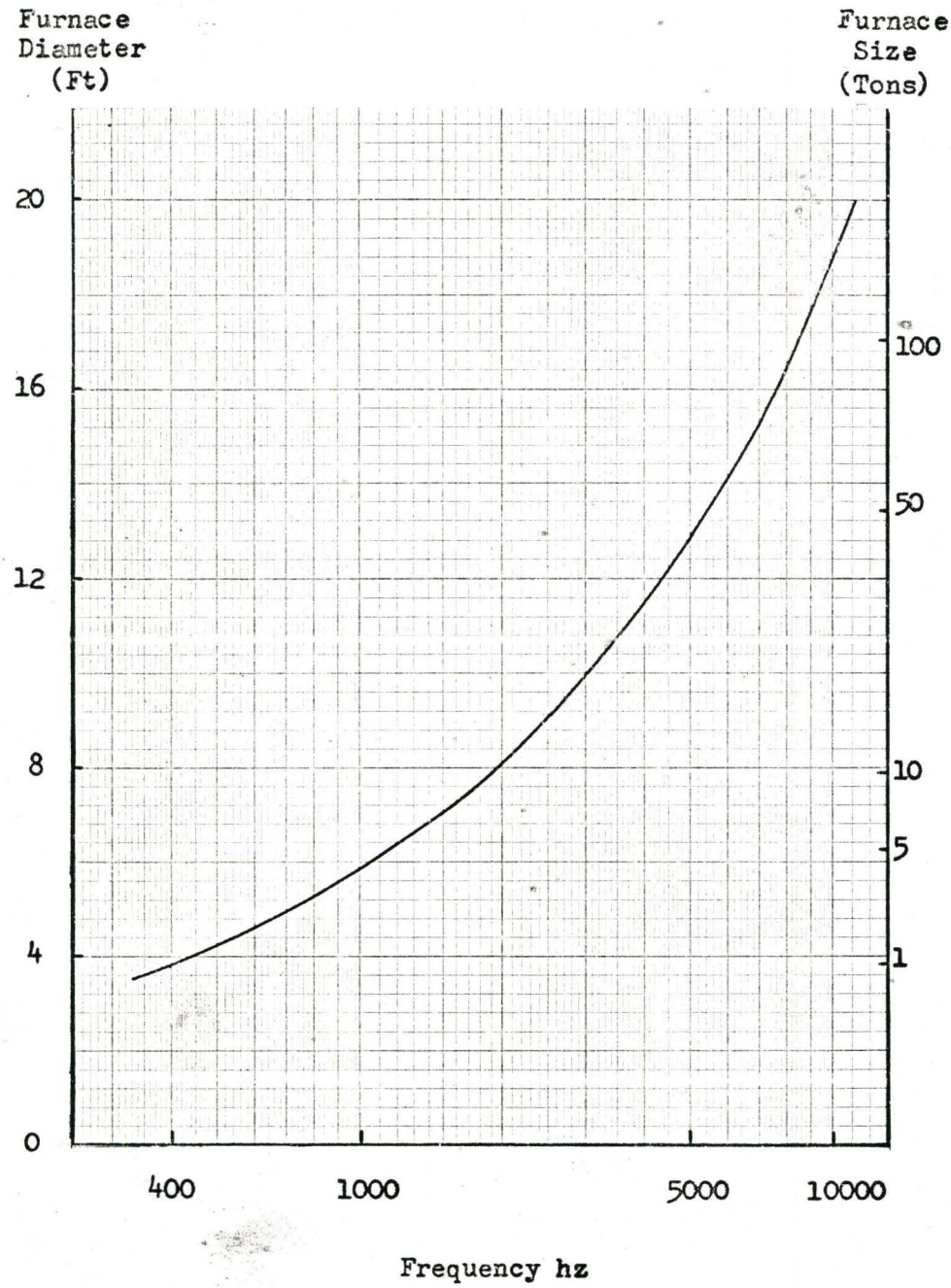

Fig. 2.1: Diameter of Furnace Modelled in Relation to Frequency

established its centre and radius of curvature, depth and diameter for a given metal capacity and scrap charge density.

With the shape decided on, the next question to be answered was what size the model should be. Using the electromagnetic scaling criterion expressed in equation 2.2, and taking into consideration the total volume and weight of mercury required, it was decided to use a model of diameter 1 ft (0.304 m). This represented a 1-ton furnace at 400 hz and a 100-ton furnace at 8.5 khz. The hearth depth was 2.7 in (0.0687 m), and had a capacity of 2.65 litres, (which for mercury weighed 80 lb (36.2 kg)). Fig. 2.1 shows the variation of the diameter of the furnace modelled with frequency. Table 2.1 lists the physical properties of mercury and liquid steel relevant to the design. For current density measurements a filament-type current density probe devised by Alden and Burke was chosen. Details of probes used are given in Table 2.2.

2.3.2 CONSTRUCTION

Hearth: The hearth was constructed from three inch (0.0763 m) thick plexiglass. A slab of the material about fourteen inches square (0.356 m square) was first machined out into a short, right circular cylinder, then the spherical dish representing the hearth machined out to design specifications. Since a cylindrical system of measurements seemed appropriate, the side of the hearth was graduated in degrees in

TABLE 2.1

PHYSICAL PROPERTIES OF MERCURY AND LIQUID STEEL (8)

PROPERTY	MERCURY	LIQUID STEEL
Melting Point $^{\circ}C$	$-38^{\circ}C$	$1535^{\circ}C$
Mass Density ρ kg/m^3	13.5 (at $20^{\circ}C$)	7.84 (at $1535^{\circ}C$)
Electrical Conductivity σ mhos/m	1.01×10^6 (at $50^{\circ}C$)	0.49×10^6 (at $1535^{\circ}C$)
Viscosity η sec^2/m	1.55×10^{-3} (at $20^{\circ}C$)	4.0×10^{-3} (at $1535^{\circ}C$)

TABLE 2.2

FILAMENT-TYPE CURRENT DENSITY PROBES

PROBE NUMBER	MATERIAL	FILAMENT LENGTH (cm)	FILAMENT DIAMETER (cm)	INSULATION	USE
№ 1	Stainless Steel	0.354	0.0356	'Eccospray' Ph-5	Measurement of surface current density in three-electrode model
№ 2	Copper	0.520	0.0457 (№ 26) A.W.G.	Enamel	Measurement of surface current density in four-electrode model
№ 3	Copper	0.497	0.0457 (№ 26) A.W.G.	Enamel	Measurement of variation of current density with depth in both models

Frequency (hz) 60, 400, 1000

Skin Depth (cm) 6.5, 2.5, 1.6

the interval 0 - 90 degrees. A fibre ring fashioned to revolve smoothly about the top of the hearth, was marked into four quadrants, and equipped with a probe arm of variable radius (the arm being graduated in terms of distance from the centre of the hearth rather than the edge). Fig. 2.2 shows the construction of the hearth and the calibrated ring.

Current Density Probe: For current density measurements, a filament-type probe was used. This enabled the current density in the model to be measured in magnitude and phase on an oscilloscope.

In construction, the probe consisted of two insulated lengths of wire tightly twisted together, except in the last inch or two at both ends. One end was electrically connected to the input terminals of the oscilloscope. At the other end, the individual wires were bent at right angles to the twisted pair to form a T. The length of the filament is the distance measured across the top of the T.

To measure current density, the filament is placed in the desired region of the liquid and rotated to give maximum signal on the oscilloscope. In this condition, it is aligned with the current, and the relationship between the probe voltage V and the current density J is given by the expression

$$V = \ell J/\sigma \qquad \ldots\ldots\ldots 2.12$$

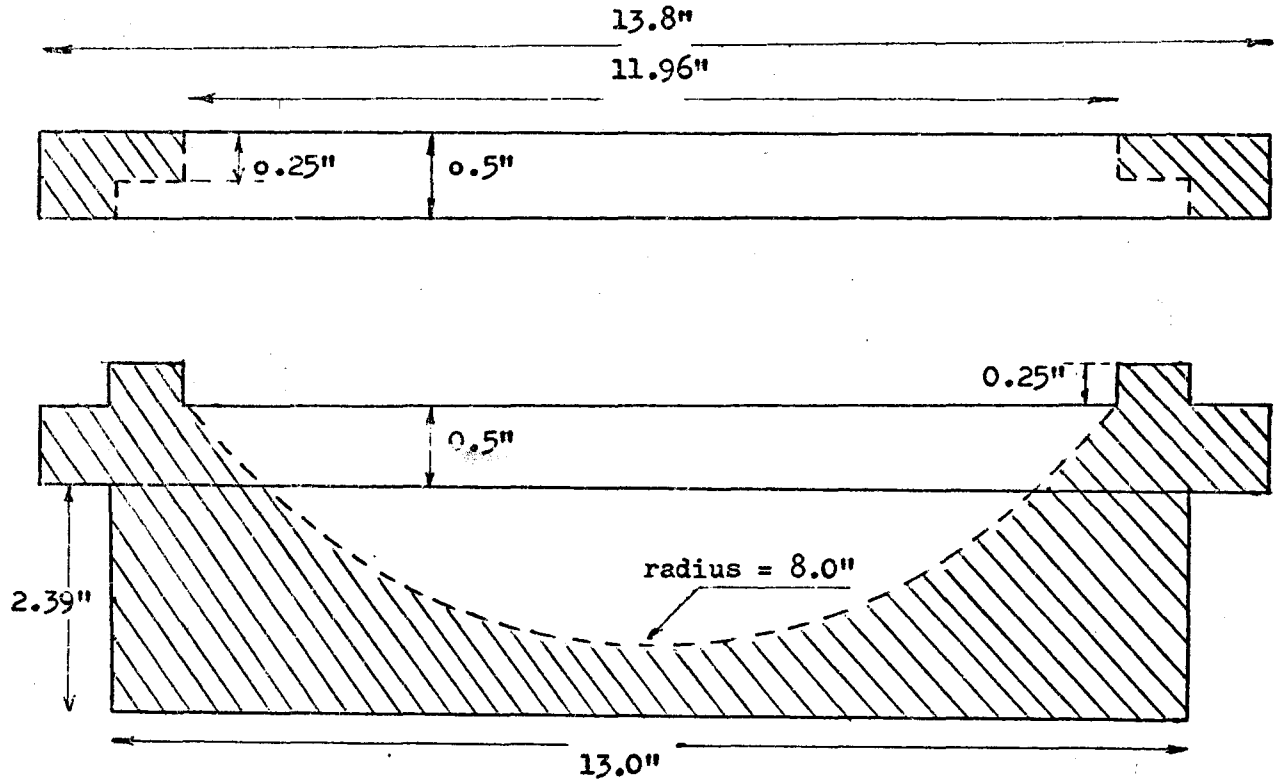

Fig. 2.2: Dimensions of Model and Ring

where σ is the conductivity of the liquid. For the probe to be accurate, the filament should be sufficiently short that current density can be considered constant along its length. As a compromise, filaments were cut so as to be as short as possible, yet sufficiently long (about 0.5 cm) to give adequate output signal. For good resolution, filament insulation should be thin, and diameter small in comparison to skin depth. The details of probes used are given in Table 2.2.

Initially, a stainless steel probe (№ 1 in Table 2.2) was used in the current density measurements, since stainless steel is not corroded by the nitric acid modelling the slag or the mercury modelling the molten metal. Momentary loss of contact between this probe and mercury, as sometimes occurred during adjustments, made cleaning of the probe necessary. This was accomplished by brushing the probe tips with fine emery paper, immersing in a dilute solution of phosphoric acid and quickly returning it to the mercury. This problem was found to be due to inherent contact resistance that exists between mercury and stainless steel, and stainless steel wire was replaced by copper. The copper probes seldom required cleaning, but required washing after use to prevent corrosion by the acid.

For rigidity and ease in handling, a 5 cm length of the twisted leads near the filament was mounted inside a 1/4 inch

(0.00635 m), drilled rod. Fig. 2.3 illustrates the construction of the current density probe.

Probe Arm and Holder: The probe arm was made of stainless steel rod, 1/4 in (0.00635 m) in diameter and 12 in (0.305 m) long, and was graduated in 1/4 in (0.00635 m) steps. It was designed to slide smoothly, without play, through a hole drilled in a one inch (2.54 cm) thick plexiglass block, and could be secured in any position with a screw having a knurled head. As explained above, the entire probe arm was attached to and rotated with a circular graduated fibre ring free to rotate smoothly about the top of the hearth. One end of the probe arm was threaded into what may be termed the probe holder. This consisted of a teflon cylinder exactly 3 cm (0.03 m) in circumference, about 1 cm (0.01 m) high, and with a hole 5/16 in (0.0079 m) in diameter centred on the vertical axis. The probe was free to rotate about a vertical axis in the 5/16 in (0.0079 m) hole and was fitted with a pointer. Centimetre graph paper attached to the 6 cm circumference teflon cylinder, conveniently divided up the cylinder into degrees and enables the measurement of the angle of rotation of probe to within 6 degrees of arc.

Electrodes: In the model, chrome-plated copper rods model the electrodes. These were 3/8 in (0.00942 m) in diameter and one was fitted on each of three, chrome-plated copper electrode arms displaced 120 degrees in a horizontal plane. The entire assembly

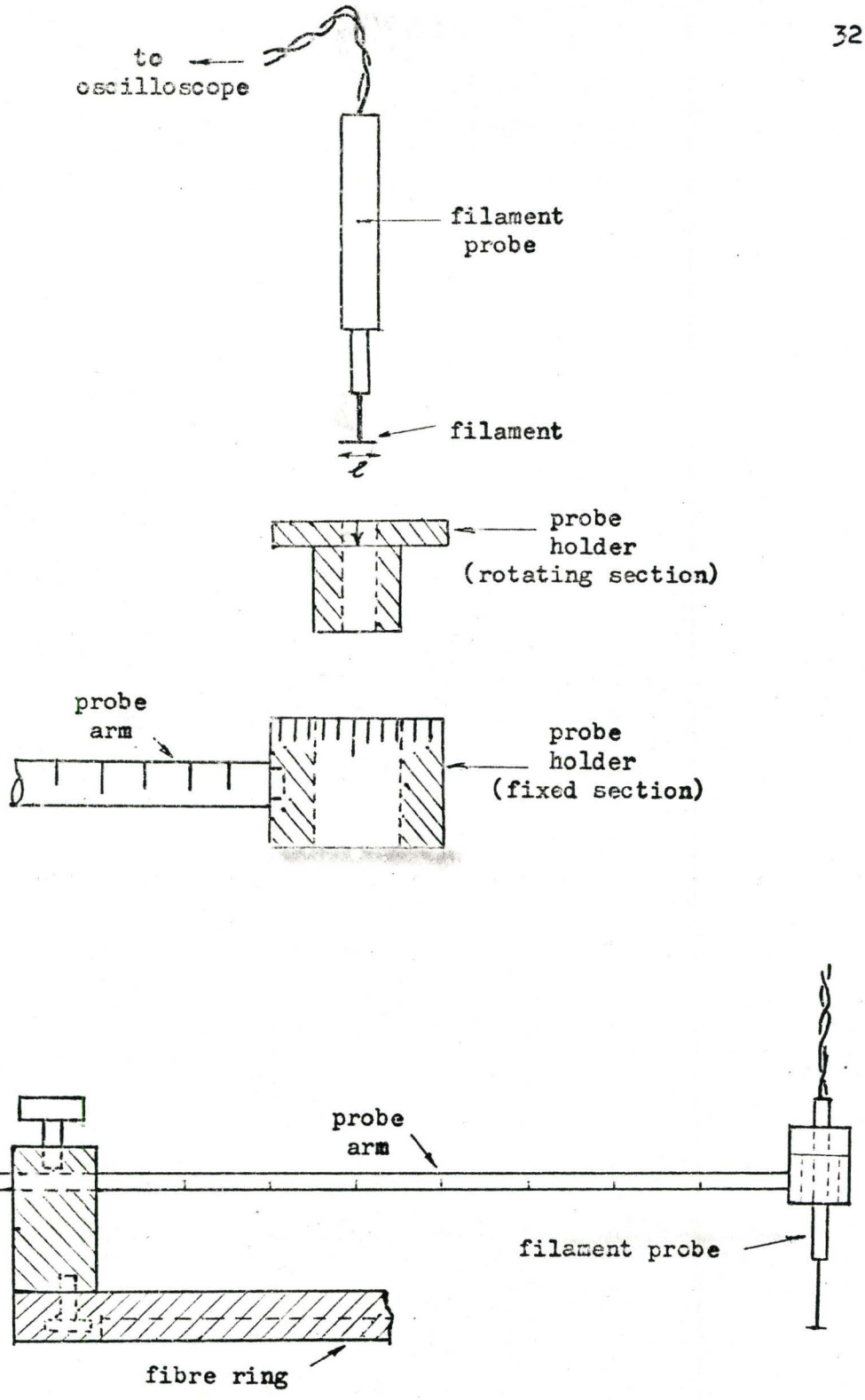

Fig. 2.3: Probe Arm, with Holder and Probe

could be moved in a vertical plane to simulate the lowering and raising of the electrodes in the actual furnace. While the actual furnace current enters the liquid metal via the electric arc, in the model, the electrodes are in constant electrical contact with the mercury to prevent an arc. In a real furnace of 1 ton (1016 kg) capacity, the electrodes are about 3 - 4 in (0.0762 - 0.1016 m) in diameter. In the model, the electrode size to scale would be about 1 in (0.0254 m). The diameter of the arc where it strikes the melt is unknown. Research in this area (15) show photographically that the diameter of the arc is less than that of the electrode, hence the size chosen was considered a good approximation.

The electrodes were movable along the electrode arms, and were adjusted so that the ratio

$$R_C/R_F = 0.33 \qquad \ldots\ldots\ldots 2.13$$

where R_C is the radius of the electrode circle and R_F the radius of the furnace. Current literature (15, 16) indicates that this is a common ratio.

The electrode arms were connected to the secondary of the furnace transformer by flexible, N^{o} 10 A.W.G., rubber insulated conductors, which were twisted together to minimise pick-up by the probe.

The entire system to this point was enclosed in a fume chamber because of the toxic effects of mercury. The exhaust fan was kept continually in operation to remove mercury vapour present and care was taken to minimize spills. Rubber gloves were worn as often as possible and direct contact between mercury and hands avoided.

Three 3-inch lengths of threaded brass rods, acting as lead-throughs, were passed through holes drilled in one wall of the fume chamber. These connected the flexible conductors attached to the electrode arms inside the chamber to the furnace transformers mounted outside the chamber.

Power Supply: Initially the power source was three-phase, four-wire, 60 hz (laboratory supply) and 400 hz (special generator) at 230 volts line to line. This power system, shown in Fig. 2.4 (a) consisted of

(1) Three single phase variable voltage transformers T_1, T_2, T_3. These served to adjust for equal current in each phase.

(2) One variable voltage, three-phase transformer bank (3-ϕ variac) T_4. This was used to adjust the current level in each phase simultaneously, for convenience. Since T_1-T_3 control the voltage level at which T_4 operate, adjustment could be made for smoother operation. As the furnace transformers were always short circuited, it was difficult to set the current levels to a predetermined point

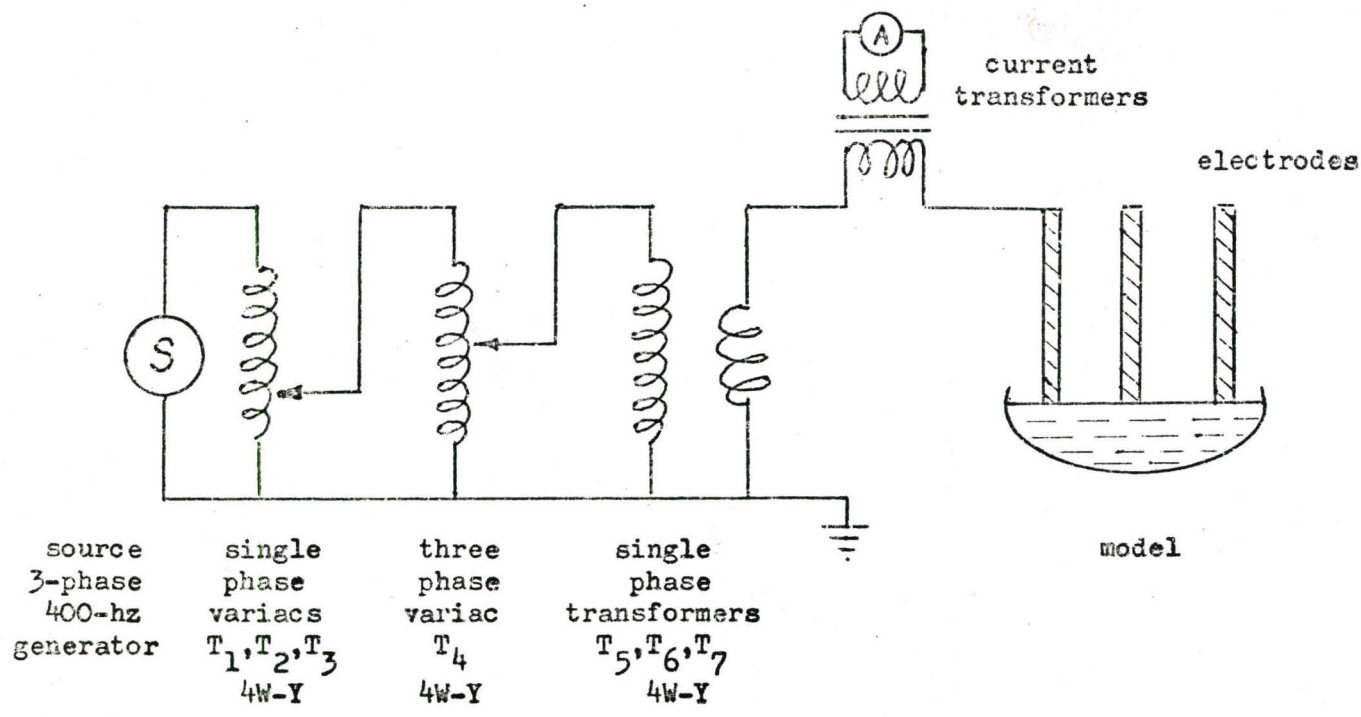

(a) Initial Power Supply for Model

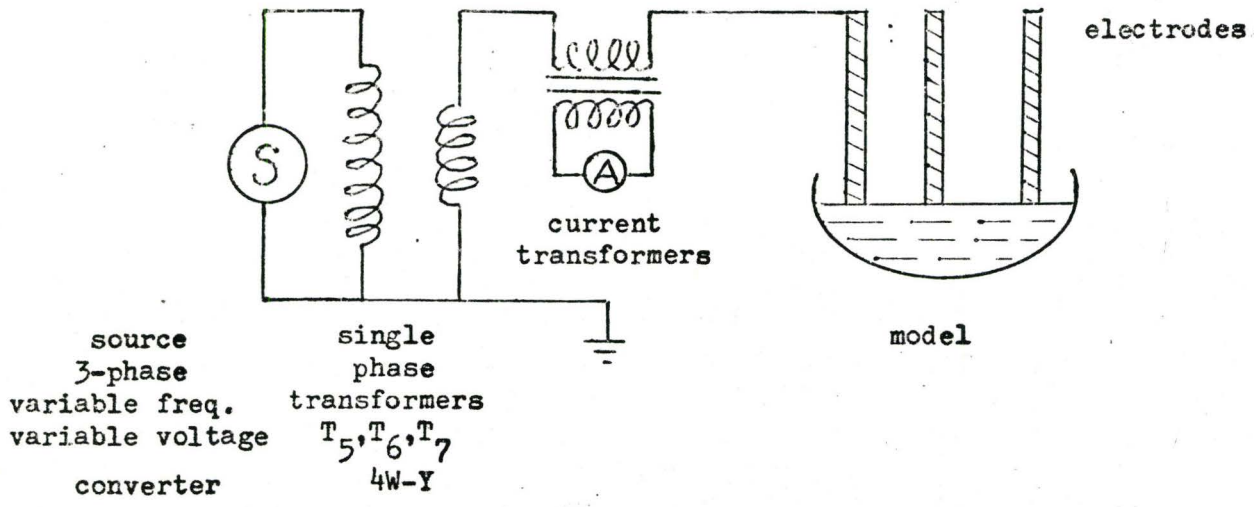

(b) Final Power Supply for Model.

Fig. 2.4: Power Supplies for Model

using T_4 alone.

(3) Furnace transformer T_5, T_6, T_7. These consisted of three single phase transformers with primary in Y and low voltage, high current secondaries also in Y. Each transformer secondary was hand-wound to deliver about 200 amps at around 3 volts.

Current transformers were inserted in each line to monitor the current in each electrode. The entire power supply system was mounted about 3 ft (1 m) vertically above and about 2 ft (0.61 m) away from the model to minimise proximity effects. Later, a three-phase, variable voltage (0 - 230 volts line to line), variable frequency (60 - 10 khz) power supply was available. Since the output voltage in each phase was adjustable, only the furnace transformers T_5, T_6 and T_7 were required. The new power supply is shown in Fig. 2.4 (b).

Fig. 2.5 shows the assembled model in the fume chamber.

Auxillary Apparatus: Previous observers of mercury flow in models (8) noted that a clean mercury surface soon became covered with an oxidised skin, even when under a layer of water. Any fluid motion occurring in the mercury took place under this skin, and could only be detected by the slight rippling effect caused. As this was unsatisfactory for velocity measurements, the mercury had to be frequently cleaned. Attempts to clean only the surface did not yield good results, and the entire bulk of the mercury had to be cleaned.

Fig. 2.5: Model Assembled in a Fume Chamber

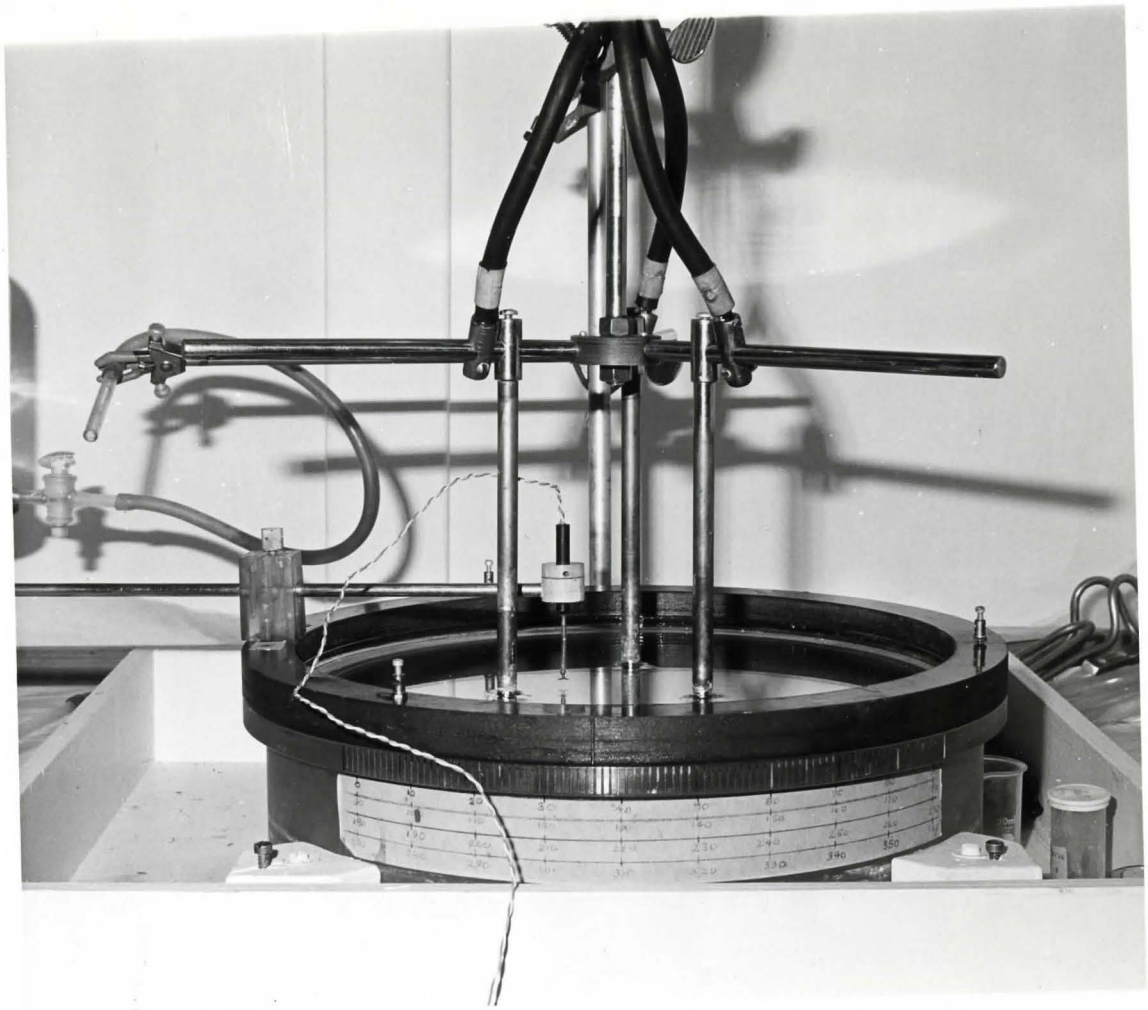

Cleaning consisted of running a thin stream of mercury through a long, vertical column of dilute (20 percent) nitric acid. The acid solution had to be made up using distilled water, as the use of tap water caused the formation of white insoluble chloride of mercury, as much a nuisance on the surface as the skin. As hand pouring through the cleaning was both tedious and hazardous to health apparatus was designed and assembled to perform this. Fig. 2.6 shows the assembled apparatus. A stainless steel, water-powered, aspirator pump was used to lift the mercury about 20 in (0.5 m) high. The mercury was then allowed to fall in a thin stream through the 12 in (0.3 m) long cleaning column. Tap T_1 controls the rate at which mercury is raised to be cleaned. Taps T_3 and T_4 control the rate at which mercury enters the reservoir. With a clamp holding tap T_1 in the desired position, if T_1, T_2 and T_3 are suitably adjusted, then the rate at which the reservoir fills is the same at which mercury enters T_1, and the apparatus does not require constant attention. Tap T_4 is used to add more acid whenever required. Tap T_5, normally closed, may be opened slightly after the mercury stream reaches the column. The bubbles of air that now enter the column from below, thoroughly mix the mercury and acid, thus providing more effective cleaning. All other taps (T_6 - T_8) are closed during this phase. When the aspirator is not on, taps T_5 and T_6 are used to remove mercury and/or acid. Tap T_7 is used to remove mercury and acid from the mercury trap. Tap T_8 is used to return clean mercury to the model.

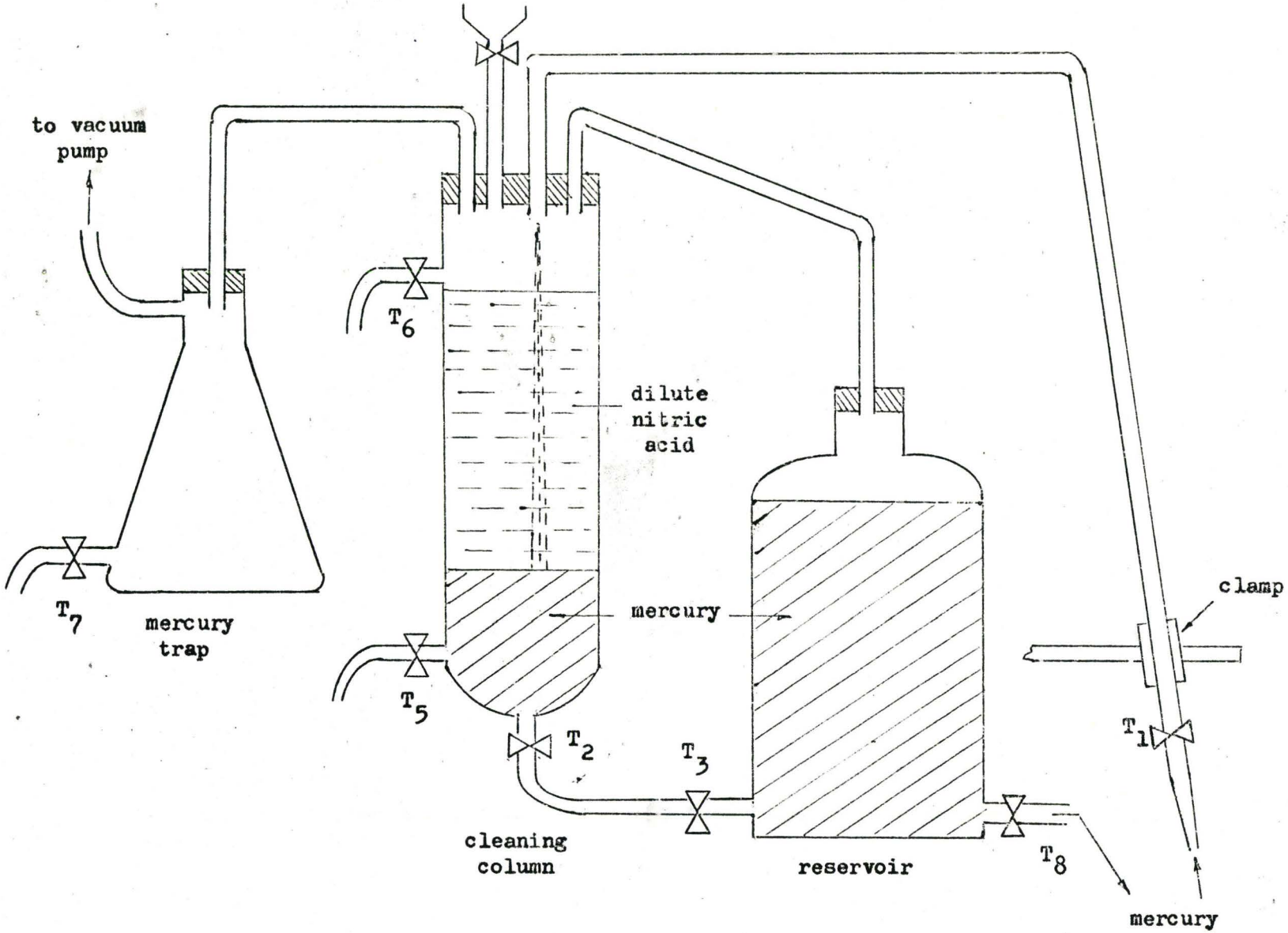

Fig. 2.6: Apparatus for Cleaning and Storage of Mercury

With this apparatus, the total cleaning time for the quantity of mercury used in the project (80 lb), was reduced from upwards of 40 minutes to about 15 minutes.

CHAPTER 3

CURRENT DISTRIBUTION

3.1 MEASUREMENT TECHNIQUES

Measurements of current distribution in the model involved the measurement of three quantities. These were:-

(1) The radius of the probe arm, 'r'. This was adjusted in 1/2 in (0.0127 m) steps from the centre, over the range 0 - 6.0 in (0 - 0.1524 m).

(2) The position of the probe arm, 'θ' measured in degrees with respect to the position of phase B of the electrode system. This was measured over the entire interval 0 - 360 degrees.

(3) The position of the axis of the filament with respect to the axis of the probe arm. This angle, ϕ, was measured in 6.0 degree steps over the range 0 - 360 degrees.

(4) Magnitude of probe voltage, 'v'. This was measured peak-to-peak on a Hewlett-Packard 1200A dual trace oscilloscope on the 0.1 and 0.2 mV/cm scales, using differential input and dc coupling.

(5) Phase of probe voltage, 'β'. This was taken with respect to the voltage waveform in one phase.

Fig. 3.1 shows the physical arrangements for measurement of r, θ and ϕ.

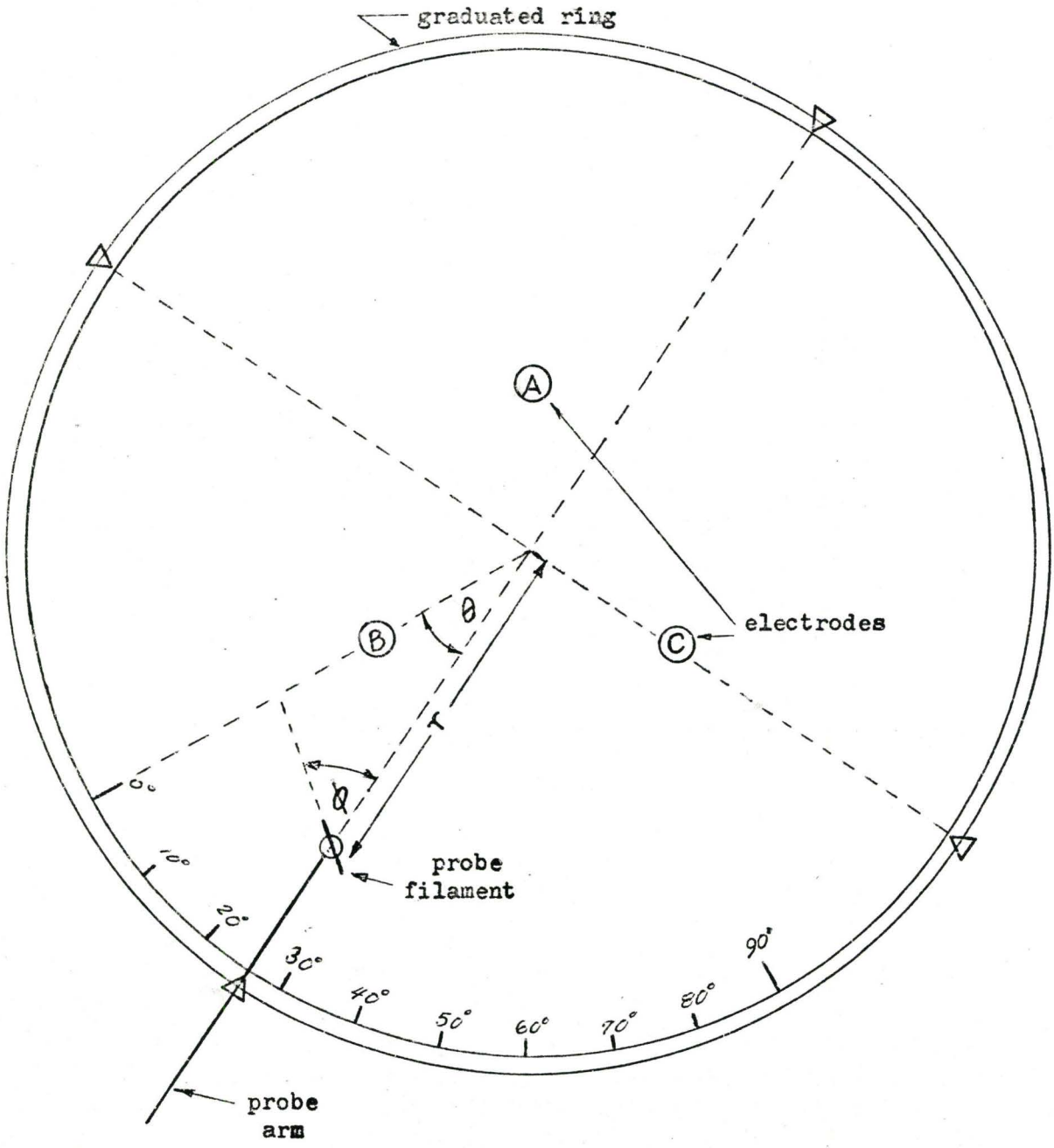

Fig. 3.1: Plan of Model, Showing System of Measurement of r, θ and φ

The probes provided excellent signals which were free of noise or distortion. To measure the surface current densities, the filament was adjusted to be just under the surface of the mercury. The stainless steel probe required frequent cleaning, about every 5 to 15 minutes, because of contact resistance problems. Copper probes seldom required cleaning, but slowly dissolved in the mercury and the acid. Signal repeatability was in general good, within 5 percent, and depended on the depth to which the electrodes were immersed in the mercury. However, near the electrodes, where the rate of change of current density with distance was large, the ability to duplicate previous measurements was dependent also on vertical alignment of the probe axis, its eccentricity and the radius of the probe arm.

The probe output voltage was measured peak-to-peak on an oscilloscope and the values divided by $2\sqrt{2}$ to convert to r.m.s.

3.2 CURRENT DISTRIBUTION IN THE THREE-PHASE MODEL

In the three-phase model, both the angular position θ and the electrical phase angle β were measured with respect to phase 'B' of the electrode system.

Initially, for a chosen value of r, measurements were taken over the entire range of θ, from 0° to 360°. However, it was observed

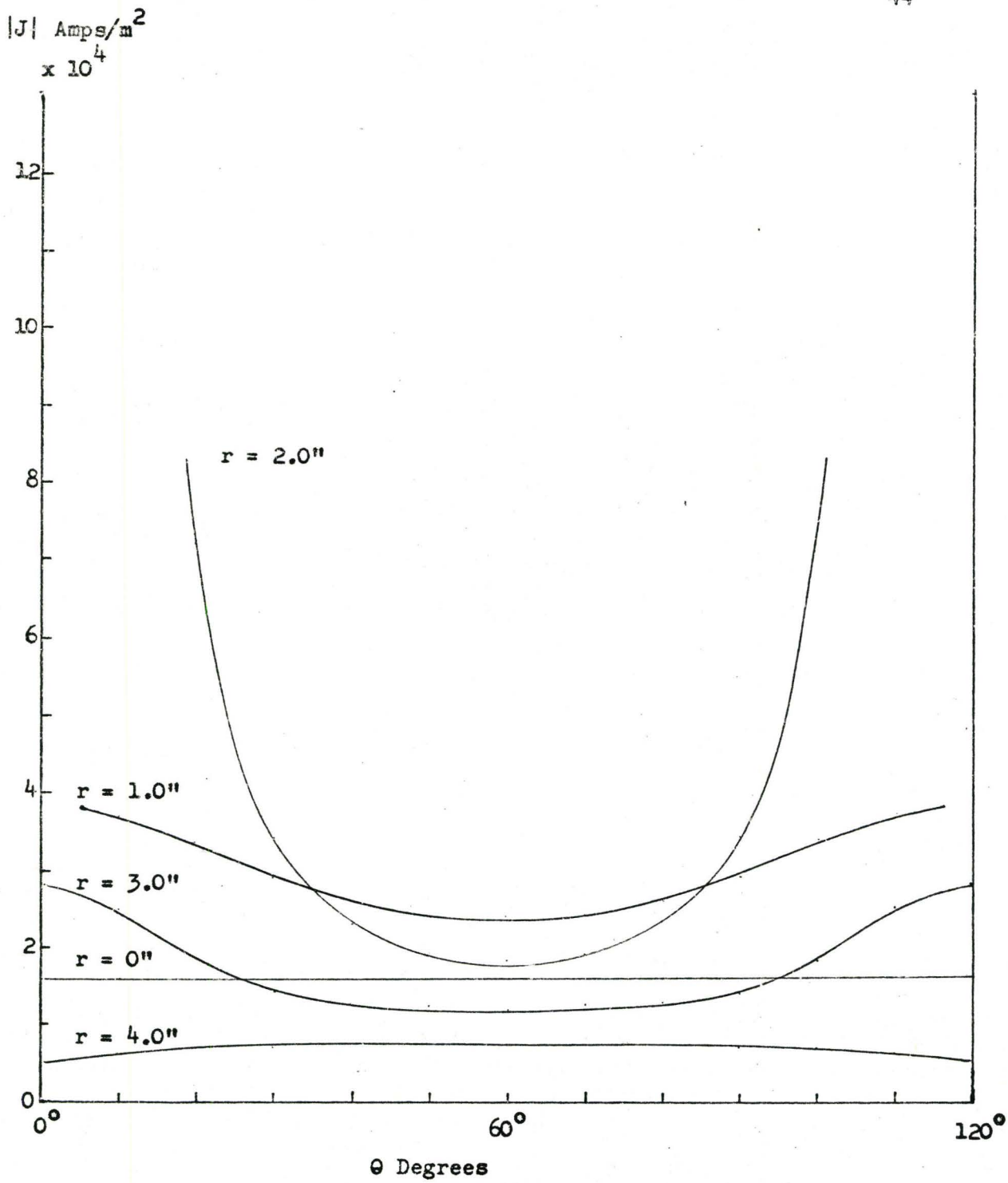

Fig. 3.2: Current Distribution in Three-Phase Model at 60 hz

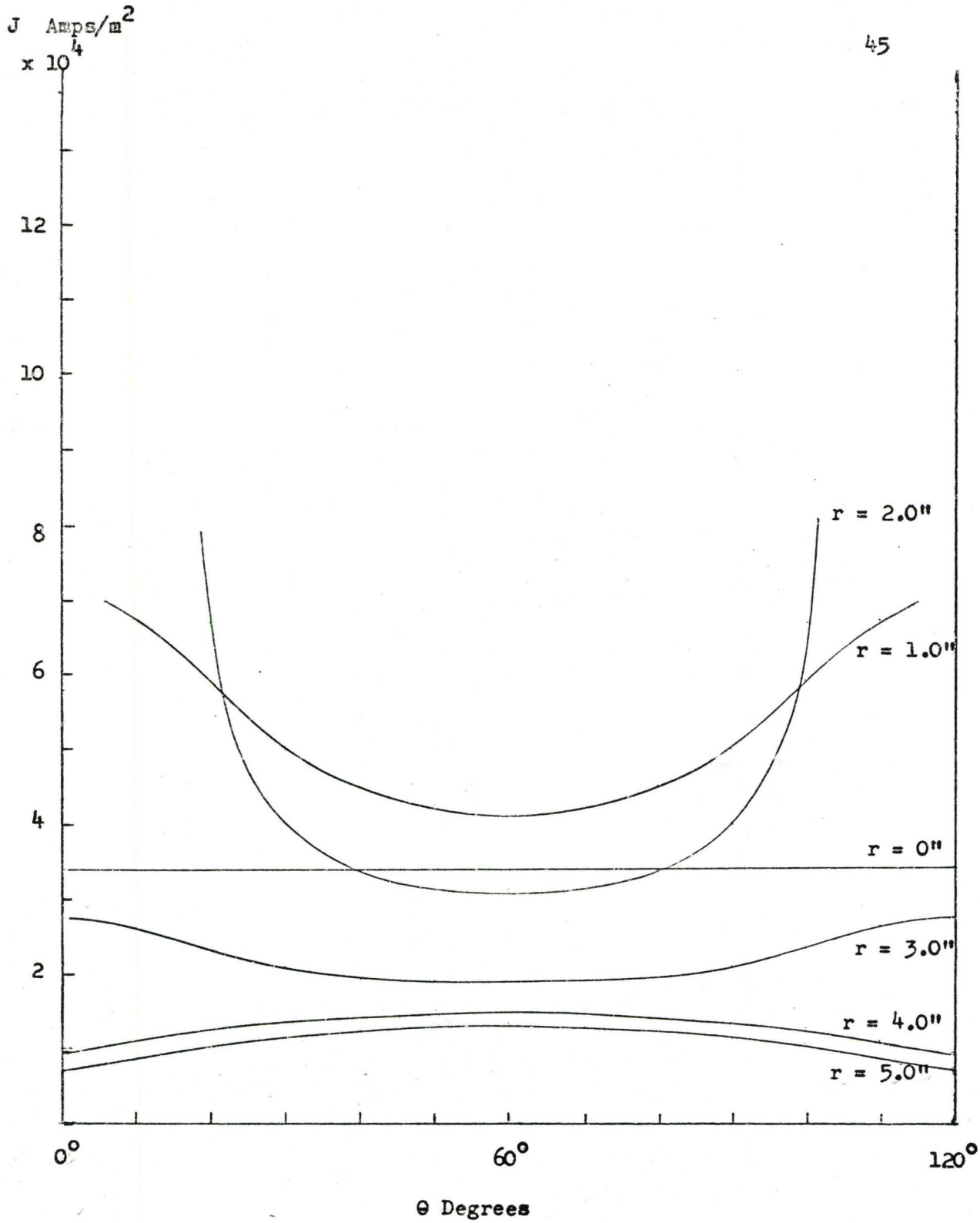

Fig. 3.3: Current Distribution in Three-Phase Model at 400 hz

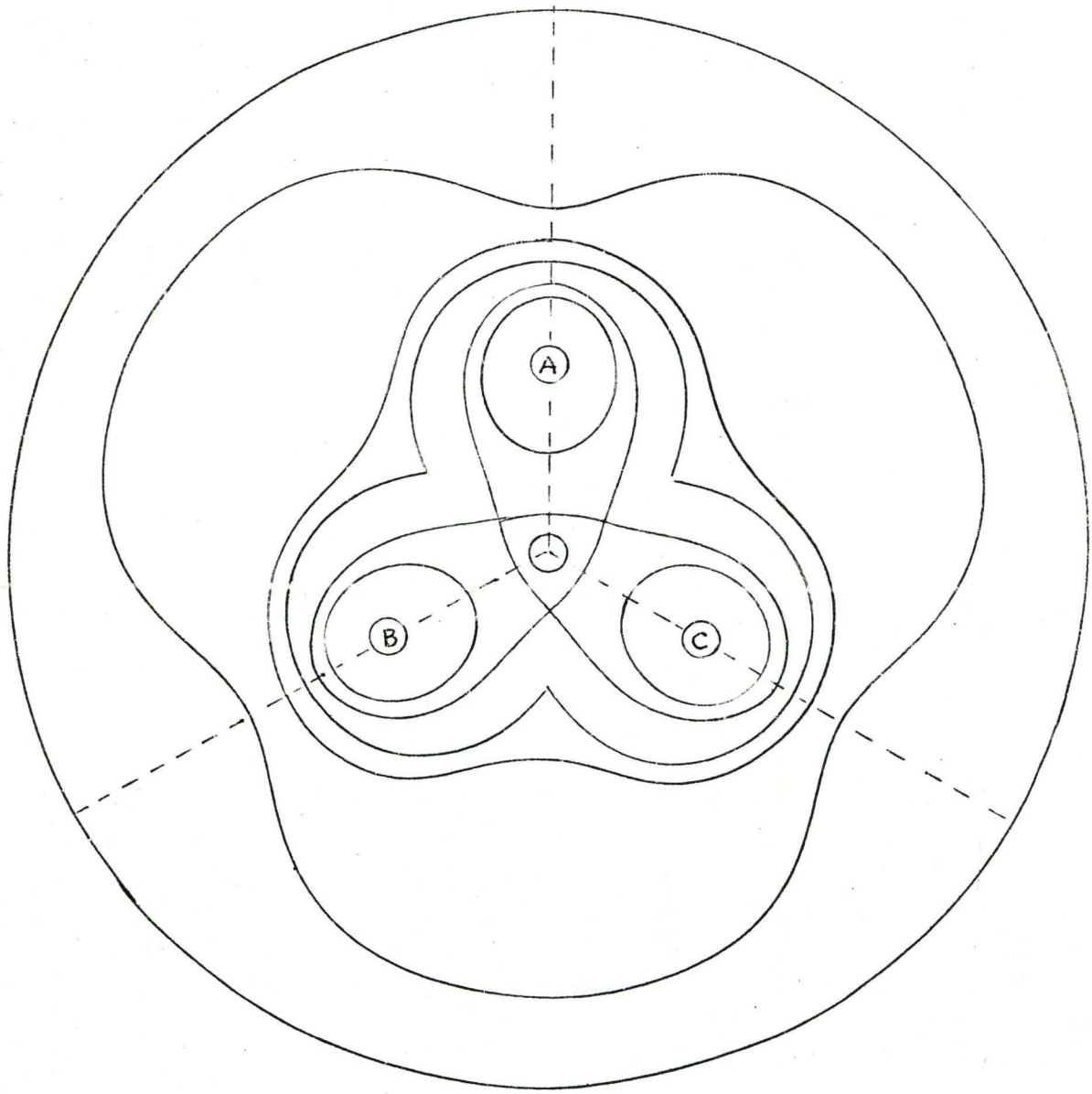

Fig. 3.4: Current Density Profiles in Three-Phase Model at 60 hz

that the values of β and ϕ for a given radius were the same in the areas between electrodes (0° - 120°, 120° - 240°, 240° - 360°) and exhibited symmetry about $\theta = 60^\circ$, 180° and 300°. From then on, to minimise the number of readings taken, values were only measured in the interval $0^\circ \geq \theta \geq 120^\circ$.

Since symmetry was found to exist about the line, $\theta = 60^\circ$, the current density was taken as the average of values equally spaced about this axis. The measured values are given in Appendix C. Fig. 3.2 shows the average current density as a function of r and θ taken at a frequency of 60 hz. Fig. 3.3 shows the same, but at a frequency of 400 hz. These were obtained by first setting the desired value of r and θ, then rotating the probe (varying ϕ) for maximum output on the oscilloscope. Deviation from symmetry is considered to be due to tilt and eccentricity in the vertical axis of the probe, and to the electrodes not being at exactly the $\theta = 0^\circ$, 120°, 240° positions.

Fig. 3.4 and 3.5 show equal current density contours in the model at 60 and 400 hz respectively. These were obtained by drawing horizontal lines in Fig. 3.2 and 3.3 at $J = 5.0 \times 10^4$ A/M^2, 2.0×10^4 A/M^2, 1.25×10^4 A/M^2 etc and plotting r and θ in polar form.

Fig. 3.6 and 3.7 show the approximate current stream lines at 60 hz and 400 hz respectively. This was obtained by plotting ϕ as short directed line segments as a function of r and θ, then connecting up suitable line segments to give the approximate stream lines. The

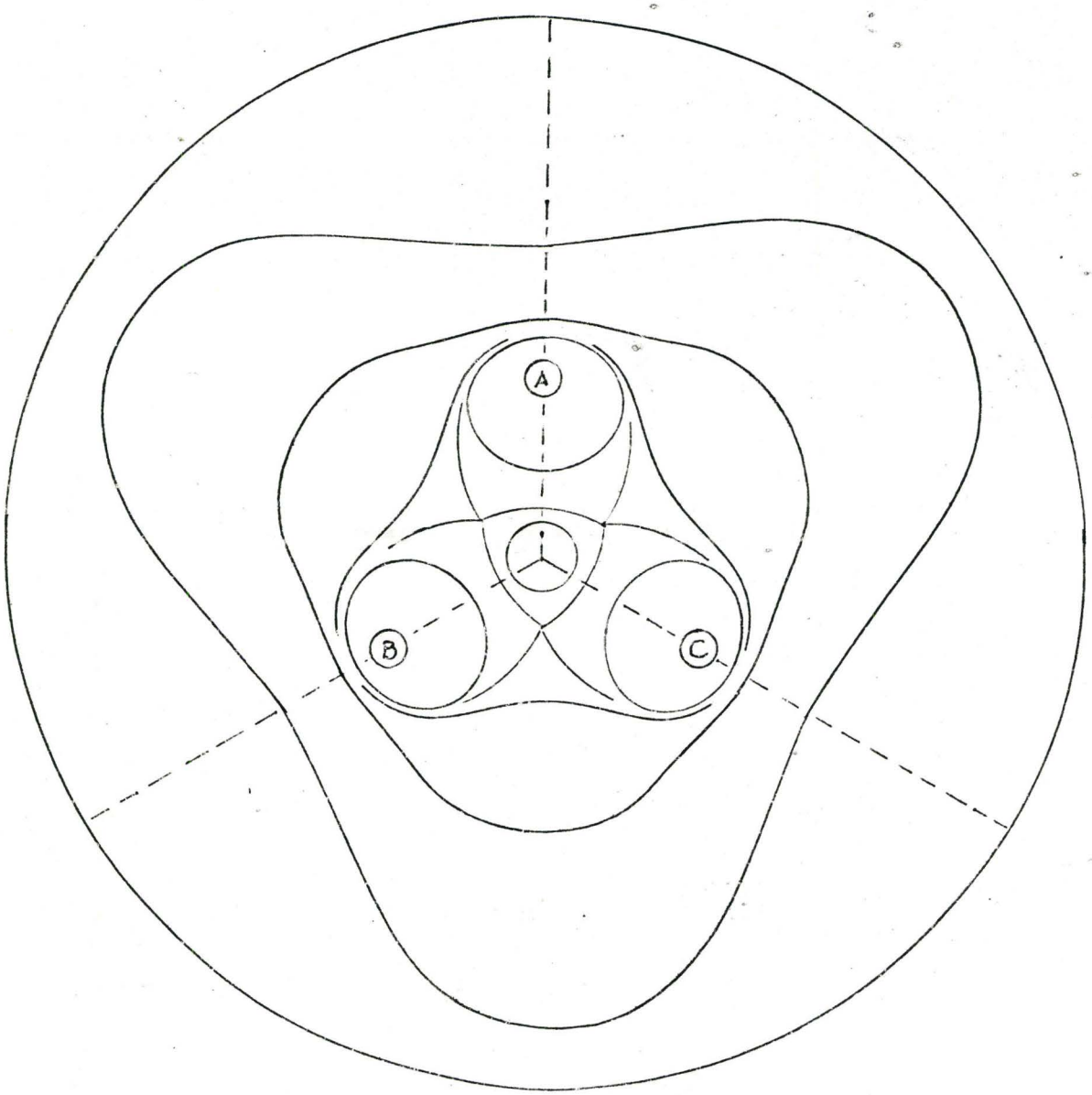

Fig. 3.5: Current Density Profiles in Three-Phase Model at 400 hz

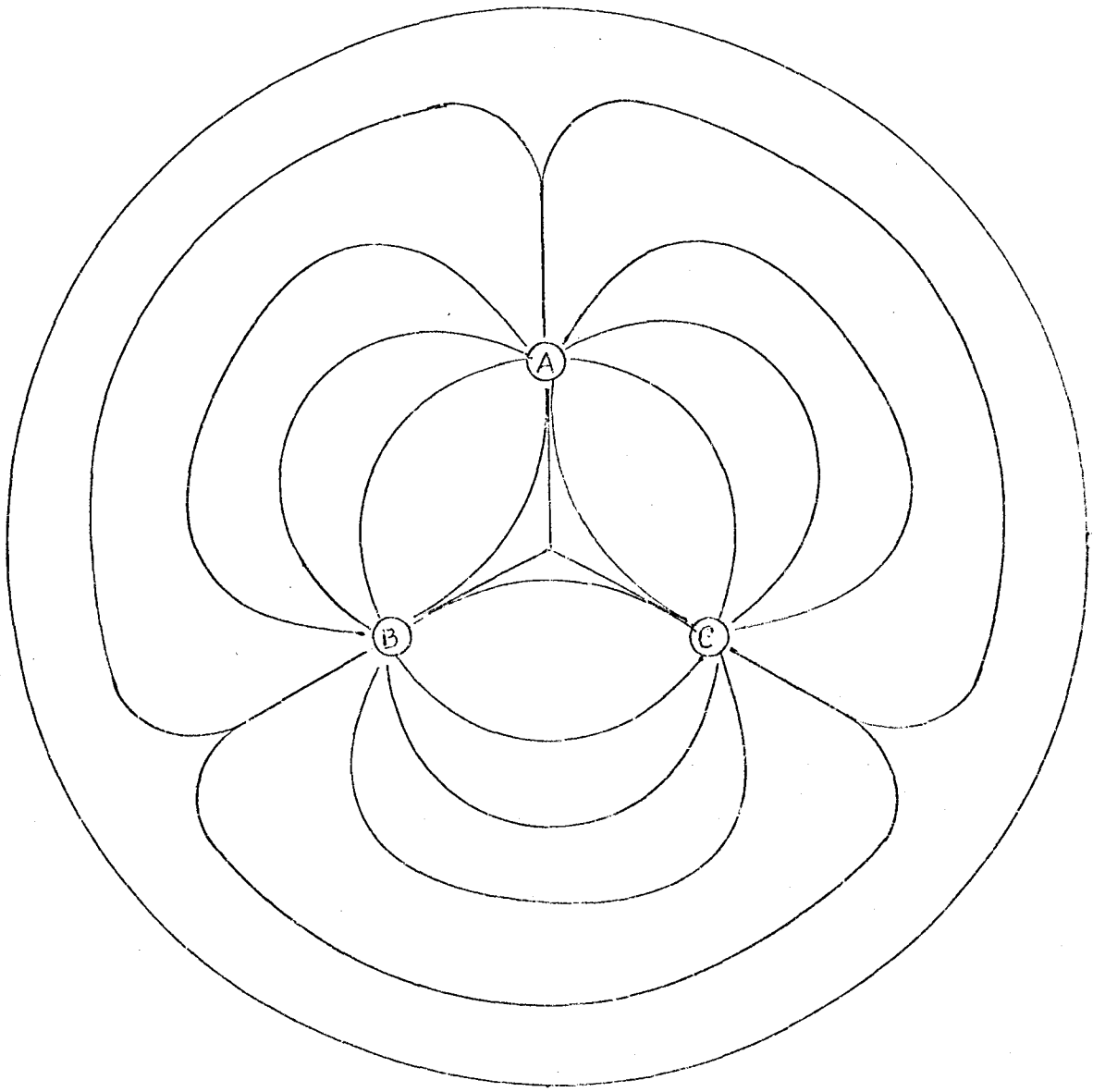

Fig. 3.6: Current Streamlines at 60 hz in Three-Phase Model

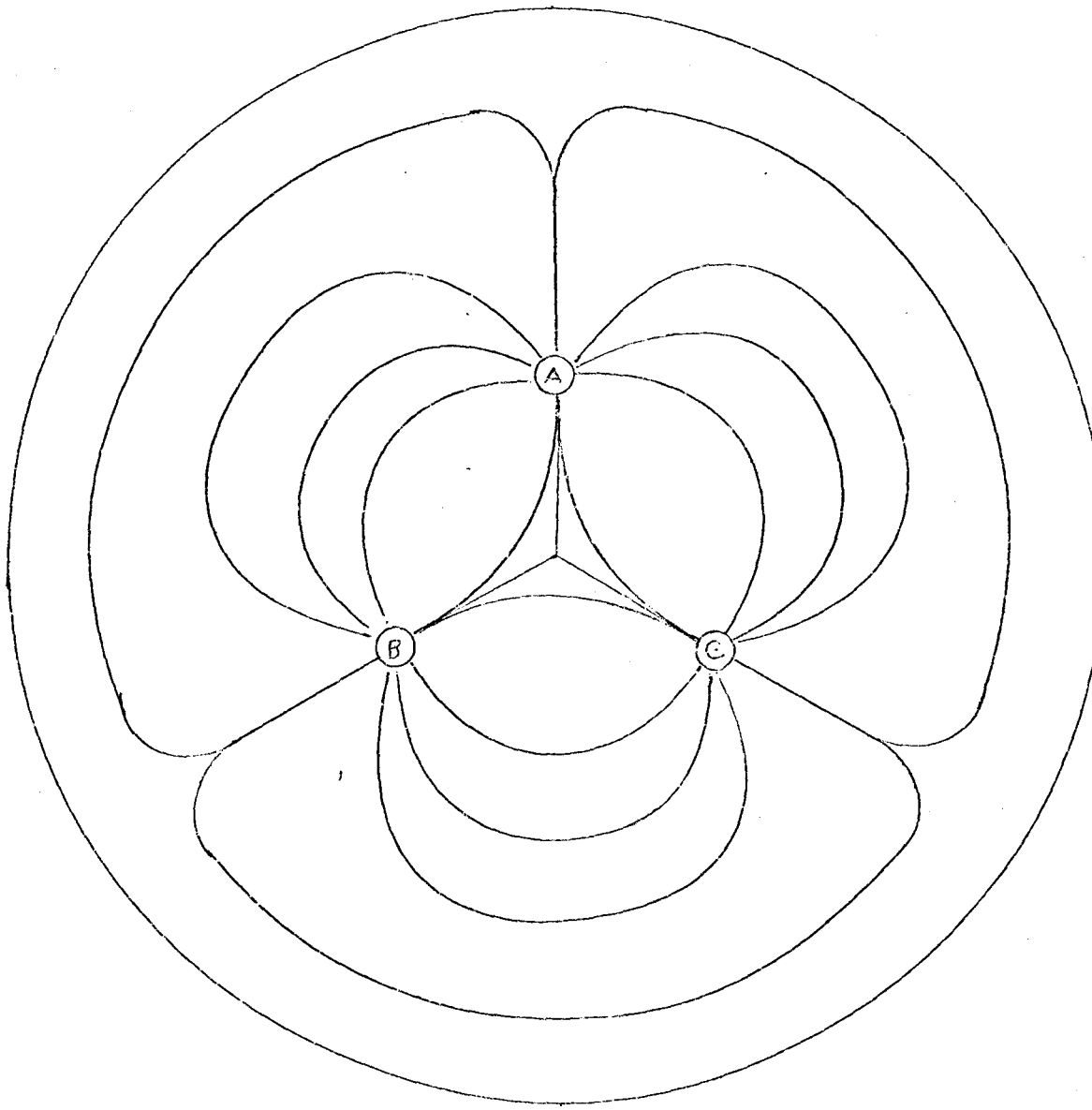

Fig. 3.7: Current Streamlines in Three-Phase Model at 400 hz

method of following the streamlines, as is done in standard field plotting techniques, would be very time consuming in the cylindrical coordinate system, as it would require constant simultaneous adjustment of r, ϕ and θ.

3.3 CURRENT DISTRIBUTION IN THE TWO-PHASE MODEL

At the present time, no two-phase electric arc furnaces are in operation (no mention in current literature). However, it was decided to examine this electrode configuration as a possible alternative to the three-phase system. The reasons surrounding the choice were based on metal movement in the furnace, and will be dealt with fully in that section.

The experimental setup was the same as before, except that the three-electrode mast was replaced by a four-electrode mast. Two single phase transformers, each operating on one phase of a two phase supply, each fed a pair of electrodes.

The three-phase system has only one basic configuration, with two phase sequences - sequence A-B-C or sequence A-C-B, giving a total of two arrangements, one a mirror image of the other.

The two-phase, four-electrode system on the other hand possesses two basic configurations - one with electrodes of the same phase adjacent, and another with these electrodes opposite each other. These configurations and their mirror images give a total of six

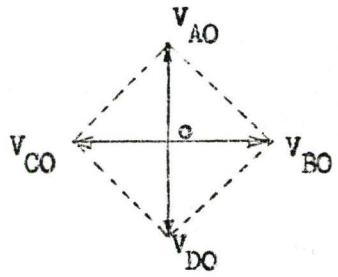

$$V_{BO} = \frac{V}{2}\angle 0^\circ \qquad V_{AC} = \frac{V}{\sqrt{2}}\angle 45^\circ$$

$$V_{AO} = \frac{V}{2}\angle 90^\circ \qquad V_{CD} = \frac{V}{\sqrt{2}}\angle 135^\circ$$

$$V_{CO} = \frac{V}{2}\angle 180^\circ \qquad V_{DB} = \frac{V}{\sqrt{2}}\angle 225^\circ$$

$$V_{DO} = \frac{V}{2}\angle 270^\circ \qquad V_{BA} = \frac{V}{\sqrt{2}}\angle 315^\circ$$

$$V_{AD} = V\angle 90^\circ \qquad V_{BC} = V\angle 0^\circ$$

(a) Voltage Phasor Diagram
V is Furnace Transformer Secondary Voltage ℓ/ℓ

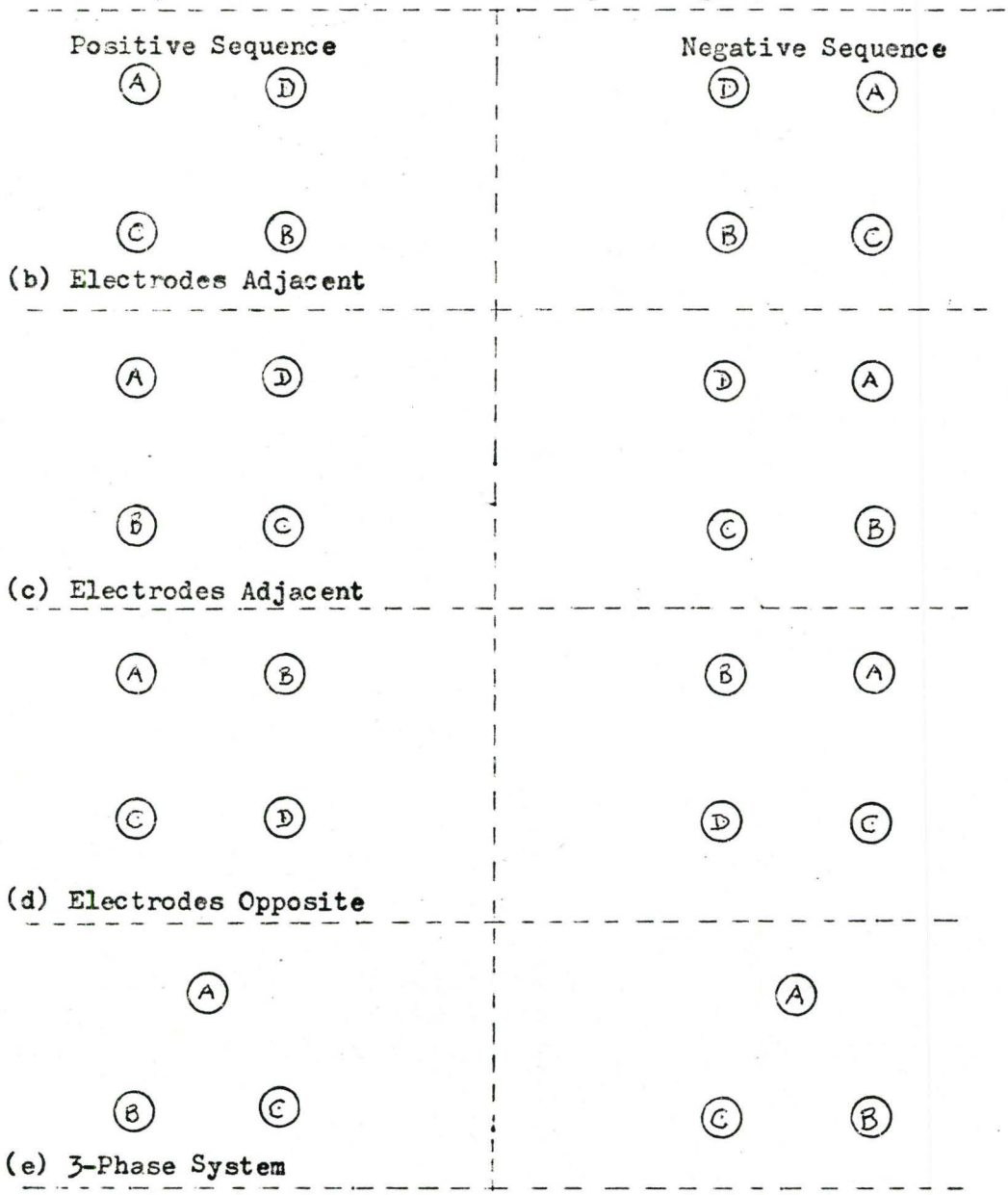

Fig. 3.8: Electrode Configurations in Two-Phase Model

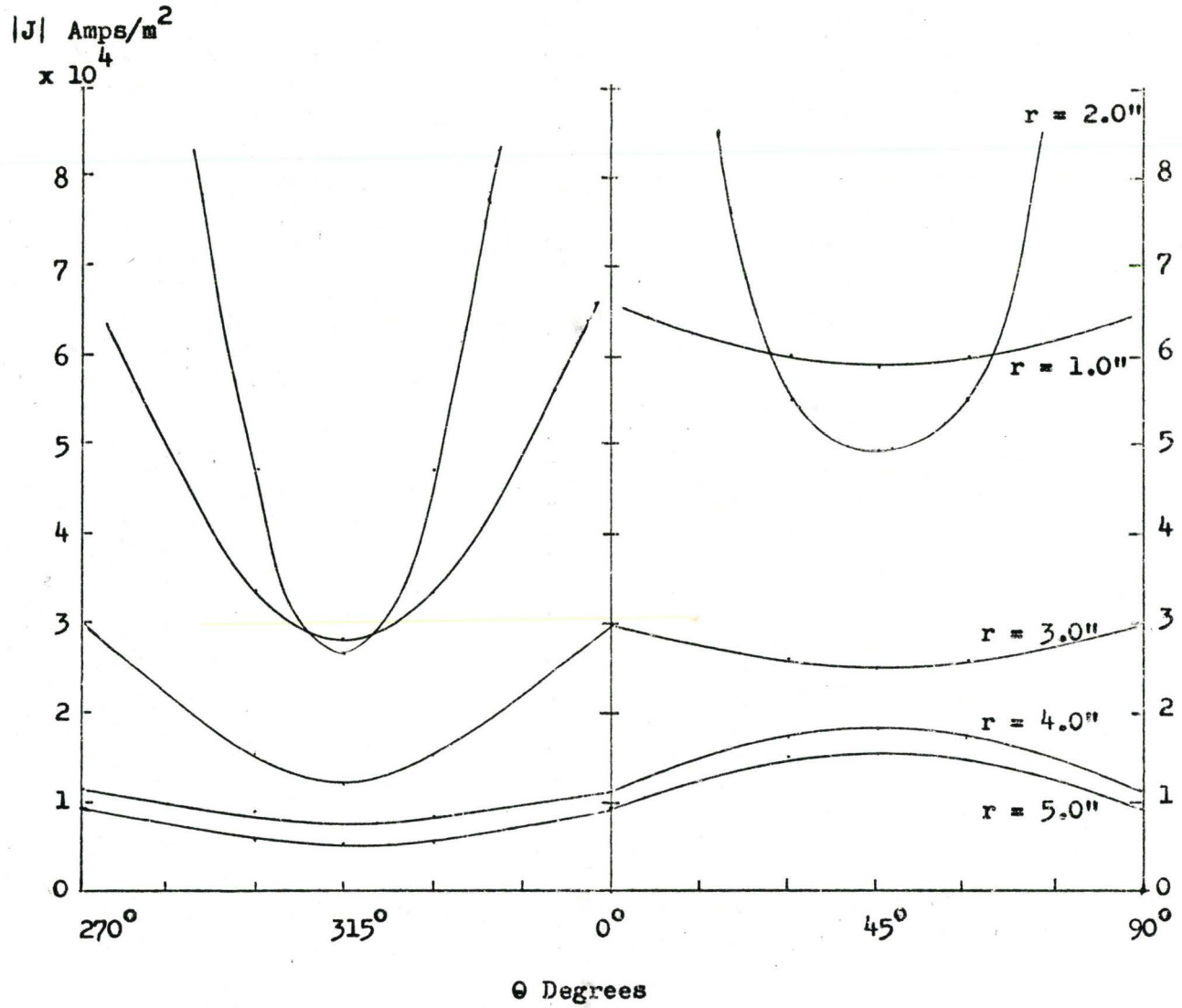

Fig. 3.9: Current Distribution in Two-Phase Model. Electrodes of same Phase Adjacent (400 hz)

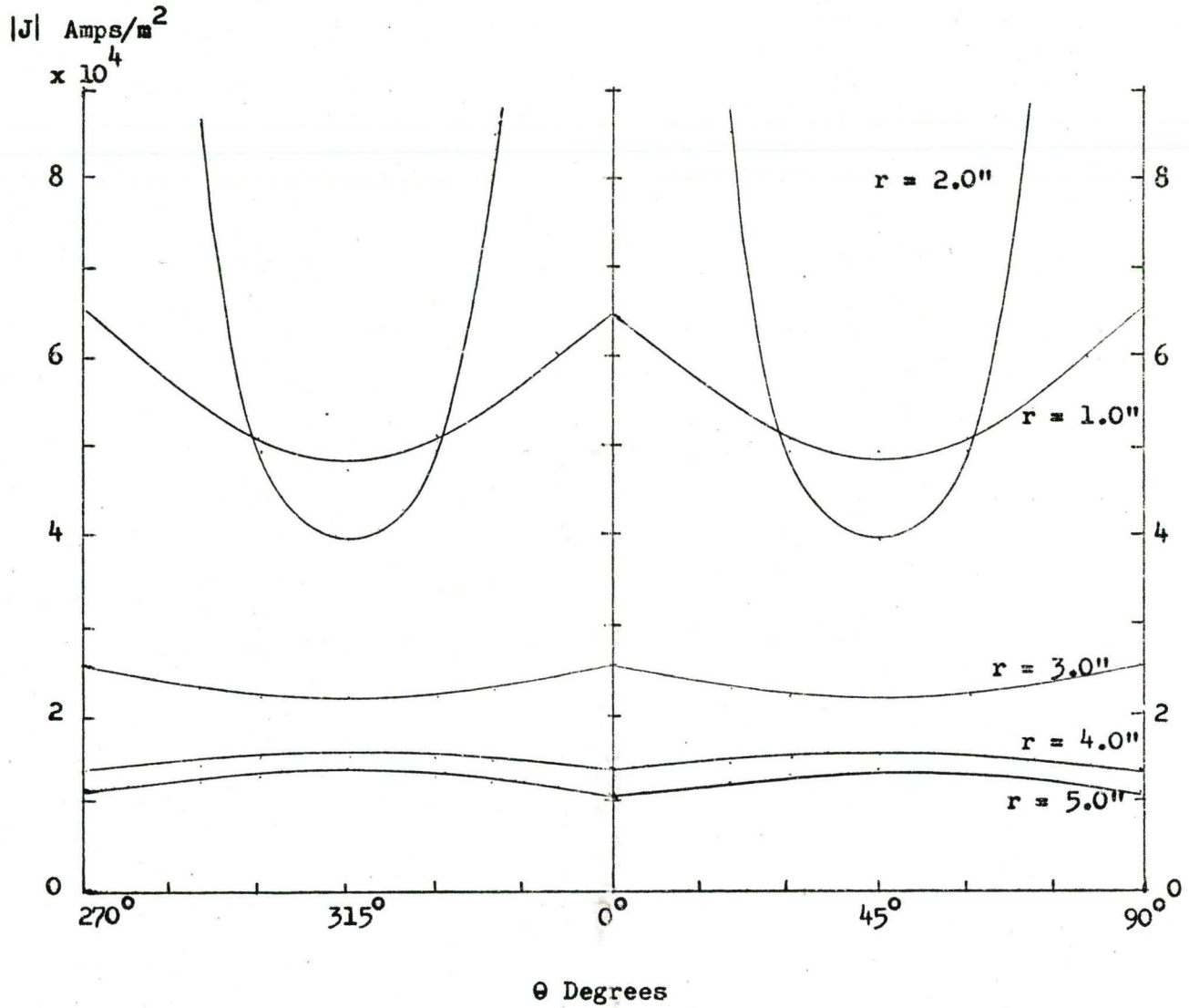

Fig. 3.10: Current Distribution in Two-Phase Model. Electrodes of same Phase Opposite (400 hz)

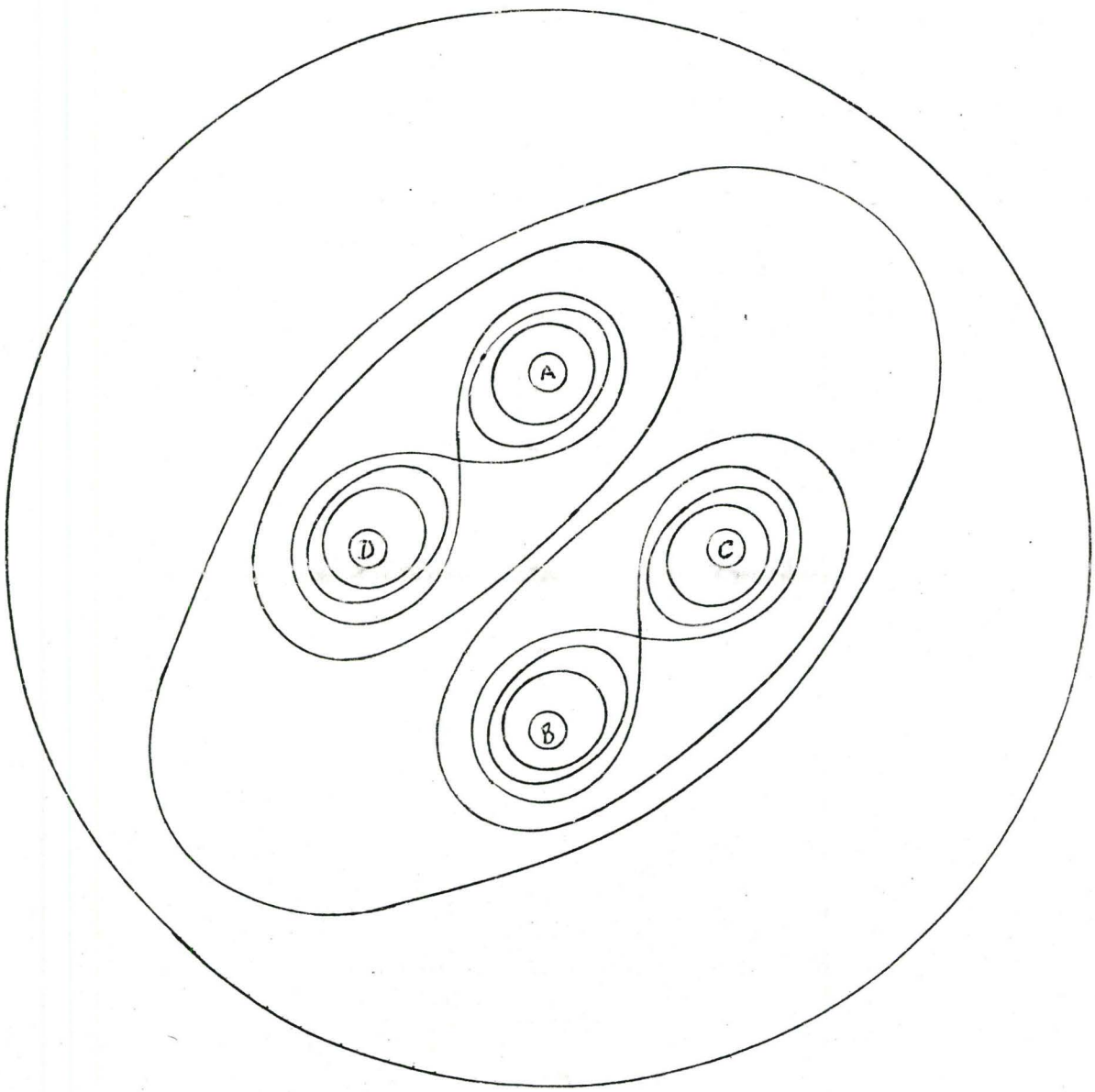

Fig. 3.11: Current Density Profiles in Two-Phase Model. Electrodes of same Phase Adjacent (400 hz)

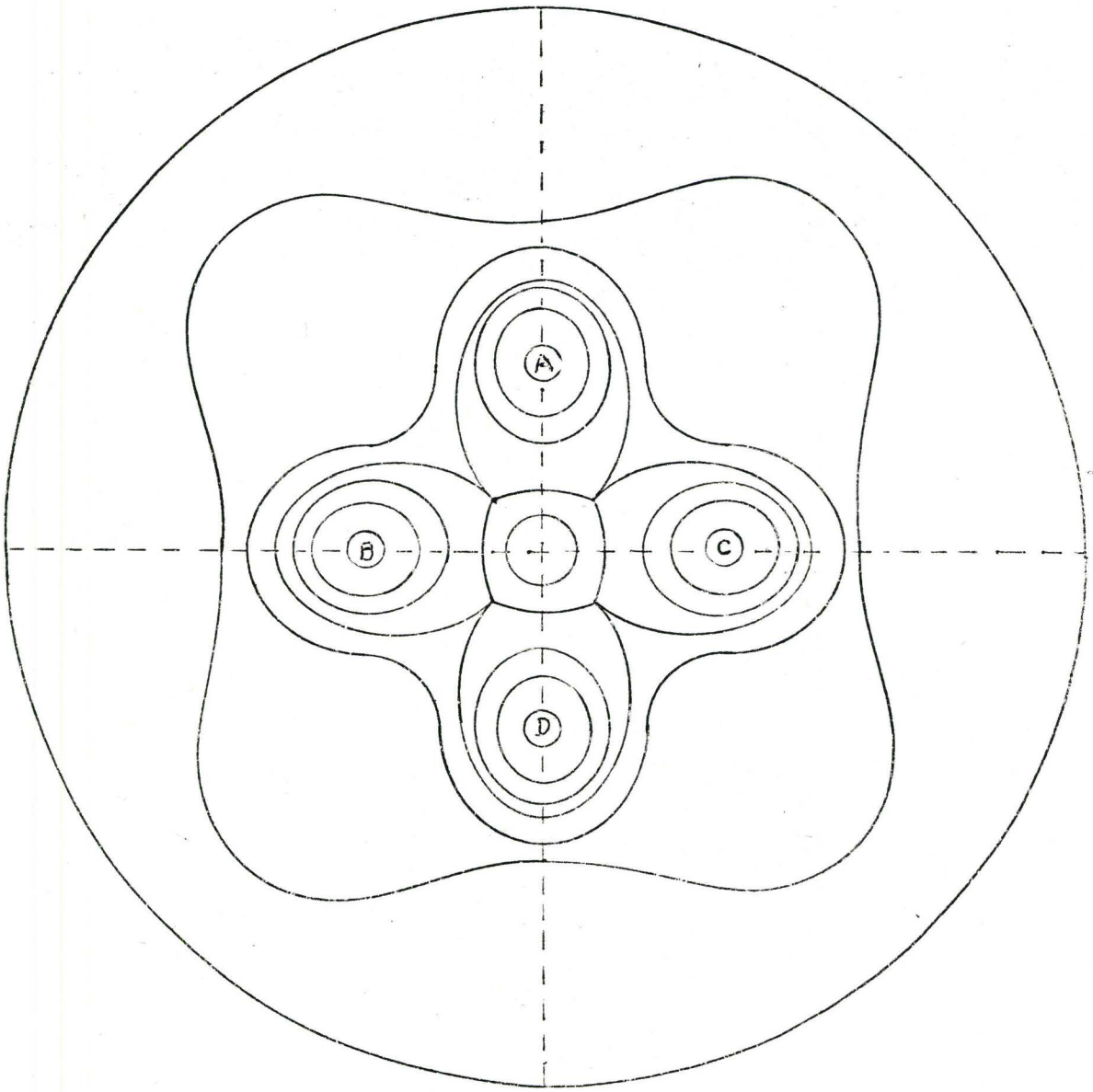

Fig. 3.12: Current Density Profiles in Two-Phase Model. Electrodes of same Phase Opposite (400 hz)

possible arrangements.

Fig. 3.8 shows all the possible arrangements realizable on this system, which, with respect to the bath, may be regarded as a four-phase system. The three-phase system is shown here for comparison. V is the secondary voltage line to line of the furnace transformer.

Fig. 3.9 and 3.10 show respectively the current distribution for electrodes adjacent and opposite. Fig. 3.11 to 3.14 show the approximate equal current contours and current streamlines respectively.

Current density measurements were taken using a copper probe (№ 2 in Table 2.2). This was substituted for the stainless steel probe as it did not require frequent cleaning. Current contours and streamlines were constructed similarly to those in the three-electrode model.

3.4 DISTRIBUTION IN THE FURNACE

The current distribution in the model should well represent the current distribution in the actual furnace. The application of Maxwell's equation to the system (Appendix A) shows that

$$I = 2 \frac{J\delta R}{\sqrt{2}} \cos(\omega t - \pi/4) \qquad \ldots\ldots\ldots 3.1$$

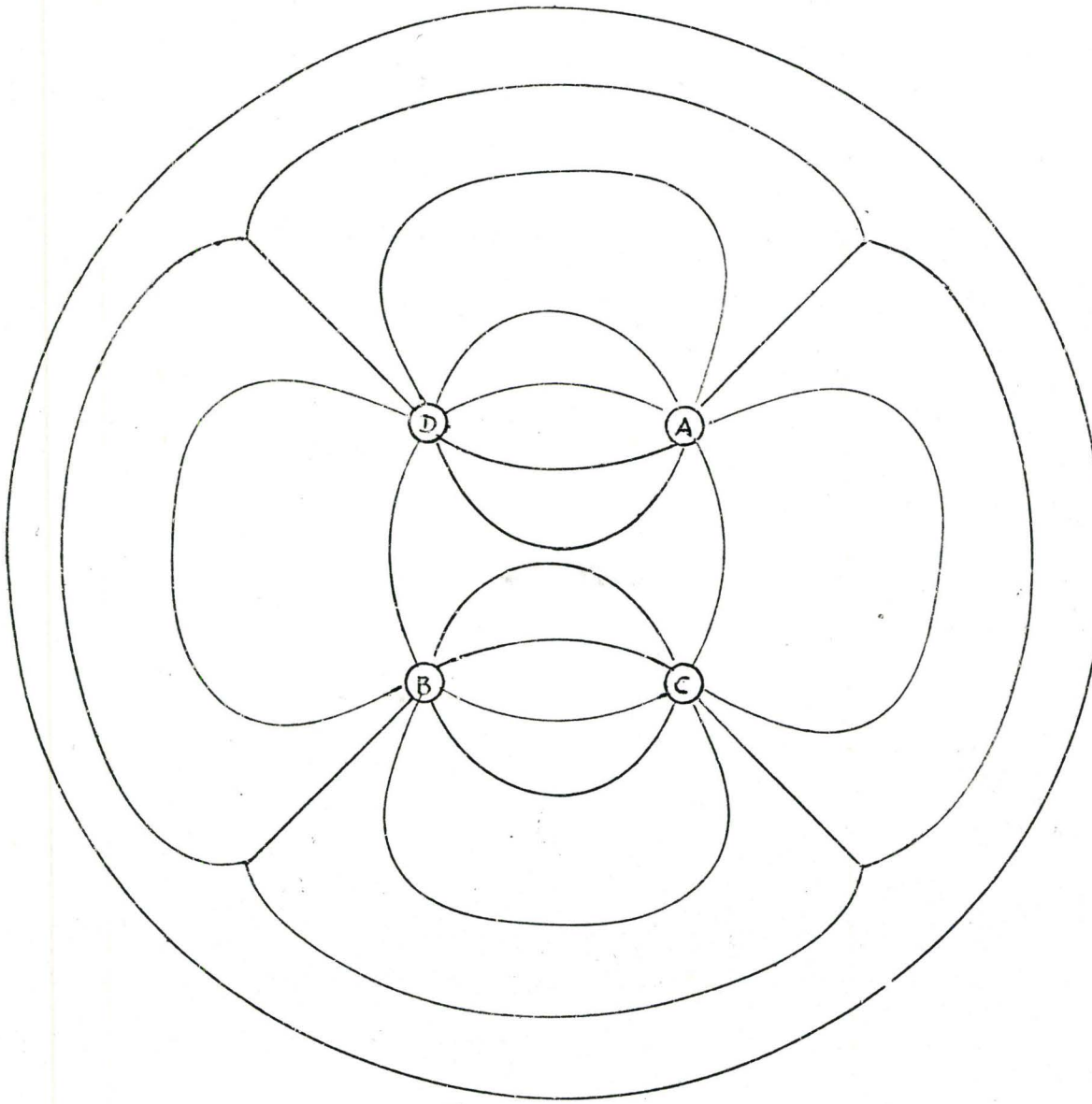

Fig. 3.13: Current Streamlines in Two-Phase Model. Electrodes of same Phase Adjacent (400 hz)

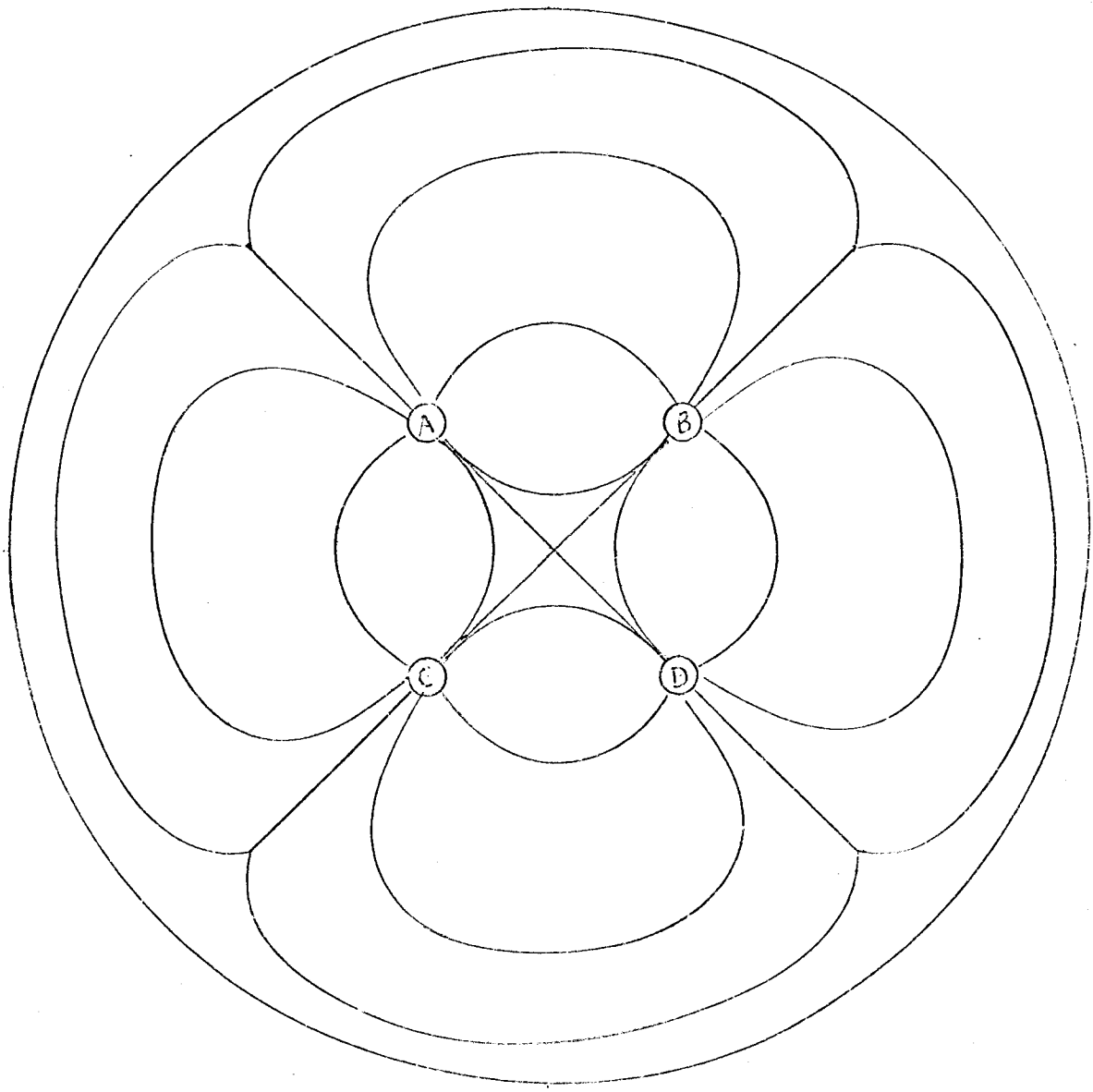

Fig. 3.14: Current Streamlines in Two-Phase Model. Electrodes of same Phase Opposite (400 Hz)

or

$$|J| = \frac{\sqrt{2}|I|}{2\pi R\delta} = \frac{\sqrt{2}|I|}{2\pi R}\sqrt{\pi f\mu\sigma}$$

$$= k|I|\sqrt{f\sigma} \qquad \ldots\ldots\ldots 3.2$$

where $k = \frac{\sqrt{2\pi\mu}}{2\pi R}$ $\ldots\ldots\ldots 3.3$

and I the input (electrode) current.

Equation 3.2 now contains a wealth of information. These may now be stated, and are:-

(1) Since the medium is isotropic and Maxwell's equations are linear, then

$$|J_n| \alpha |I_1 + I_2 + \ldots + I_n| \qquad \ldots\ldots\ldots 3.4$$

where I_1, I_2, I_n are the sources at the boundaries. Hence for equal sources

$$|J_n| \alpha N |I_1| \qquad \ldots\ldots\ldots 3.5$$

and the current density in the medium at any given position and frequency is directly proportional to the current input at the

electrodes.

(2) For a given position and medium, the current density is directly proportional to the square root of the frequency, i.e.

$$|J| \alpha \sqrt{f} \qquad \ldots\ldots\ldots 3.6$$

(3) In referring measurements taken in one medium of conductivity σ_2 to another of conductivity σ_1

$$\frac{|J_1|}{|J_2|} = \sqrt{\frac{\sigma_1}{\sigma_2}} = \frac{\delta_1}{\delta_2} \qquad \ldots\ldots\ldots 3.7$$

Referral of values measured to the actual furnace would therefore involve the following scaling factors:-

(1) Any position (r, θ) in the model would correspond to a position $(C_s r, \theta)$ in the furnace, where C_s is the size scaling factor.

(2) The current input to the furnace is increased by a factor C_I over that in the model; where

$$I \text{ (furnace)} = C_I \cdot I \text{ (model)} \qquad \ldots\ldots\ldots 3.8$$

(3) The current density in the furnace is related to the current density in the model by a factor C_J, where

$$|J| \text{(furnace)} = C_J |J| \text{(model)} \qquad \ldots\ldots\ldots 3.9$$

and

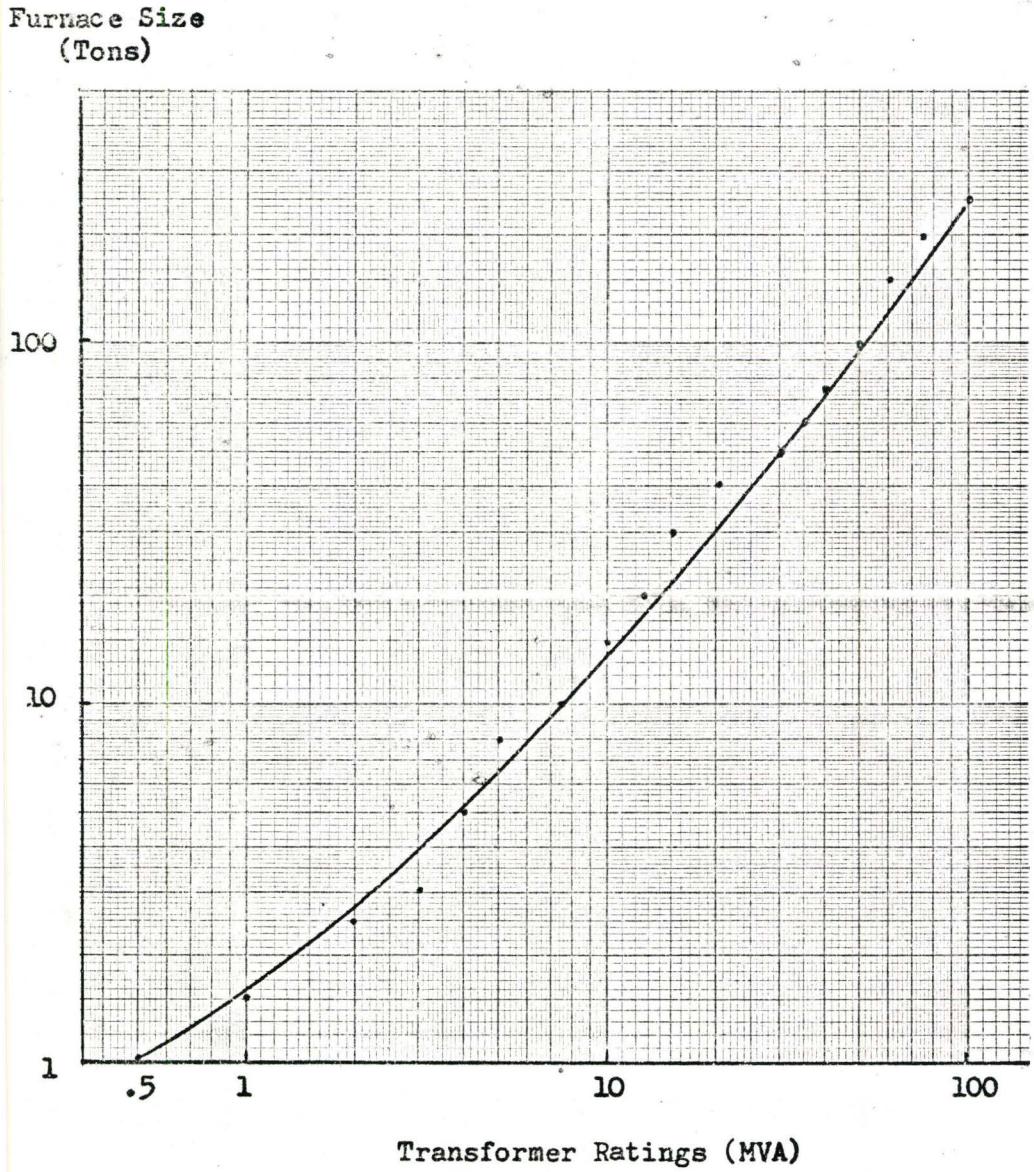

Fig. 3.15: Relationship between Furnace Size and Transformer Rating

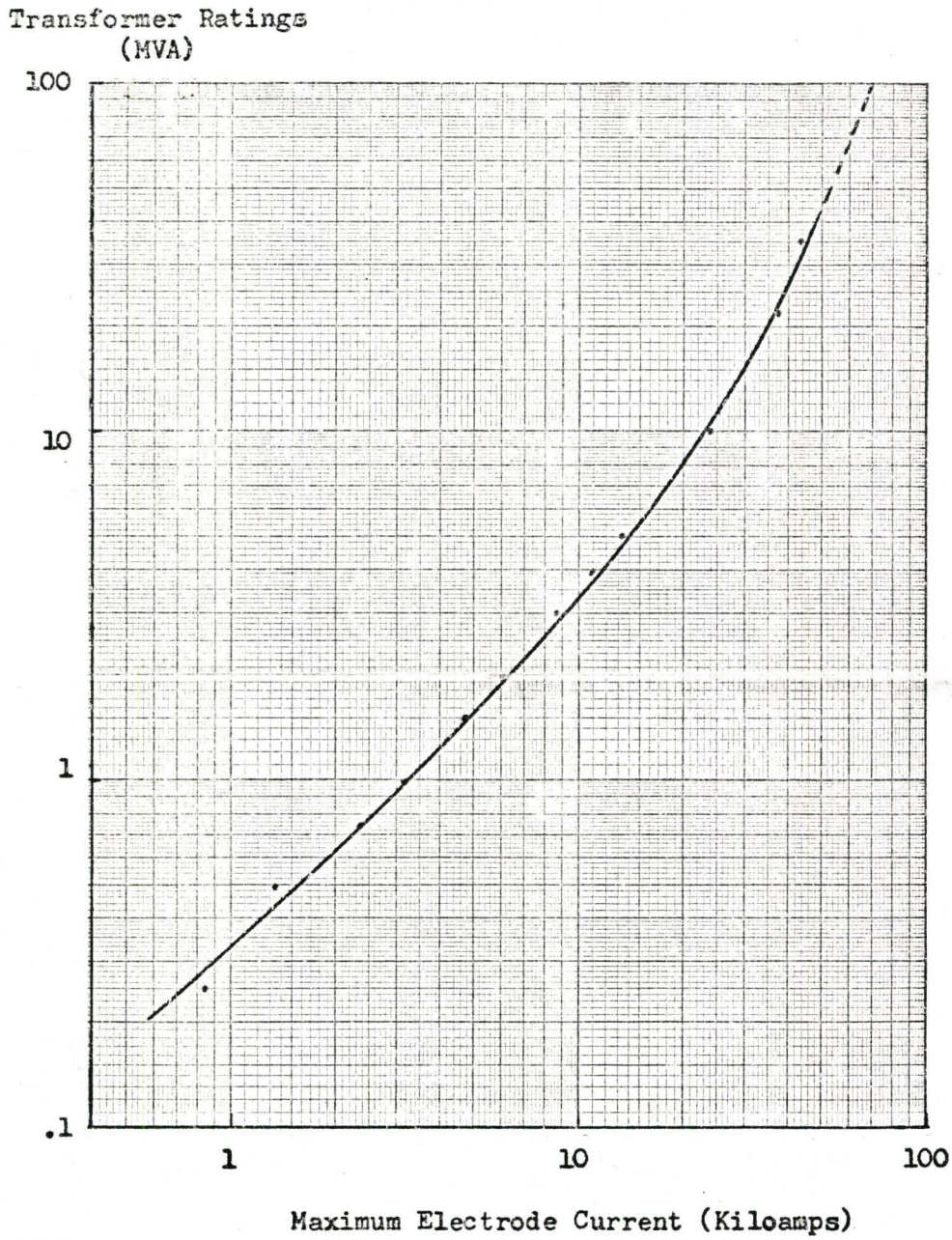

Fig. 3.16: Correlation between Furnace Transformer Rating and Maximum Electrode Current

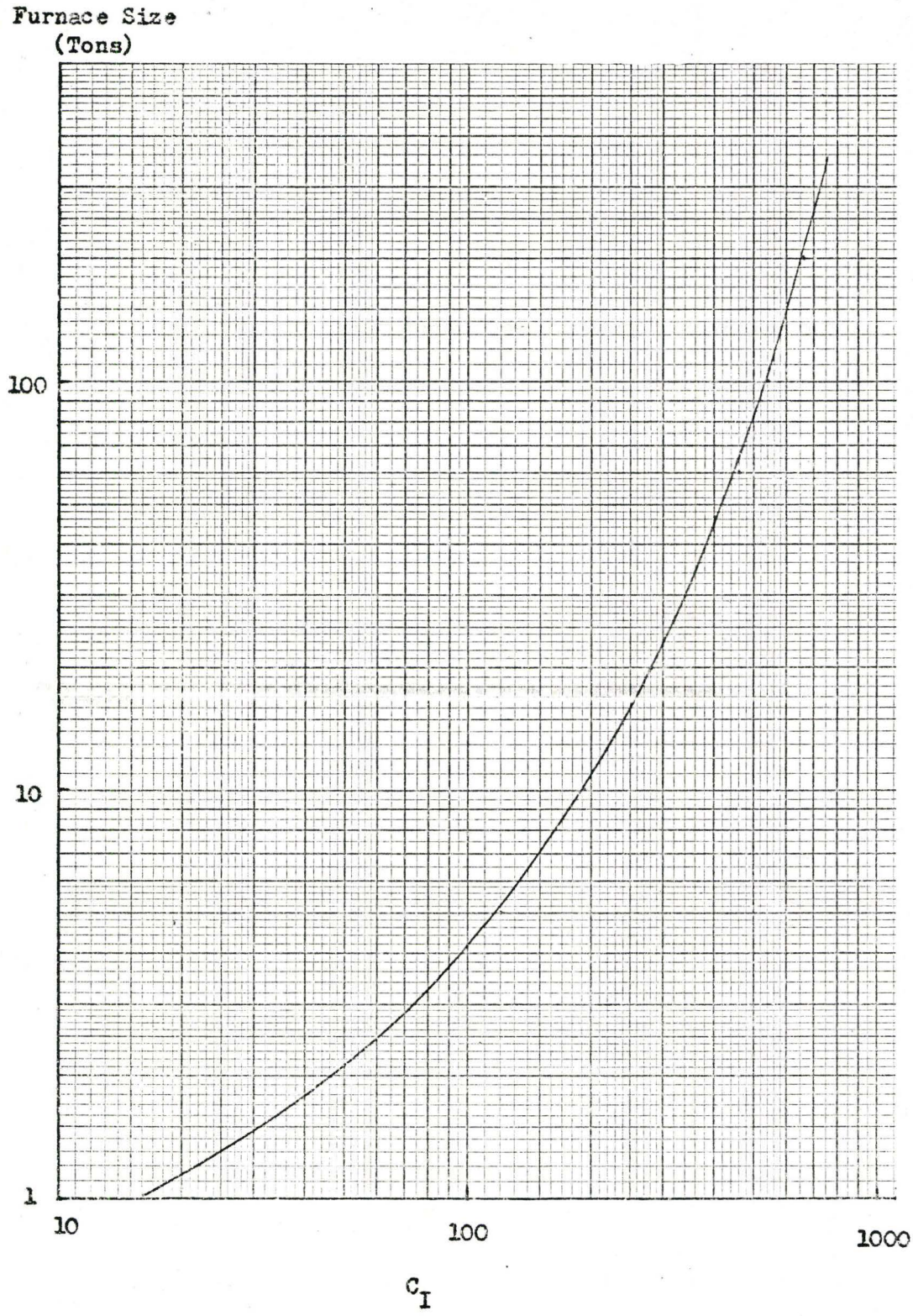

Fig. 3.17: Current Scaling Factor, C_I

$$C_J = C_I \sqrt{\frac{f\ (\text{furnace})}{f\ (\text{model})}}$$

$$= C_I \frac{\delta(\text{model})}{\delta\ (\text{furnace})} \qquad \ldots\ldots\ldots 3.10$$

The only unknown quantity here is the scaling factor C_I. If this value is not known, a reasonable approximation to this value may be obtained from data made available by electric arc furnace manufacturers. Fig. 3.15 shows the correlation between furnace size and furnace transformer ratings . Fig. 3.16 shows the correlation between furnace transformer ratings and maximum electrode current ratings . From this available data, Fig. 3.17 is constructed to show the relationship between furnace size and the current scaling factor C_I. It may be noted here that IC_I is the maximum current rating of the furnace transformer, I being the current input per phase to the model. For convenience the value of I used was 100 amps/phase.

As a check on the validity of the scaling equations used, actual measurements were carried out. Fig. 3.18 demonstrates that equation 3.5 is true in the range taken. If equation 3.6 is also valid, then

$$\log |J| \alpha \tfrac{1}{2} \log f \qquad \ldots\ldots\ldots 3.11$$

and the graph of $\log |J|$ vs. $\log f$ should have a slope of $\frac{1}{2}$.

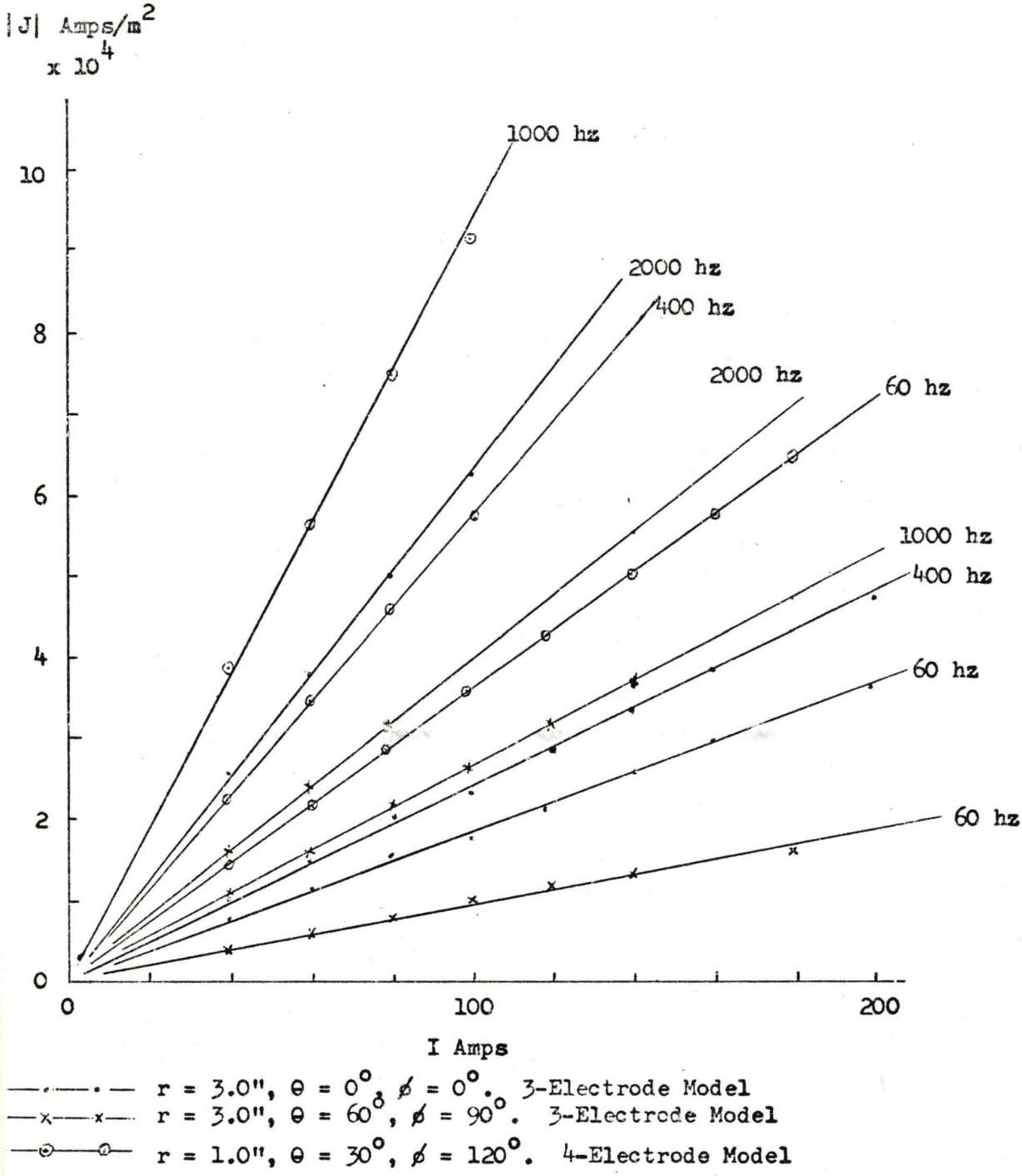

Fig. 3.18: Graph of |J| vs I

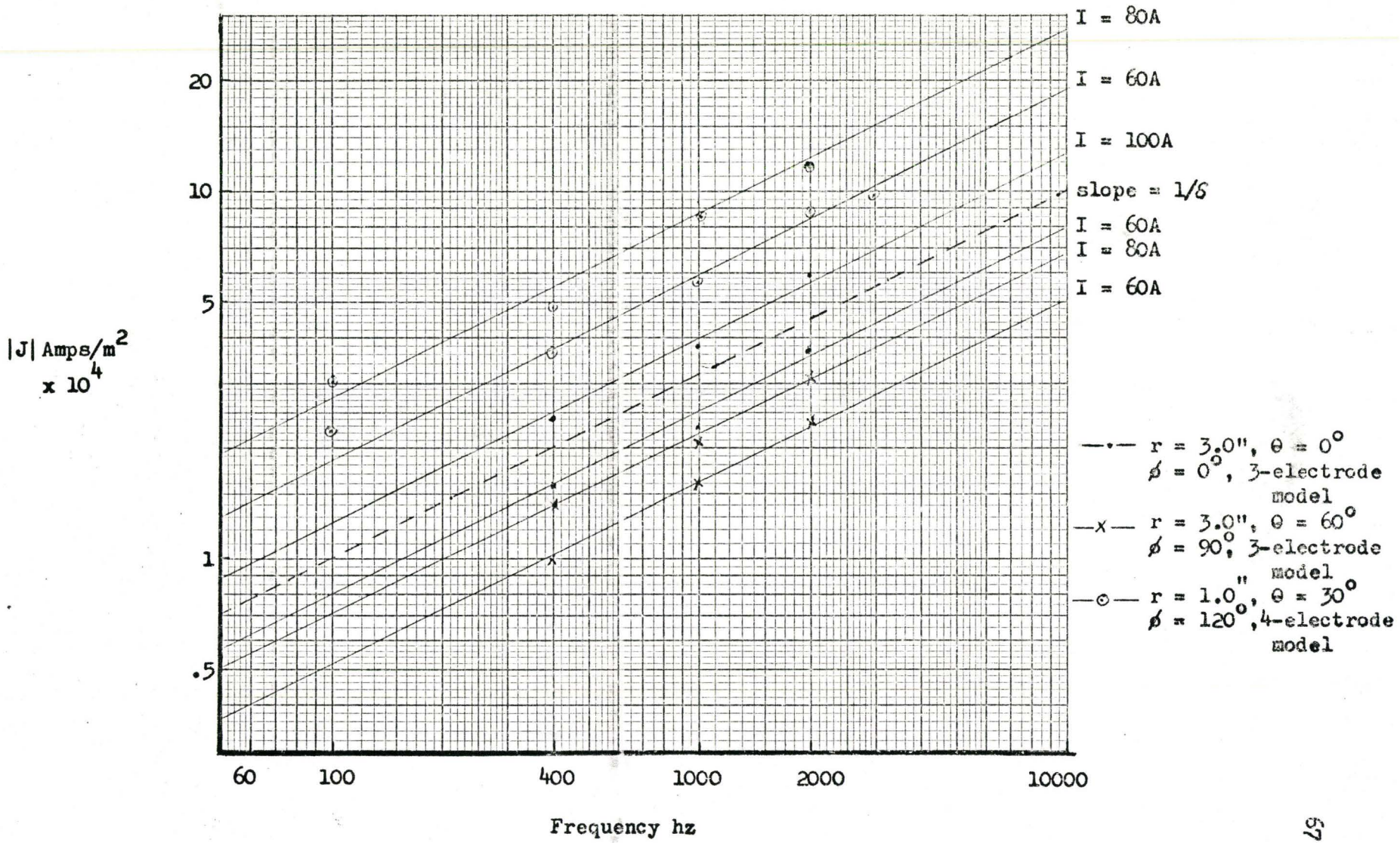

Fig. 3.19: Graph of Log |J| vs log f

Fig. 3.19 shows such a graph, with a line (shown dashed) of slope $\frac{1}{2}$ superimposed. These curves, taken at different positions and input currents, for both the three- and four-electrode systems, all run parallel to this line and also parallel to a line of slope $1/\delta$.

From equation 22, Appendix A, the variation of current density J with depth z is given by

$$J_r = J_{ro} \exp(-z/\delta).\exp(-jz/\delta) \qquad \ldots\ldots\ldots 3.12$$

where J_{ro} is the surface current density. The validity of the assumption that J is constant in the first skin depth (and zero for $z > \delta$) is dependent on the extent to which equation 3.12 applies to the model. Fig. 3.20 shows the measured variation of $\left|\frac{J}{J_o}\right|$ with z (solid lines) for frequencies of 400 and 1000 hz. The dotted lines show the corresponding calculated values. These were obtained by assuming that total reflection of the field occurred at the bottom, which for simplicity of calculations, was taken as a plain surface. Incident and reflected values were added vectorially to obtain the resultant. Fig. 3.21 shows the measured and predicted values of $\angle J_o - \angle J$. The departure of measured from calculated values may be attributed to the fact that the reflection surface is not flat.

At low frequencies, or at points where z is small in comparison to δ, the reflected component is large enough to affect

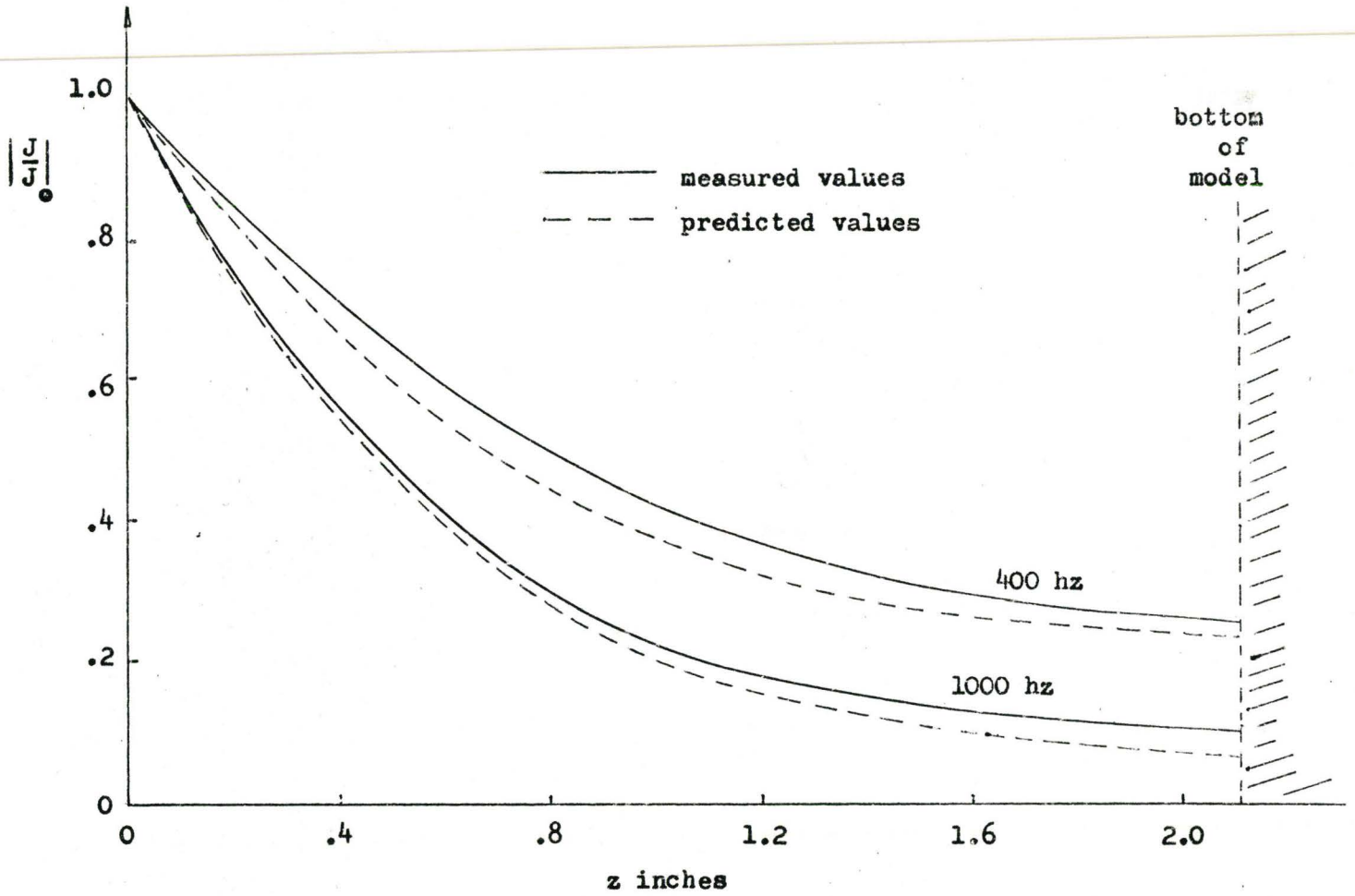

Fig. 3.20: Variation of Normalized Values of |J| with Depth (400 and 1000 hz)

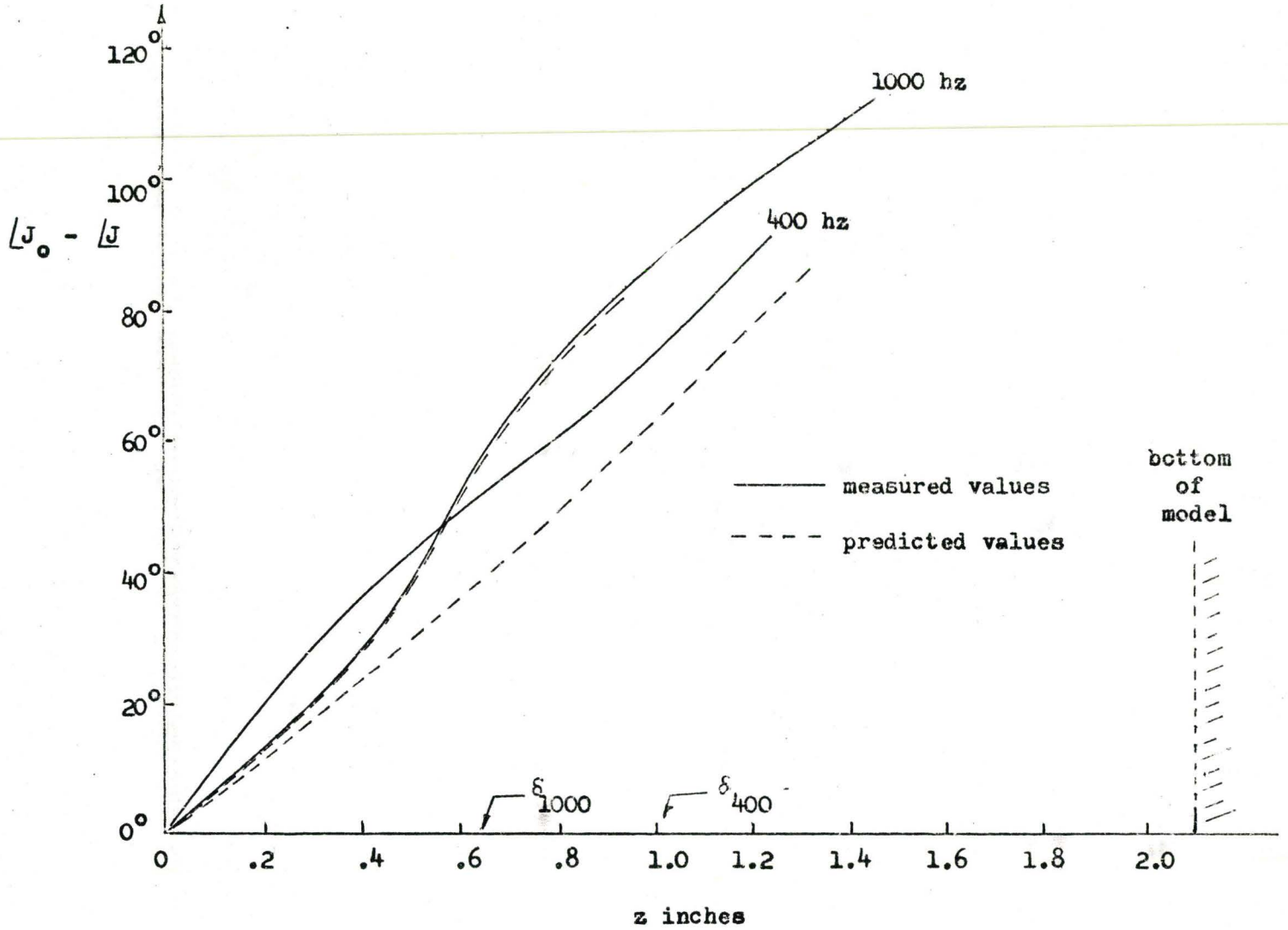

Fig. 3.21: Measured and Predicted Values of Phase at 400 and 1000 hz

the surface value. Here the value of J measured at the surface is not J_{ro}, but the sum of incident and reflected quantities. The approximation is good at points where the reflected field does not affect the surface values. However, with this crude approximation, the maximum difference between measured and predicted values is 5 percent for the magnitude and 12 percent for the phase. The predicted phase angle $\angle J_o - \angle J$ is within the 12 percent limit only as far as the dotted curve. Beyond this the phase changes to leading. However, for both frequencies, this condition exists well after one skin depth.

Since the probe measured the magnitude of J only when aligned with the current, the measurements were taken where the current streamlines run parallel to the horizontal filament. Fig. 3.22 shows the current path below the surface. Here it is seen that probe alignment occurs on lines of symmetry ($\theta = 60^\circ$, 180°, 300° in 3-electrode model, $\theta = 45^\circ$ etc in 4-electrode model).

3.5 HEATING EFFECTS

An attempt may now be made to relate power densities in the model to power densities in the actual furnace.

The power dissipated in a conductor with skin effect is the same as the average power loss produced by having the current distributed uniformly in one skin depth (18). At a chosen point ($r = 2"$, $\theta = 30^\circ$), the current density is 5×10^4 a/m^2 at 400 hz. Referring

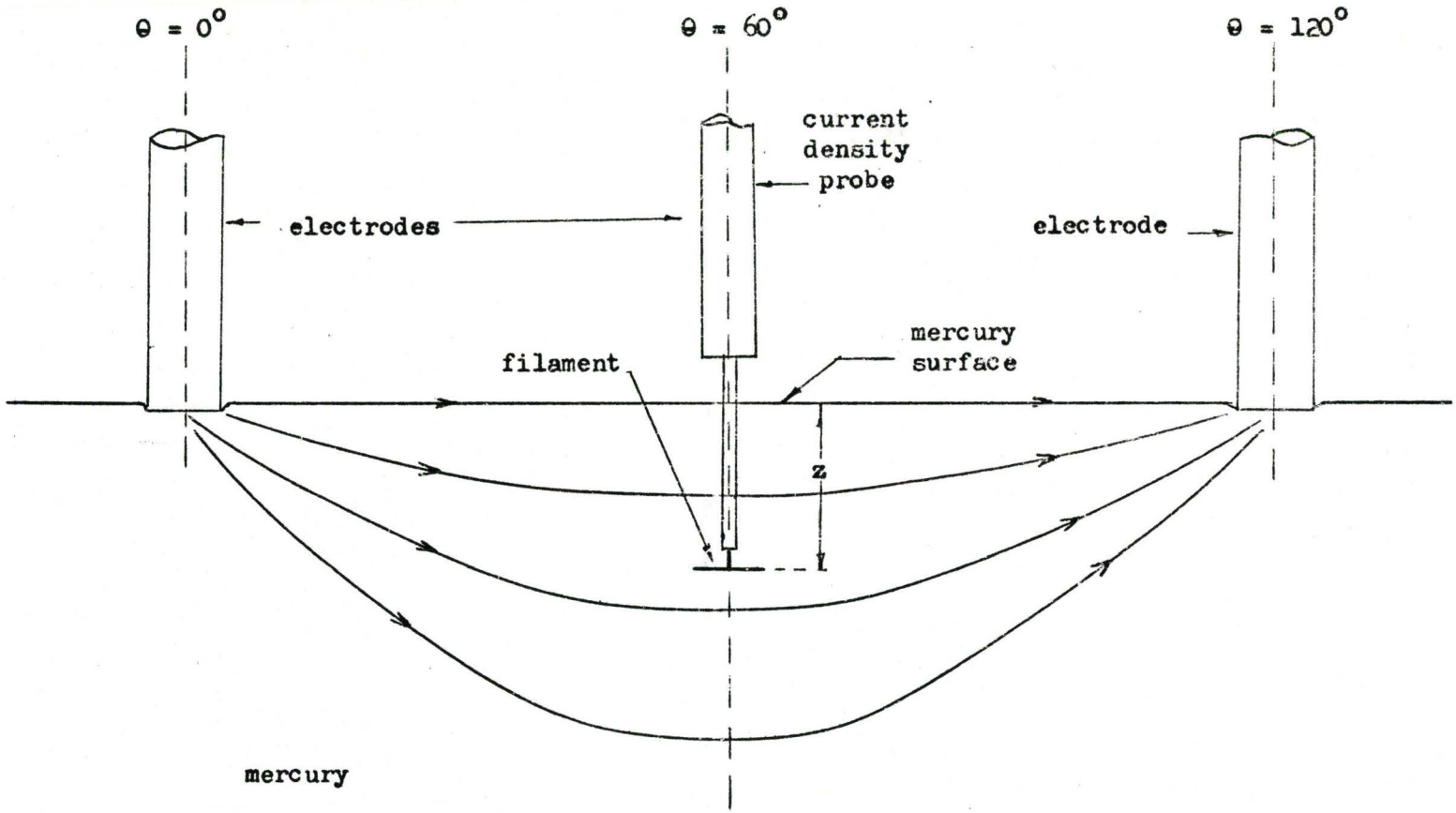

Fig. 3.22: Current Path below Mercury Surface in Three-Electrode Model

these values to a one-ton furnace, the size scaling factor, C_s, is 3.7 (from Fig. 2.1), and the point becomes ($r = 7.4"$, $\theta = 30^{\circ}$). For an r.m.s. current density J^M_{400} in the model (where the subscript refers to the frequency, and the superscripts M to model) the corresponding r.m.s. current density 60 hz is given by equation 3.7

$$|J^M_{60}| = \frac{\delta^M_{400}}{\delta^M_{60}} |J^M_{400}| \qquad \text{.....(3.7)}$$

The corresponding current density in the furnace is given by

$$|J^F_{60}| = C_I \frac{\delta^M_{60}}{\delta^F_{60}} |J^M_{60}| \qquad \text{..... 3.10}$$

$$= C_I \frac{\delta^M_{60}}{\delta^F_{60}} \frac{\delta^M_{400}}{\delta^M_{60}} |J^M_{400}|$$

$$= C_I \frac{\delta^M_{400}}{\delta^F_{60}} |J^M_{400}|$$

The power density at this point in the furnace is given by

$$P^F_{60} = |J^F_{60}|^2 \sigma^F_{60} \quad W/m^3$$

$$= 16.0 \times 5.0 \times 10^4 \times \frac{2.5 \times 10^{-2}}{9.3 \times 10^{-2}}^2 \frac{1}{0.49 \times 10^6} \quad W/m^3$$

$$= \frac{4.62 \times 10^{10}}{0.49 \times 10^{6}} = 9.45 \times 10^{4} \quad W/m^3$$

This power may be considered uniform only in the first skin depth.

The power input capability of a 1-ton (1016 kg) furnace is about 0.5 MVA. Allowing a 70 percent efficiency in the arc, the maximum power input to the furnace is about 0.35 MW. The average power density throughout the entire volume (0.13 m^3) of the metal is

$$P = \frac{0.35 \times 10^{6}}{0.13} \quad W/m^3$$

$$= 2.7 \times 10^{6} \quad W/m^3$$

From these values, the current heating effect appears to be a favourable 3.5 percent of the power input of the arc. However, when viewed with respect to the fact that this power is uniform only in the first skin depth of 3.2 in (0.093 m) and the maximum depth of the furnace is about 10 in (0.254 m) this average value could be less than 1 percent.

It may be reasonable to assume, however, that in the vicinity of the electrodes (or more correctly, the foot of the arc), where current densities are concievably much higher, the heating effect due to current density in the metal could be a sizeable percentage compared to the input power of the arc.

Furthermore, in projecting these values to a larger furnace, where the volume to skin depth is a much smaller percentage of the total volume of the bath, the average heating effect would be much less favourable. From the actual values measured and projections made, it may be safe to conclude that the heating effect could constitute only a very small percentage of the power input to the electric arc furnace.

The overall temperature rise in the model was $5^{o}C$ - from $32^{o}C$ to $37^{o}C$. As the connecting leads to the electrodes attained temperatures of about 75 - $80^{o}C$ during operation, it was difficult to ascertain what portion was due to the inherent heating and what was due to radiation from the conductors. Because of this, no projections can be made concerning the temperature increase due to current density in the model or the furnace. Since this effect is proportional to the square of the current, it may be important at the very high current levels encountered in modern Ultra-High Power arc furnaces.

However, better estimate of this heating effect would be obtained if an equivalent circuit can be found for the liquid metal in the crucible.

CHAPTER 4

FLUID MOTION

4.1 INHERENT MOTION IN FURNACES

Agitation of the bath of an electric arc furnace is beneficial both from physical and metallurgical viewpoints. As a result, some installations use an external induction stirrer, operating on the principle of the linear induction motor, to achieve product homogeniety. Some observers have noted that natural stirring occurs in the electric arc furnace, especially when it is operating in the high-current mode (19).

Similar stirring effects were noted during the operation of the model, and attempts were made to measure the fluid velocity by direct observation of the surface of the mercury. This required cleaning the entire amount of mercury about every two hours to provide a fresh surface for the measurements.

The dilute acid (about 5 - 10 percent) on the surface of the mercury served a dual purpose. Besides helping to maintain a clean surface on the mercury, it also simulated the slag cover in the actual furnace.

During the observations, it was noted that the acid layer moved at a speed that was slightly higher than that of the actual mercury surface. To measure the surface velocity, the time taken for small pieces of copper wire to traverse a known distance was recorded. Average values were determined for both the three and four electrode arrangements.

4.2 MOTION IN THE THREE-PHASE MODEL

Observation of surface motion in the three-phase model disclosed that there was one basic movement. This was the motion of the liquid around the electrodes. The motion was definitely related to the sequencing of phases, a clockwise phase sequence producing clockwise rotation of the mercury, and vice-versa. This local motion about the electrodes caused the entire surface, out to the edges, to rotate in the same sense. The measurements were carried out at 400 hz and 1000 hz, using an input current of 160 amps per phase - about the upper limit of the apparatus over this range.

Perhaps it should be stressed at this point, that the measurements taken were with the object of giving mainly a qualitative comparison of the motion produced in the models. There were at times some flow counter to the main one, and at times, only one or two electrodes contributed to the overall movement.

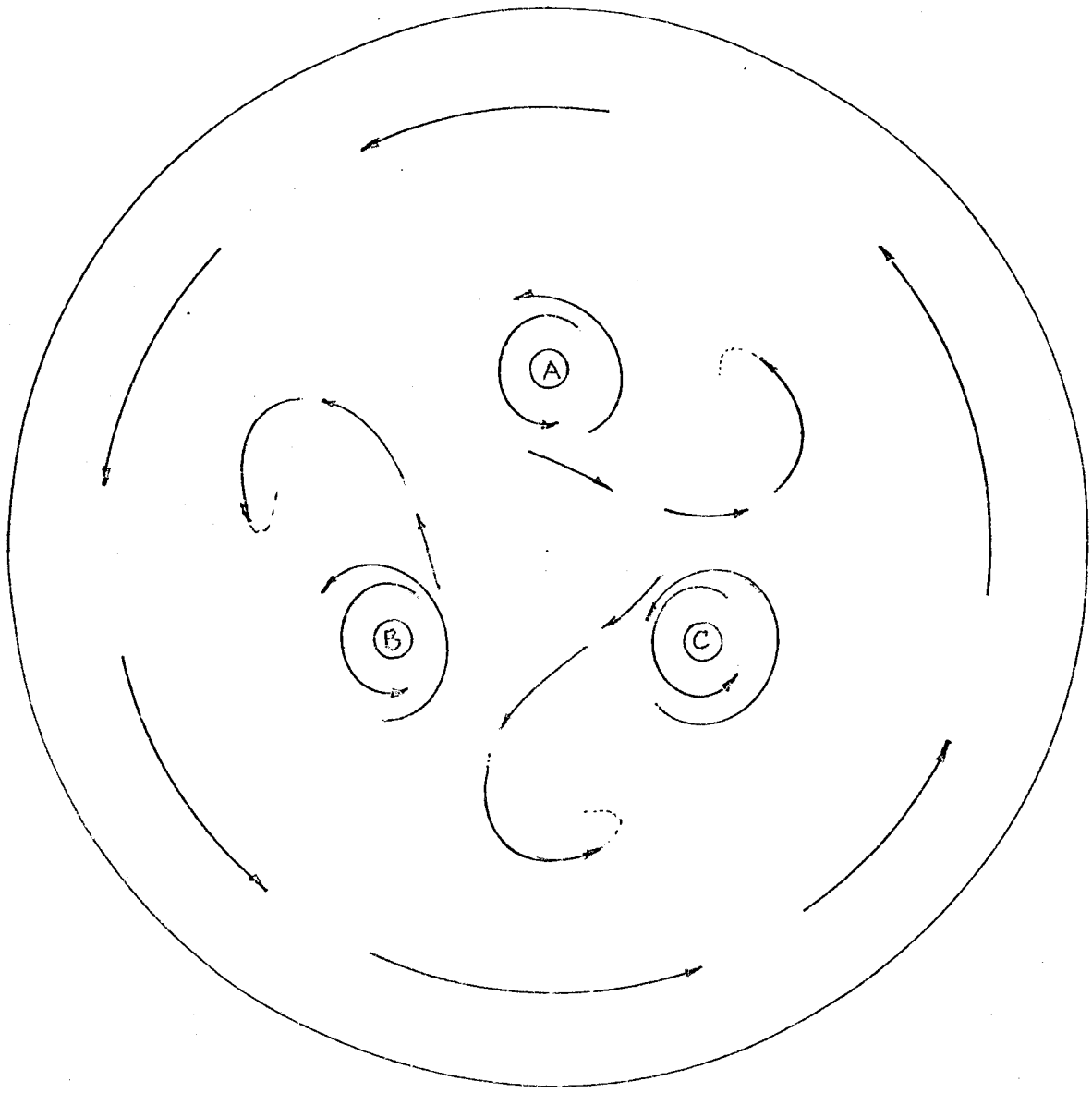

Fig. 4.1: Natural Flow Pattern in Three-Phase Model (Phase Sequence A-B-C)

In measuring the flow around the electrodes, the time taken for a test particle on the surface of the mercury to make 5 revolutions was noted on a stop-watch. Five revolutions were chosen because the particle often failed to make complete revolutions as it was captured by the adjacent electrode. The average of several sets of 5 revolutions on a mean path diameter of about 1 in (0.0254 m) was taken. Values were about the same for both phase sequences. The mean period of revolution of the mercury surface was about 28 seconds, and mean speed 0.28 cm (0.0028 m)/sec.

The speed near to the edge was monitored by a particle about 5.0 in (0.0123 m) from the centre. As counter currents again posed problems, the time taken for the particle to travel one quarter of a revolution was noted. The mean edge velocity in the interval was about 0.17 cm/sec.

Fig. 4.1 shows the main flow patterns in the three phase model. Velocity and flow pattern were about the same at 400 and 1000 hz.

4.3 MOTION IN TWO-PHASE MODEL

The method of taking these measurements were the same as in the three phase model. Here, as before, the main motion was that around the electrodes. However, two basic flow patterns were produced, and depended on whether electrodes of the same phase were

adjacent or opposite each other. Again, the sense of rotation was dependent on phase sequencing.

With electrodes adjacent, the primary motion was again around the electrodes. The directions however were not the same, and created flow currents such that fluid flowed towards the centre along one diagonal and away from the centre along a diagonal at right angles. Fig. 4.2 shows the flow pattern produced by this configuration. For a current input of 160 amps/phase, the speed around the electrodes was about 0.69 cm/sec, and that along a diagonal about 0.36 cm/sec. At the wall, the fluid velocity was low, about 0.2 cm/sec. Values measured at 400 hz and 1000 hz gave speeds around the electrodes that were about the same.

With electrodes of the same phase opposite each other, the flow pattern generated was rather different. In this case, the flows around the electrodes were all in the same direction. The pattern here was quite similar to that in the three-electrode model, and also reversed sense with change in phase sequence. The speed around the electrodes was about 0.63 cm/sec, and that around the edge about 0.28 cm/sec, for a frequency of 400 hz. Measurements taken at a frequency of 1000 hz yielded values that were similar. This indicated that the velocity was more closely related to input current rather than frequency in the range taken, since lowering the input current caused a lowering of the speed.

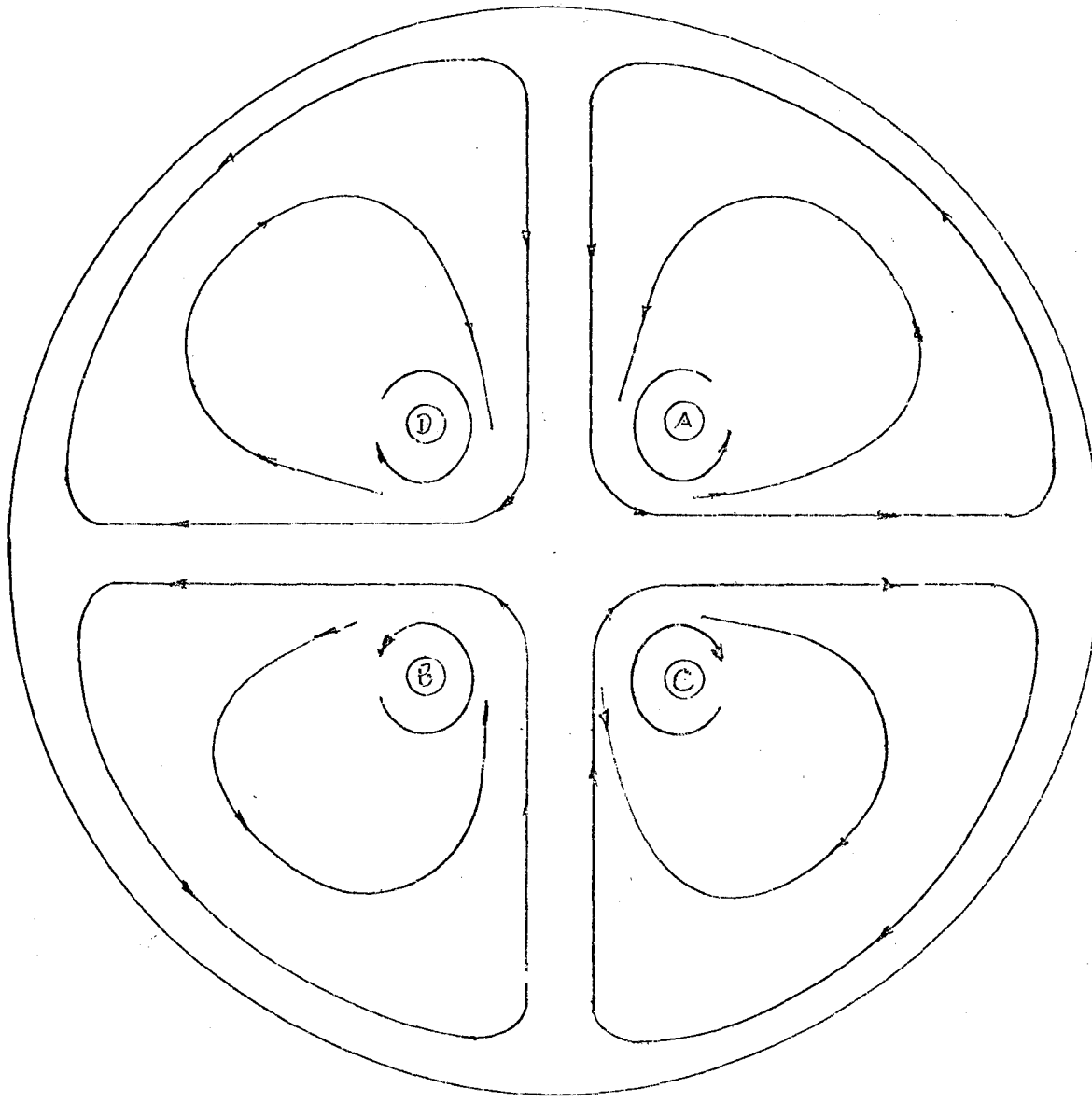

Fig. 4.2: Natural Flow Pattern in Two-Phase Model. Electrodes of same Phase Adjacent (Phase Sequence A-D-B-C)

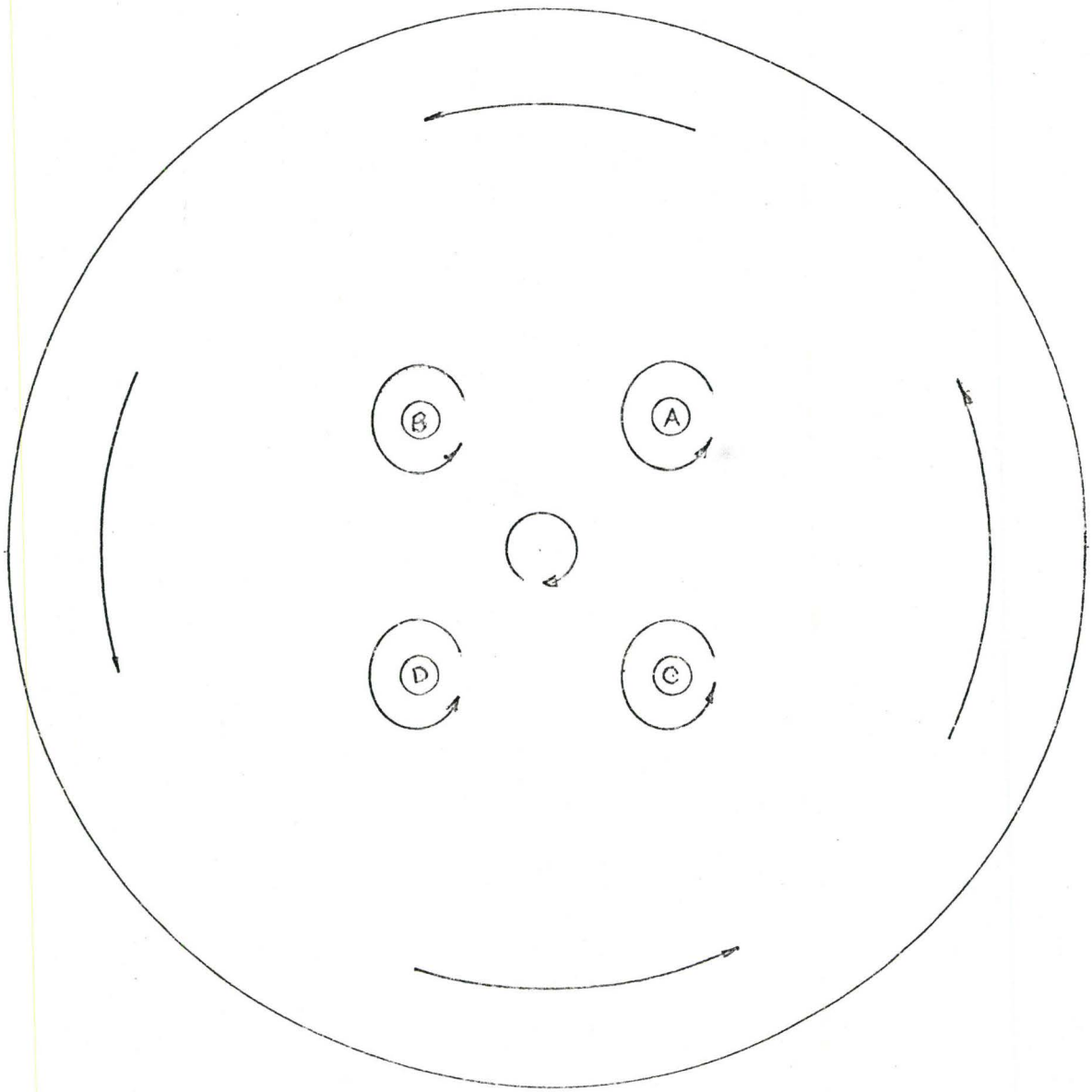

Fig. 4.3: Natural Flow Pattern in Two-Phase Model. Electrodes of same Phase Opposite (Phase Sequence A-B-D-C)

Fig. 4.3 shows the flow pattern for electrodes of the same phase opposite.

4.4 EFFECT OF VANES ON MOTION

Other researchers (8) have shown that the shape of the flow path has a marked influence on the fluid velocity in a channel type induction furnace. Borrowing this concept, an attempt was made to change the flow path in the moded by the insertion of vanes. Fig. 4.4 shows one such arrangement as well as the flow pattern produced for the three-phase model. Only in the very centre of the model did the stirring effects appear to be slightly better than that without the vanes, producing small ripples and eddies. However, flow in the middle region was impeded. The vanes used were made of plasticine to allow rapid and easy change of shape and location. No actual measurements of velocity were taken on the models with vanes, as there appeared to be no really significant improvement in fluid flow. Further, the presence of vanes in the actual furnace would create more problems than they solve by hampering the charging of scrap to the furnace. They could also seriously interfere with the actual melting patterns, since during the meltdown period, heat transfer from the arc is by radiation.

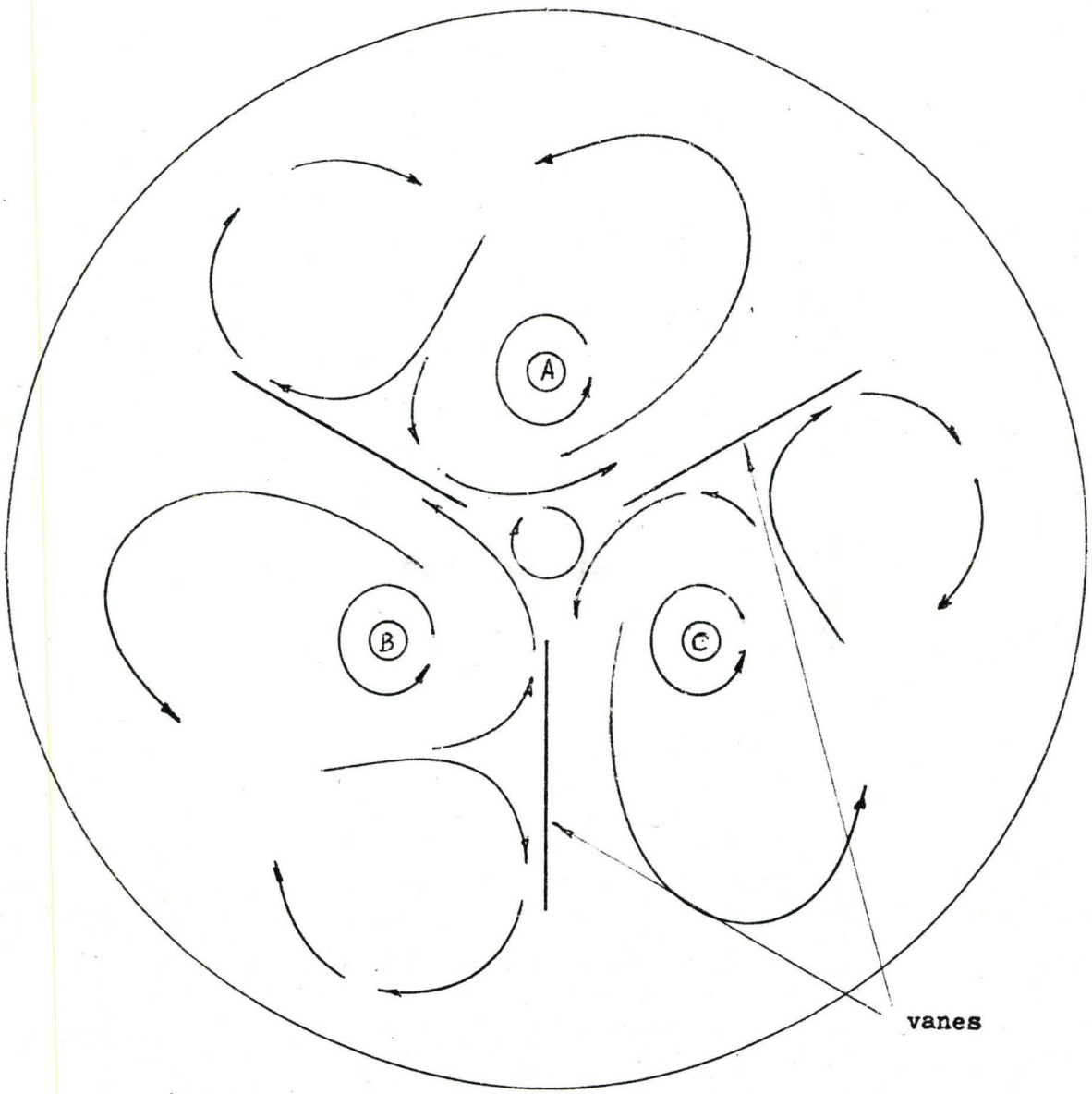

Fig. 4.4: Effect of Vanes on Flow Pattern (Phase Sequence A-B-C)

4.5 ELECTROKINETIC EFFECTS

As mentioned in section 4.1, the use of an external induction stirrer is at present the most common means of stirring in the electric arc furnace. As an alternative to this, it was decided to investigate the use of auxillary electrodes to achieve this end.

The criteria of an acceptable alternative were set as

(a) The electrical circuit containing the auxillary electrodes should be operable on existing commercial supplies of electricity, or supplies easily derived therefrom.

(b) The energy input to the auxillary system should be very small compared to the energy input to the furnace.

(c) The system should be simple, easily added to an existing furnace, and cost little in terms of installation and maintenance, and finally

(d) The stirring produced by the addition should be significantly above that otherwise observable.

The first idea was to make use of electrodes contacting the mercury in the model. This was considered undesirable for one main reason. In a real furnace, the most easily available and economic electrode, would be the graphite electrode. This would dissolve in steel, increasing the carbon content. The system was however,

attempted on the three phase model, using three auxillary electrodes on a three phase system. This arrangement did not seem satisfactory in terms of additional stirring, and produced patterns similar to the original three-phase supply to the model. In fact it looked rather like changing the power supply to the model from three to six-phase. The input power requirements were about similar to that in the model producing no striking effects.

Allowing the electrodes to touch only the acid solution was next attempted. The effects produced may be related to the electrokinetic phenomena which occur at the interface of two dissimilar liquids (Appendix B), and were observable on both alternating and direct currents.

With alternating current, standing waves were produced on the surface of the mercury and the acid. There was no doubt that the effect was produced by the flow of current through the acid and mercury as a visible pattern could be seen, marking the path of current flow between the auxillary electrodes, similar to the current streamlines associated with the main electrodes.

In addition to the standing-wave pattern, there was motion of the acid and the mercury surface around the electrodes and in the general area between the electrodes. Motion in the main was not uni-directional, but consisted of several small swirls directed towards the electrodes. The presence of a small amount of gassing at the

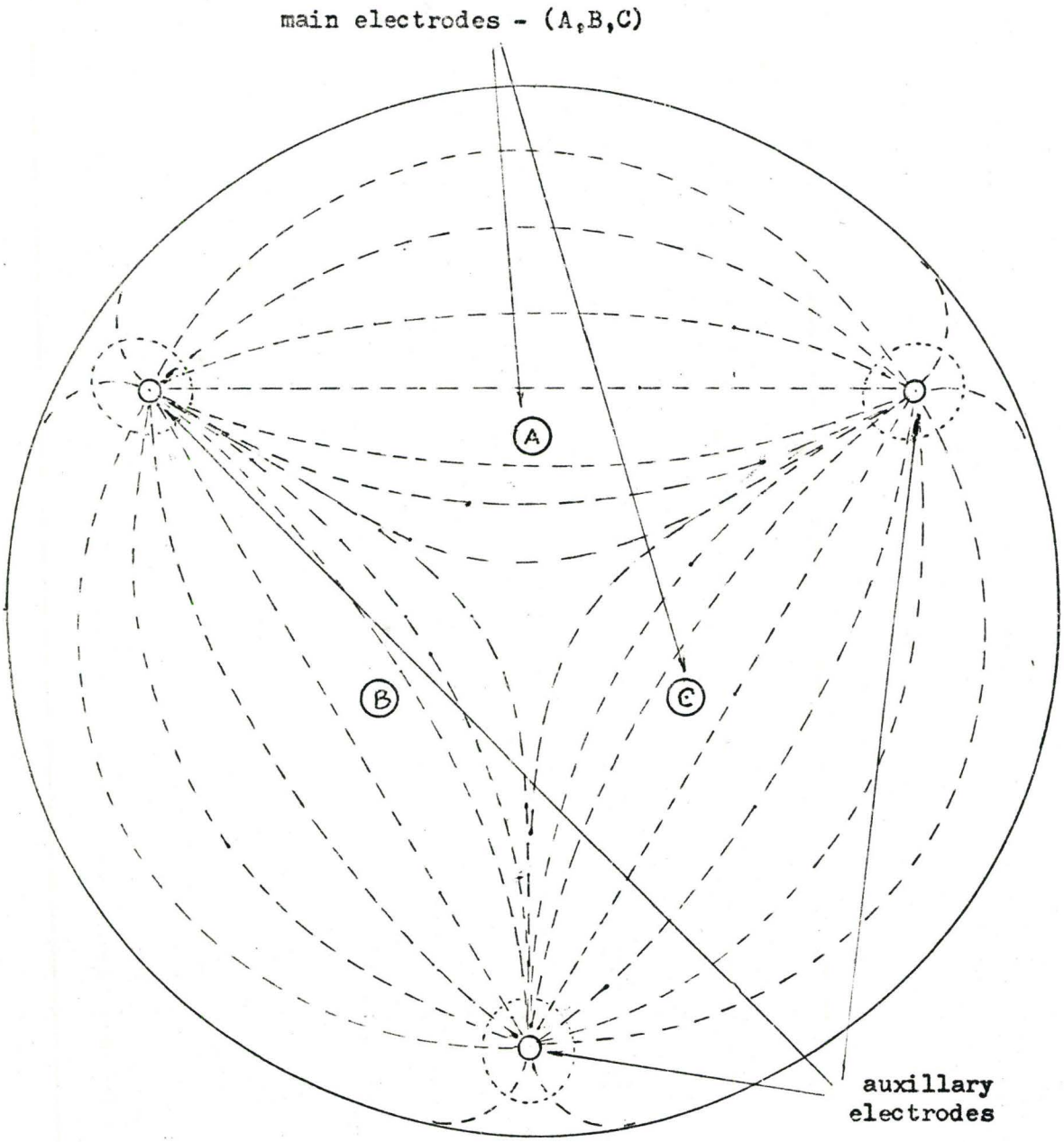

Fig. 4.5: Electrocapillary Action using Alternating Current

electrodes indicated that some amount of electrolysis was taking place. Good stirring action was obtained using 10 volts at 0.15 amps. The intensity of the action depended on the current strength, while the voltage requirements were decided by the conductivity of the acid.

Actual velocity measurements were not taken because of the difficulty of observation of the motion of particles, but the surface activity may be well described as greatly improved. Estimated velocity however, was about 1 cm/sec, and the auxillary electrodes about 1 in (0.025 m) from the edge. Though it augmented the natural motion occurring in the model, the action was independent, and effective by itself (Fig. 4.5).

The effect of frequency on the surface oscillations was investigated. Above 60 hz, the amplitude of the oscillations decreased with increasing frequency and at about 1000 hz, the effect all but disappeared. However, the size of these oscillations increased as the frequency was decreased. At a frequency of about 0.1 - 0.5 hz, a condition similar to resonance was obtained, where the oscillations became fairly large.

On direct current, the effect was more marked than on alternating current. Fig. 4.6 shows one arrangement used. At the negative electrode, not much motion was noticed, though there was

slight gassing. Small, everwidening ripples, like those produced by a small stone on a placid pond, were seen to spread slowly from this electrode. The surface of the mercury immediately under the electrode seemed to be depressed by an estimated one millimetre.

At the positive electrodes, an area of mercury initially about one inch (0.0254 m) in diameter was raised about one millimetre upwards, towards the electrodes. This area increased in size until it reached the nearest edge, accompanied all the while by a turbulent motion. Again no surface velocity measurements could be accurately taken, because of the turbulence of the flow, but it was estimated to be in excess of 3 cm/sec, using a 10-volt dc supply at 0.2 amps.

In some cases, the raised areas around the positive electrodes joined together to form one larger area occupying about half the surface of the model. A dividing line separating the 'positive surface' from the 'negative surface' could be clearly seen.

Motion in general was at the positive electrode in a direction away from the negative electrode. Fig. 4.7 shows the stages in the development of the flow. That the mercury surface at the positive electrode rose during operation was confirmed by observation at the wall of the model in the area where the flow reached the wall. The elevation here could be clearly seen above the rest of the surface.

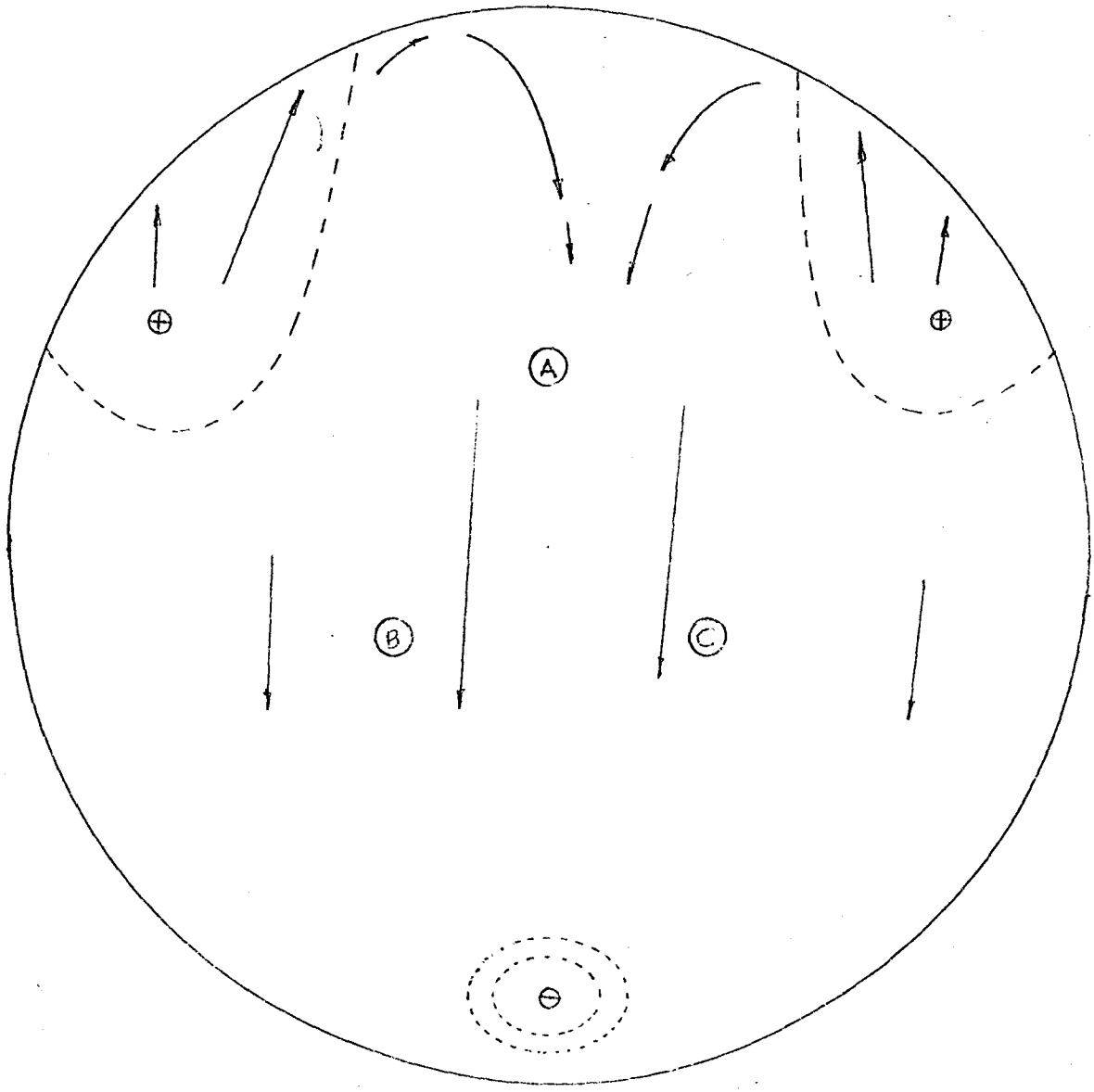

Fig. 4.6: Electrocapillary Action using Direct Current

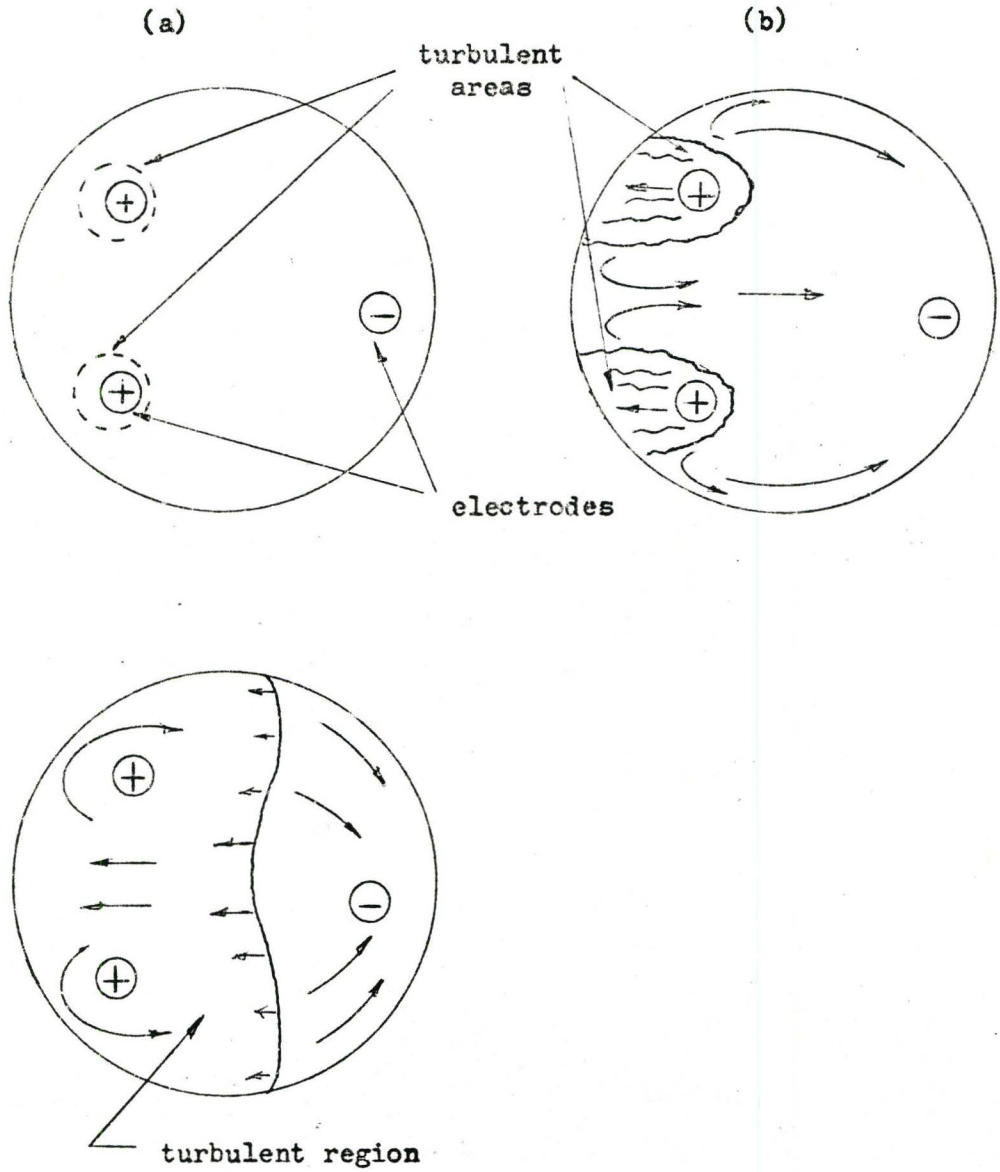

Fig. 4.7: Stages in Development of Electrocapillary Action on Direct Current

A variation of this was to allow the negative electrodes to touch the mercury surface, and the positive electrodes only the acid. Though this appears to contradict a previous statement to the effect that this is undesirable, the apparent contradiction may be easily removed if it is noted that in the actual furnace, the refractory is a fair electrical conductor at the temperature of molten steel. The refractory may then be used as the negative electrode. In this case however, the active areas merged and after sometime took over the entire surface of the model. At this condition activity became much reduced, and similar to that at a negative electrode. Reversing the polarity for a short while reactivated the surface. The notion was similar to that in the previous case, with a slightly higher current input.

The effect of the combination of both direct and alternating current on the electrokinetic effect was also investigated. The combination was produced by feeding the output of a function generator having a variable dc offset voltage, into a dc power amplifier. This produced the combined effects of ac and dc motion, giving both vertical oscillations and horizontal movement of the mercury. Best results were obtained with the function generator set to give a low frequency (~0.5 hz) square wave output.

CHAPTER 5

DISCUSSION AND CONCLUSIONS

5.1 DISCUSSION

5.1.1 THE AIM

The aim of this thesis was to determine current distribution and metal flow in the hearth of an electric arc furnace.

Metal flow (stirring) has been observed in arc furnaces. Explanation of this phenomena, however, is not given in current literature.

This investigation constitutes an initial attempt to discover what happens and explain effects observed in the hearth of the furnace. Since no mathematical model of the hearth has ever been developed, an analog method was used, and experiments were carried out on a scaled model of the furnace.

The Model: Analog modelling techniques were applied in the development of a suitable scale model of the hearth. Since the hearth and its model are geometrically similar, current distribution is identical when the ratio of diameter to skin depth is made the same.

In the model of the hearth, mercury represented the liquid steel. The modern trend is towards large furnaces with high metal output. Here, the diameter is large (15-32 ft) compared with skin depth ($\sim$4 inches at 60 hz). A 1-ton furnace is considered the smallest size of furnace of commercial interest. Scaling was such that a model of diameter 1 ft simulated a furnace of capacity 1-ton at 400 hz and one of 100-tons capacity at 8.4 khz. Operation of the model at frequencies below 400 hz, where it represented an arbitrarily small furnace, resulted in reflection of the electromagnetic fields at the boundaries (sides and bottom) - an effect not occurring to that extent in an actual furnace. This produced significant distortion in the current distribution pattern and the metal movement. Operation of the model at and above 400 hz give results which are predictable with good accuracy (within 12 percent).

5.1.2 CURRENT DISTRIBUTION

Current Density Measurements: Predictions have not been attempted regarding current density as a function of position. Values have been determined by actual measurement on the model using current density probes. Measurements were mainly at the surface of the mercury at a frequency of 400 hz. It has been predicted and experimentally verified at frequencies of 400 hz and above, that (1) Current density is a linear function of the current input, and varies directly as the electrode current,

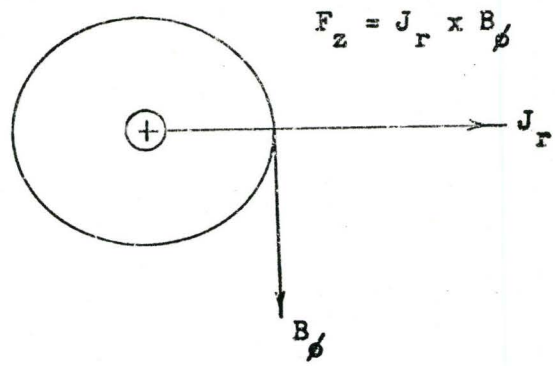

(a) Current Down into Electrode

B_ϕ is Magnetic Flux Density

Due to Electrode (Arc) Current

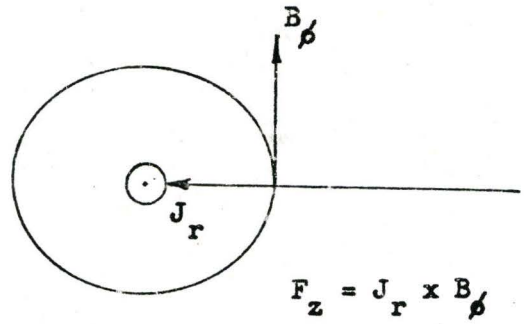

(b) Current up into Electrode

Fig. 5.1: Forces on Surface under Foot of Arc

(2) Current density, for a constant electrode current, varies directly as the square root of the frequency (or inversely as the skin depth), and

(3) Current density varies exponentially with depth, with the ratio (depth/skin depth) as the exponent. Since reflection occurs at the bottom, this variation with depth is more accurately expressed as the sum of an increasing and a decreasing exponential (hyperbolic cosine). As a result, measurements taken on the model at a single frequency in the range 400 hz and above, can be related to values at any other frequency in that range. Hence one set of measurements can be used to determine current density in furnaces of any given size.

Results taken were used to construct approximate current streamlines and profiles of equal current density.

Heating Effects: An attempt was made to relate current density to heating effects due to losses (J^2/σ) in the liquid metal, relative to arc heating. An evaluation of this is best obtained using an equivalent circuit for the liquid metal in the hearth. This however, demands the use of a mathematical model, which has not yet been developed. In the method used, a typical value of current density near the electrodes was chosen. Assuming that this value exists uniformly throughout the liquid steel, the heating effect was determined as a percentage of the total input power for a one-ton furnace. The result obtained indicates that this upper bound for the heating effect is about one percent of the total power input to the

furnace.

Some general observations may be made with reference to forces produced by the current in the furnace.

Surface Depression under Arc: Depression of the surface of the slag and steel under the foot of the arc has been observed in electric arc furnaces. This effect is explained by Fig. 5.1. Here, J_r is the surface current density in the liquid metal and B_ϕ the magnetic flux density due to current in the arc. The force density F_z is given by

$$F_z = J_r \times B_\phi \qquad \ldots\ldots\ldots 5.1$$

Since F_z is downwards, the conductor, in this case the liquid metal, moves downwards, creating a depression in the surface. This is especially true near the foot of the arcs where current densities are high. Reversal of current direction in the arc reverses both J_r and B_ϕ, leaving the direction of F_z unchanged.

Arc Flare: Arc flare is described as the rapid and sudden motion of the arc towards the sidewalls, and is considered a main contributor to furnace wall erosion. As mentioned above, the metal surface under the foot of the arc is depressed. As the arc is a flexible conductor, a force equal to F_z pushes upward on the arc,

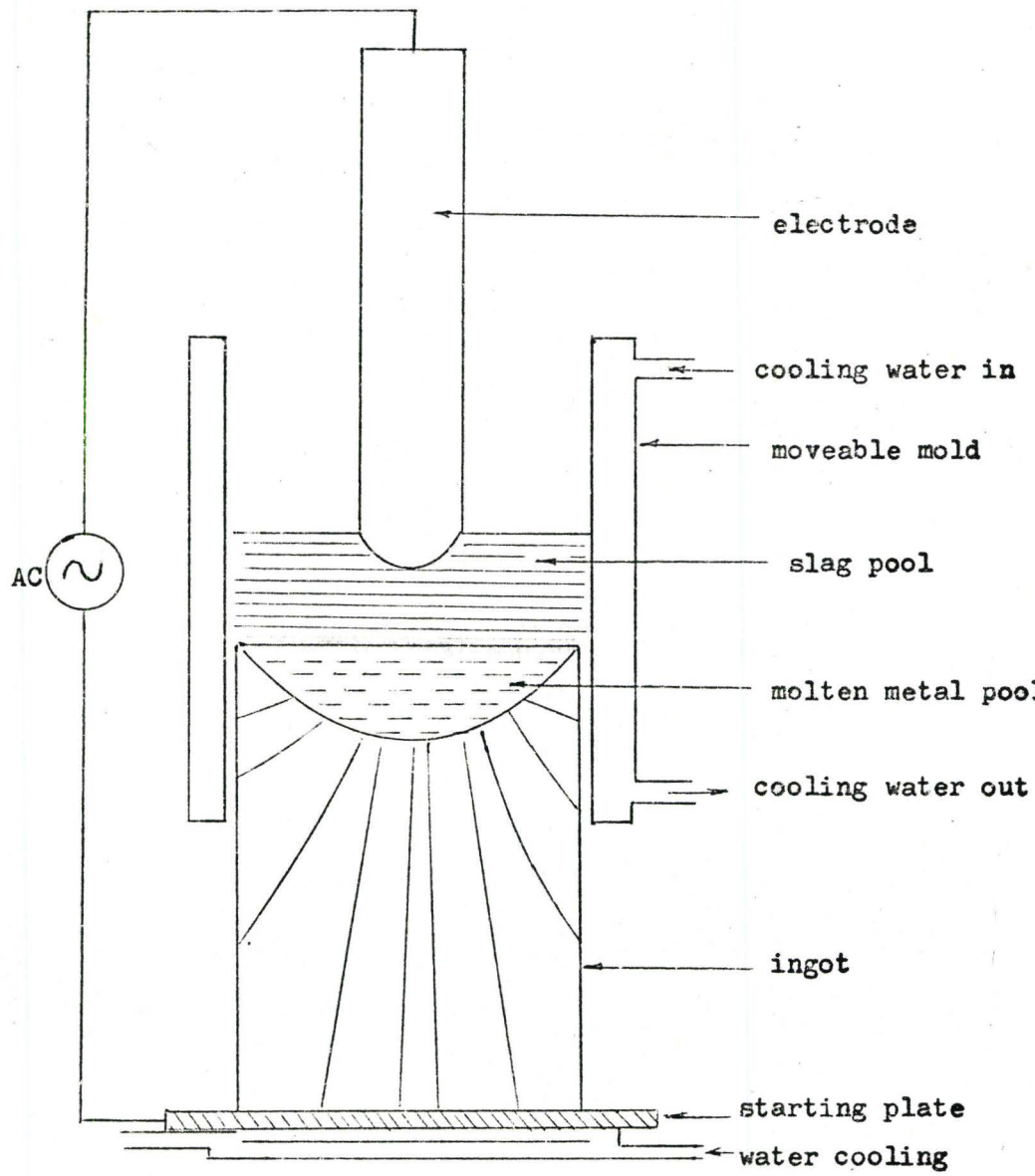

Fig. 5.2: Features of a Typical Electroslag Remelting Furnace

moving it away from the surface and towards the sidewalls. The problem is further complicated by the presence of three arcs in a furnace, each bearing currents differing in phase and direction from the others. Electrodynamic forces varying in proportion to the current in each arc would cause movement of the foot of the arc across the liquid metal surface. Strictly based on observations made on liquid metal movement, in which electrodynamic forces move the liquid around each individual electrode, it is postulated that the foot of the arcs also move around the electrodes twice each cycle.

5.1.3 MOTION

The motion observed can be divided into two categories - naturally occurring and artificially produced.

Naturally Occurring Motion: This has been observed in electric arc furnaces and in both the coreless and channel-type induction furnaces, where it has been used to advantage. This effect was observed in the model of the arc furnace hearth. Here, the flow was around each electrode, and in a direction that always matched the phase rotation of the electrode supply. Flow velocity remained constant at frequencies of 400 and 1000 hz for a given input current. A similar study in modelling the channel-type induction furnace (8), indicated that sustained flow was a function of channel geometry and frequency. Flow velocity at 1000 hz was half that at 400 hz in a model of comparable size, disappearing completely at 3000 hz. It was also found that flow occurred only when channel width was less than

twice skin depth. In the arc furnace model, the depth of the hearth near the electrodes was about twice skin depth at 400 hz, and about three times skin depth at 1000 hz. From this result, the mechanism of flow appears different for the electric arc and channel furnaces. This difference could not be further substantiated in the laboratory, since equipment limitations prevented operation of the model at a high enough frequency, at a comparable power level, to enable a study of the effect of frequency on flow over a sufficient frequency range. An attempt was made to enhance metal flow in the arc furnace model by a slight modification of flow geometry. Fluid path geometry was changed by inserting vanes of insulating material in the model. This however was not considered practical in an actual furnace, as they would affect adversely the heating and melting pattern existing in a furnace without significantly increasing flow.

Artificial Motion: Artificial motion was also produced in the model. This was done with the aid of a system of auxillary electrodes. The effect produced using the auxillary electrodes is reasonably well explained by the electrocapillary curve in Appendix B. This electrokinetic effect is due to surface properties, and as such, it is difficult to determine the extent to which it penetrates into the mercury. Even as a surface effect however, it should find application in a real furnace, since the surface is the site of the reactions between molten metal and slag. In fact, it is noted in industry that the use of alternating current during electroslag remelting (22) provides a more active refining bath. This phenomena is considered to be due to the constant changing of polarity of ions in

the molten metal. For some grades of steel, this process provides the best combination of desulphurization and degree of refining. Fig. 5.2 shows a typical electroslag remelting furnace used in the production of large ingots from the remelting of smaller ones.

5.1.4 TWO-PHASE SYSTEM

The two-phase (or 4-phase) system may well serve as an alternative to the present three-phase design. The possible advantages of this system include:-

(1) A more uniform melting pattern in the furnace. Assuming a constant power in the arc i.e. a power in each arc equal to that in the three electrode design, the weight of steel melted per electrode is smaller. This could produce a more even melting pattern.

(2) Decrease in meltdown time. Because of the higher power input, the meltdown time should be reduced to about 3/4 that in the present system.

(3) Better refining: With electrodes of the same phase opposite, the stirring produced would be more intense. With electrodes of the same phase adjacent, in addition to being more intense, the flow pattern is such as to move fresh materials near the sidewalls into the high temperature and reaction zones near the arc.

(4) Lower mutual coupling between phases. For the high currents used in electric arc furnaces ($\sim$50 to 100 kilo-amps) mutual coupling between phases increases the reactance and limits the power input to the furnace for a given transformer. If the two conductors to each

phase are placed side by side, coupling between phases would be minimised. Further, if conductors to each phase are co-axial, the coupling should be almost entirely eliminated.

The system however, is not without its disadvantages. These are likely to be:-

(1) Shorter refractory life. With four arcs in the furnace, the refractory life should be shorter. The extent to which this is shortened is dependent not only on power input, but also on arc length and arc flare. The radiant energy impinging on the furnace walls is fairly predictable, hence the increase in heating of the walls may be calculated.

(2) Increase in size and number of hot spots. Since there are now four arcs, there are now four hot spots. These may be larger since the thermal energy reaching the walls is increased. This may require reducing power input to each phase or moving the electrodes closer to the centre of the furnace.

(3) Greater initial expenditure and possibly maintenance costs. The addition of an extra electrode would require such changes as another hole in the roof, another electrode arm and positioning controls etc. However, if this saves on the cost of power consumption through lower reactances, and in operation through shorter meltdown times and higher output tons per hour, it may be worth the additional expense involved.

(4) Phase conversion. Since the supply to the electrodes is two-phase, and the commercially available supplies of electrical energy are three-phase, a special furnace transformer would be needed.

This would require special taps and connections to effect the three- to two-phase conversion. As such, this transformer may be more expensive than the present type used. It is noted however that the furnace transformer is normally of special design, hence it would appear that the phase conversion may not add significantly to the cost.

5.2 FUTURE WORK

Prediction of Current Distribution: Future work on current distribution involved the prediction of current density for a given hearth shape and electrode configuration. Analytical techniques involving the use of complex-potential theory in a multipolar and cylindrical co-ordinate system is capable of generating the basic patterns. Extension of the method to include skin effect and boundary conditions should yield good results.

A successful method of prediction would be of importance to a study of the submerged arc or electric resistance furnace, where the charge is heated entirely by the passage of current. While in the hearth of the electric arc furnace this heating effect (J^2/σ) is secondary, in the resistance furnace this is the source of heating.

Application of Electrocapillary Action: Future work in this area is the test of the applicability of this method of stirring on a scale larger that attempted so far. This would be done on a larger

scale model, or an actual full size, electric arc furnace. This method is of course not limited in application to the electric arc furnace. Being an independent system it could be used on any type of furnace for melting or holding metals provided that a slag cover is present.

5.3 CONCLUSIONS

This investigation was exploratory in nature with the aim of determining current distribution and metal flow in the hearth of an electric arc furnace, by simulation on a model. This objective was attained in the following ways:

Known analog modelling techniques have been successfully applied to the development of a small scale model of a typical electric arc furnace, using the skin depth to diameter ratio as a main parameter.

Experimental results were obtained to demonstrate that current distribution may be predicted for furnaces of different sizes and ratings from measurements taken using one model only.

Natural stirring was observed in the model of the electric arc furnace, and was found to be dependent on the phase rotation of the supply to the electrodes.

Electrokinetic stirring was produced and examined, using auxillary low power electrodes.

An alternative two-phase, four-electrode design for an electric arc furnace has been proposed. This is expected to improve energy input and power distribution relative to the standard three-phase design. A reasonable basis of this expectation has been verified by tests on the two models.

APPENDIX A

RELATION OF CURRENT DISTRIBUTION TO INPUT CURRENT

It is possible to relate the current distribution J_r to the electrode current I, by application of Maxwell's equations to the system. To do this, it is assumed that the liquid metal surface is a cylinder of radius R, and infinitely long (Fig. A1). Since the medium of isotropic and the equations are linear, only one electrode (or arc) is considered, and for simplicity, only one boundary condition.

Maxwell's time varying equations are given as (17,18)

$$\nabla \times H = \frac{\varepsilon \partial E}{\partial t} \qquad \ldots\ldots\ldots 1$$

$$\nabla \times E = -\mu_o \frac{\partial H}{\partial t} \qquad \ldots\ldots\ldots 2$$

$$\nabla \cdot E = 0 \qquad \ldots\ldots\ldots 3$$

$$\nabla \cdot H = 0 \qquad \ldots\ldots\ldots 4$$

Taking the curl of both sides of equation 3.2

$$\nabla \times (\nabla \times E) = -\nabla \times \frac{\partial H}{\partial t} \qquad \ldots\ldots\ldots 5$$

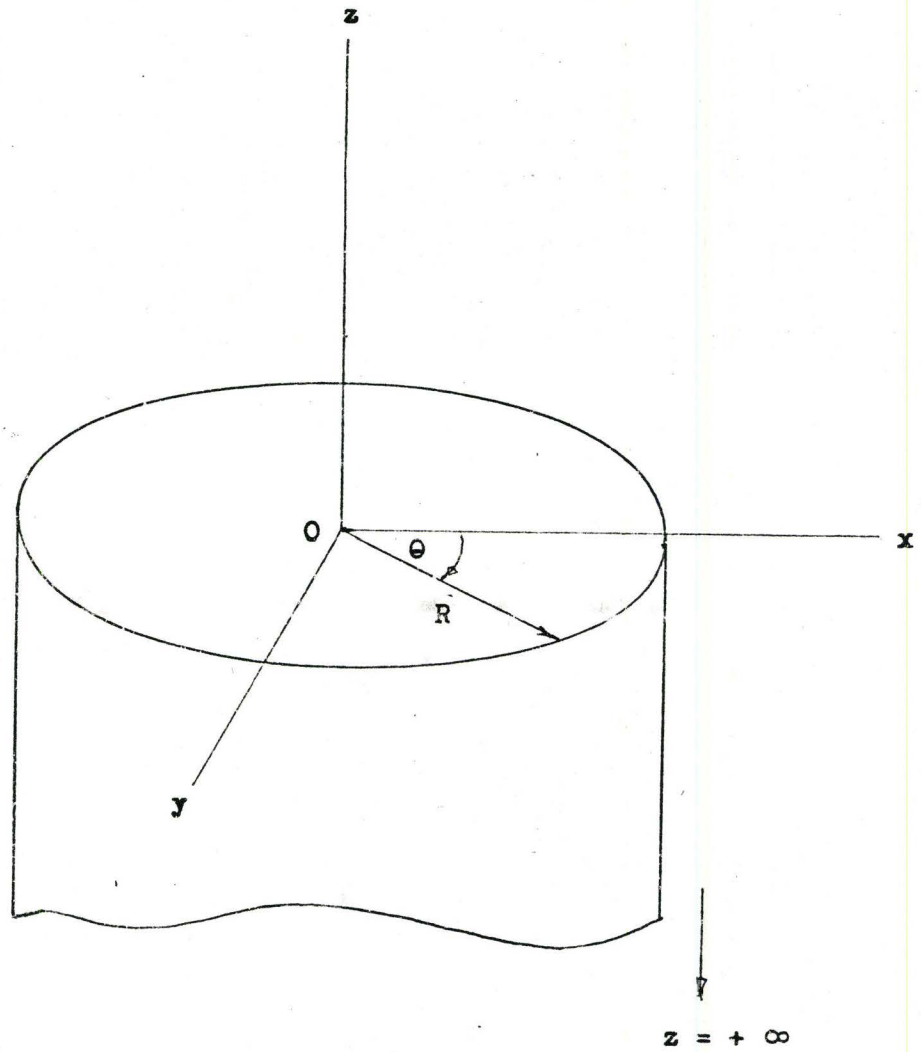

Fig. A1: The Model as a Cylinder of Infinite Length

On expanding and simplifying, equation (5) yields the wave equation

$$\nabla(\nabla \cdot E) - \nabla^2 E = \varepsilon\mu \frac{\partial^2 E}{\partial t^2} \qquad \ldots\ldots\ldots 6$$

Since from (3)

$$\nabla \cdot E = 0 \qquad \ldots\ldots\ldots 3$$

the wave equation reduces to

$$-\nabla^2 E = \mu\varepsilon \frac{\partial^2 E}{\partial t^2} \qquad \ldots\ldots\ldots 7$$

If cylindrical coordinates are used then

$$\frac{1}{r} \frac{\partial}{\partial r} \left(r \frac{\partial E}{\partial r}\right) + \frac{1}{r^2} \frac{\partial^2 E}{\partial \theta^2} + \frac{\partial^2 E}{\partial z^2} = -\mu\varepsilon \frac{\partial^2 E}{\partial t^2} \qquad \ldots\ldots\ldots 8$$

The solution of this equation is of the general form

$$E_r = (\theta)\, R(r)\, Z(z)\, T(t) \qquad \ldots\ldots\ldots 9$$

If as a simple solution only the Z(z) and T(t) components are considered, then

$$E_r = Z(z)\, T(t) \qquad \ldots\ldots\ldots 10$$

One solution of this equation is

$$E_r = E_{ro} \exp(-z\sqrt{\pi f \mu \sigma}) \cos(t - z\sqrt{\pi f \mu \sigma}) \quad \ldots\ldots\ldots 11$$

or substituting for the skin depth

$$\delta = \sqrt{\frac{1}{\pi f \mu \sigma}} \quad \ldots\ldots\ldots 12$$

$$E_r = E_{ro} \exp(-z/\delta) \cos(\omega t - z/\delta) \quad \ldots\ldots\ldots 13$$

where E_{ro} is an arbitrary amplitude factor, evaluated at $z = 0$, $t = 0$.

This field in the conductor may now be related to the external field at the surface of the conductor. If the origin of the coordinates is placed at the surface, then in the region $z>0$, the medium is a perfect conductor, and for $z<0$, the medium is a perfect dielectric.

At the boundary surface, $z = 0$, and

$$E_r = E_{ro} \cos \omega t \quad \ldots\ldots\ldots 14$$

This is now considered as the source field which establishes the fields within the conductor.

Since in a good conductor the displacement current is negligible, then

$$J = \sigma E \qquad \ldots\ldots\ldots 15$$

and the conduction current density at any point within the conductor is given by

$$J_r = \sigma E_r$$

$$= \sigma E_{ro} \exp(-z/\delta) \cos(\omega t - z/\delta) \qquad \ldots\ldots\ldots 16$$

The time average power density into the conductor, as given by the Poynting theorem is p_z

$$p_z = \frac{1}{2} \frac{E_{ro}^2}{\eta} \qquad W/m^2 \qquad \ldots\ldots\ldots 17$$

where η is the intrinsic impedance of the conductor

$$\eta = \sqrt{\frac{j\omega\mu}{\sigma + j\omega\varepsilon}}$$

Since for a good conductor $\sigma >> \omega\varepsilon$

$$\eta = \sqrt{\frac{j\omega\mu}{\sigma}}$$

$$= \frac{1}{\sigma} (1 + j)$$

$$= \frac{\sqrt{2}}{\sigma} \angle \pi/4 \qquad \ldots\ldots\ldots 18$$

Hence

$$p_z = \frac{1}{2}\sigma \frac{E_{ro}^2}{\sqrt{2}} \exp(-2z/\delta) \cos \pi/4$$

$$= \frac{1}{4}\sigma \frac{E_{ro}^2}{\sqrt{2}} \exp(-2z/\delta) \ W/m^2 \qquad \ldots\ldots\ldots 19$$

The total power loss, P, in the direction of the current, in a cylinder of radius R is the power crossing the conductor surface which is given by

$$P = \int_0^{2\pi} \int_0^R \left[\frac{\sigma E_{ro}^2}{4} \exp(-2z/\delta) \right]_{z=0} r \, dr \, d\theta \quad \text{watts}$$

$$= \pi\sigma \frac{\delta E_{ro}^2}{4} R^2$$

$$= \pi\sigma \frac{\delta J_{ro}^2}{4\sigma} R^2 \qquad \ldots\ldots\ldots 20$$

(Since $J_{ro} = \sigma E_{ro}$)

If the total current were distributed uniformly in one skin depth, then the current I is the integral of J_r over the entire depth of the conductor

$$I = \int_0^R \int_0^\infty J_r \, dr \, dz \qquad \ldots\ldots\ldots 21$$

and since J_r is the same form as E_r then

$$J_r = J_{ro} \exp(-z/\delta) \cos(\omega t - z/\delta)$$

In complex exponential form,

$$J_r = J_{ro} \exp(-z/\delta) . \exp(-jz/\delta)$$

$$= J_{ro} \exp(-z(1 + j)/\delta) \qquad \ldots\ldots\ldots 22$$

Therefore

$$I = \int_0^{\infty} \int_0^{2\pi} J_{ro} \exp(-z(1+j)/\delta) R \, d\theta \, dz$$

$$= 2\pi J_{ro} \exp(-z(1 + j)/\delta) \frac{-\delta}{(1 + j)} \Bigg]_0^{\infty}$$

$$= \frac{2\pi R \delta J_{ro}}{(1 + j)} \qquad \ldots\ldots\ldots 23$$

Hence

$$I = \frac{2\pi R \delta J_{ro}}{\sqrt{2}} \cos(\omega t - \pi/4) \qquad \ldots\ldots\ldots 24$$

Equation 24 establishes the relationship between I and J_r.

Now ohmic power loss per unit volume is J^2/σ, and the time average power loss in a cylindrical slab of radius R and thickness δ is

$$P = \int \frac{J_r^2}{\sigma} \, dv$$

$$= \int_0^R \int_0^{2\pi} \int_0^{\delta} \frac{J_{ro}^2}{2\sigma} \cos^2(\omega t - \pi/4) \; r \, dr \, d\theta \, dz$$

$$= \frac{J_{ro}^2}{4\sigma} \pi R^2 \delta \quad \text{watts} \qquad \ldots\ldots\ldots 25$$

This power loss is the same as that in equation 20 and the current density may be considered to exist only in the first skin depth, and to be uniform throughout that region.

APPENDIX B

THEORY OF ELECTROKINETIC EFFECTS

In electrokinetics, the electric charges on two surfaces in contact determine their relative motion in an electric field. The effects produced in the model may be explained on the basis of electrocapillary action, which is the change in surface tension of the interface between two liquids, due to the application of an electrical potential. The simple theory of electrocapillarity is as follows (20, 21). The superficial electronic charge density on the mercury interface is q. This is a positive charge since thermodynamically, a metal in contact with an aqueous solution loses electrons. Because of the presence of an electrical double layer, the interface is analagous to a parallel plate condenser, with a potential difference v between the plates. The work required to increase the charge on the plates by dQ is v.dQ. Work is also required to increase the area, due to surface tension forces, hence the total work dW (reversible) is

$$dW = \gamma\, dA + v.dQ \qquad \ldots\ldots\ldots 1$$

Since dW is a complete differential, then

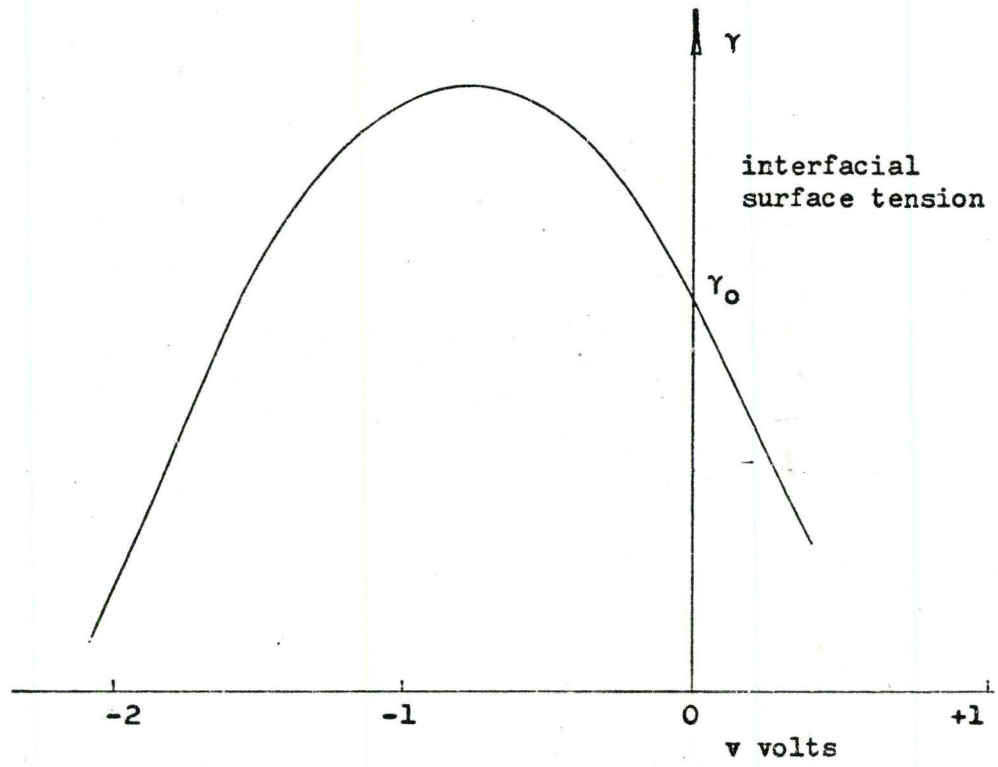

(a) The Electrocapillary Curve

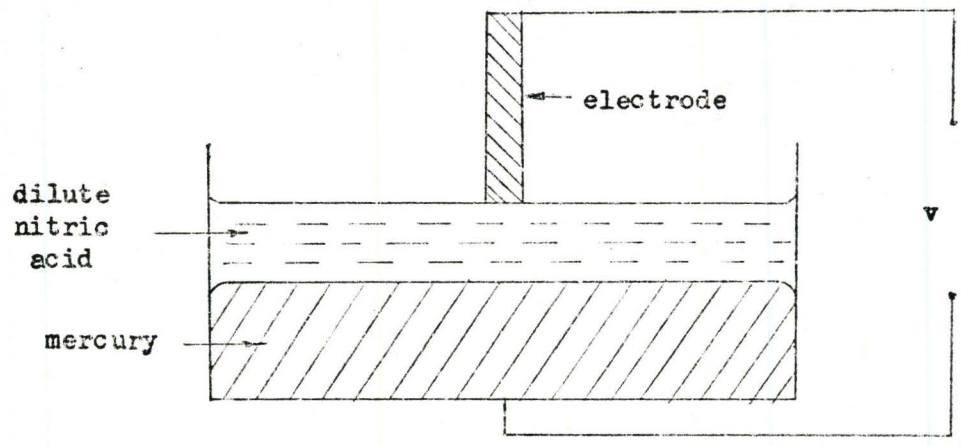

(b) Production of the Electrocapillary Curve

Fig. B1: The Electrocapillary Curve

$$\left[\frac{\partial \gamma}{\partial v}\right]_A = -\left[\frac{\partial Q}{\partial A}\right]_v = -q \qquad \ldots\ldots\ldots 2$$

This is the fundamental equation of electrocapillarity, and is named the Lippmann equation, in honour of its discoverer. It infers also that if the expansion or contraction of a surface causes a flow of electric charge towards or away from it, then the interfacial tension is dependent on the applied voltage. The relationship applies equally well to any two liquid media. The graph of this relationship, termed the electrocapillary curve, is shown in Fig. B1. It may be noted that the slope of the curve is numerically equal to the surface charge density, q. Experimentally, it has been shown that the shape of the curve is a function of the nature of the metal phase and the concentration of the aqueous solution, but is independent of the absolute value of potential or the nature of the electrode.

Action of the mercury surface beneath an electrode, may be deduced from the electrocapillary curve. Fig. B2 shows the development of oscillatory forces in the surface of the mercury, leading to the production of standing waves if an alternating current is applied between the electrode and the mercury. Fig. B3 shows the possible action on the application of direct current to the system.

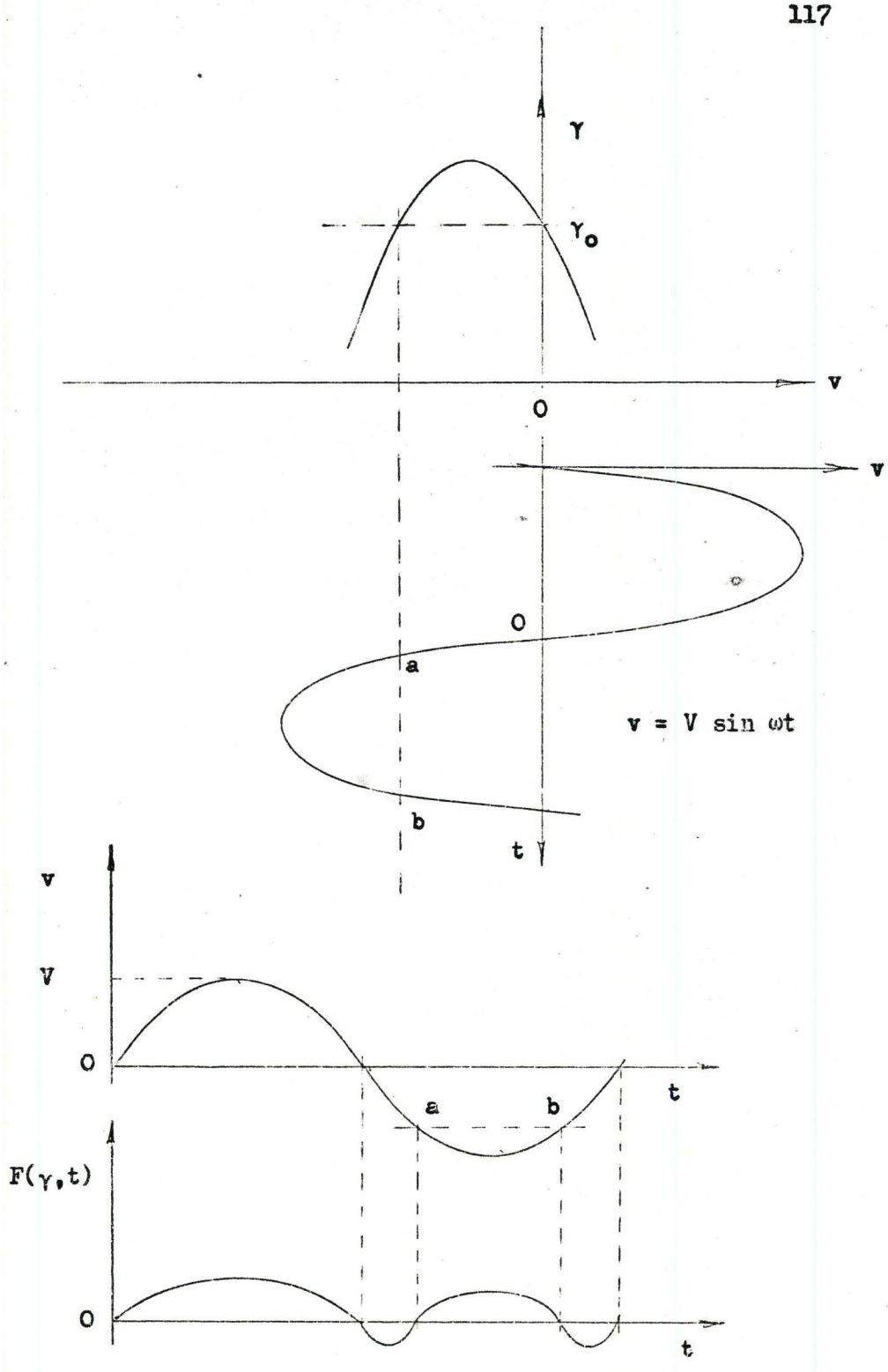

$F(\gamma,t)$ is surface force due to change in γ

Fig. B2: Production of Surface Oscillations by Alternating Current

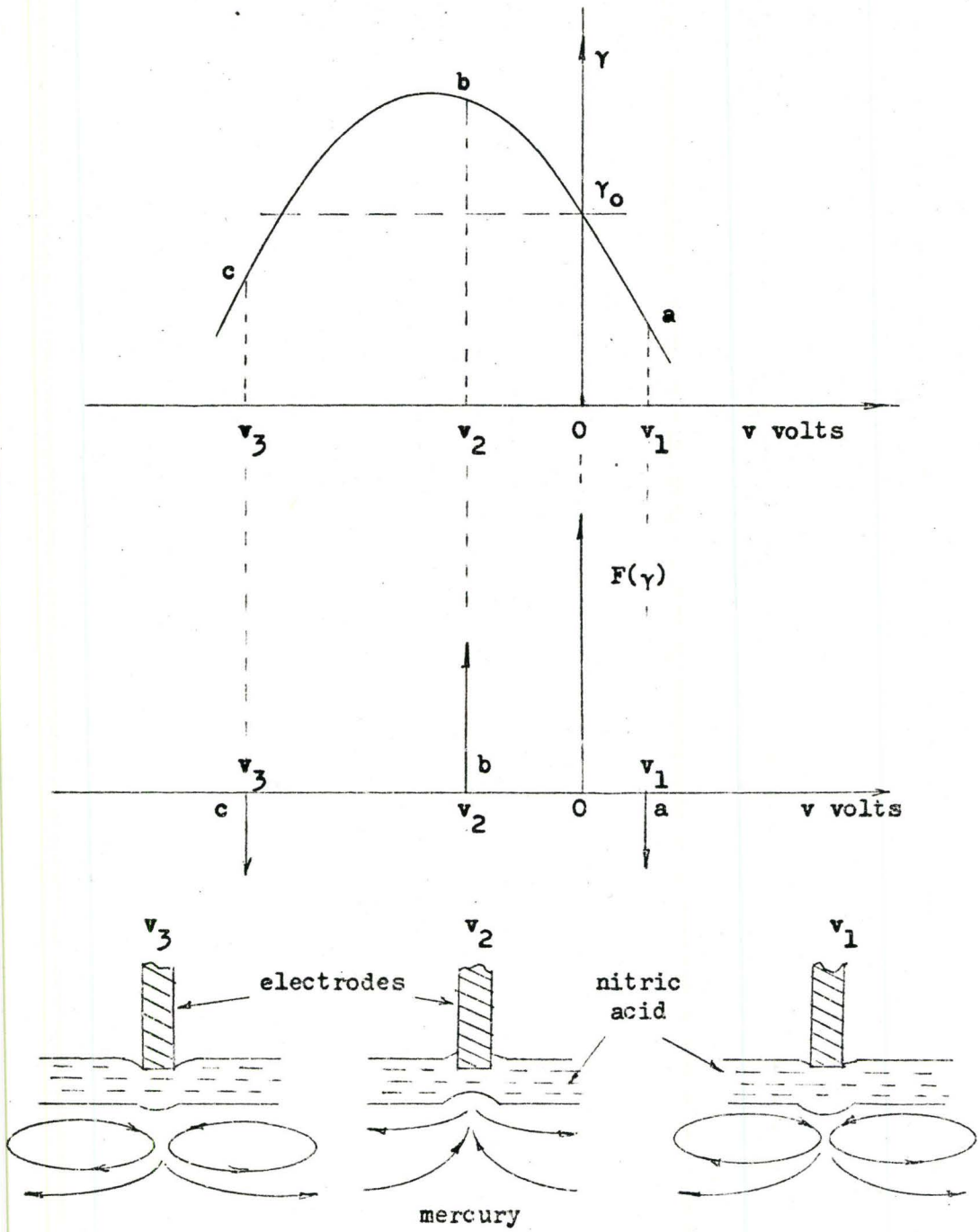

Fig. B3: Movements of Mercury Surface by Electrocapillary Action Using Direct Current

APPENDIX C

RECORD OF CURRENT DENSITY MEASUREMENTS

This appendix lists the current density measurements taken on the model.

CURRENT DENSITY MEASUREMENTS

Model = 2-phase; Electrode Current = 100 A/phase; Frequency = 400 hz; Probe used = Nº 2; Phase Sequence = ADBC; Phase angle with respect to V_{AD}; V_A = V 0°; V_B = V 90°; Electrodes 'A' at θ = 0°; 'O' at θ = 90°

	r = 0 inch				r = 1.0 inch		
θ°	J A/m² x 10^4	∅°	β°	θ°	J A/m² x 10^4	∅°	β°
45°	0.006	0		10	5.35	-45	180° lead
	2.54	30	45° lead	30	5.13	-84	200
	3.16	45	50	45	4.8	-90	200
	3.50	60	50	60	4.8	-102	200
	4.25	90	50	80	4.9	-135	200
	3.84	120	45	350	4.58	0	180
	3.16	135	45	330	4.0	30	180
	2.2	150	45	315	3.3	90	110
	0.013	180	-	300	3.9	150	75
	2.47	210	135° lag	280	5.0	180	70
	3.43	225	135				
	4.12	240	135				
	4.53	270	135				
	3.84	300	135				
	2.26	330	135				

Model = 2-phase; f = 400 hz; Phase Sequence = ADBC

r = 2.0 inches				r = 3.0 inches			
θ°	J A/m^2 x 10^4	ϕ°	β°	θ°	J A/m^2 x 10^4	ϕ°	β°
20	7.68	-60	180	0	2.26	0	0
30	5.49	-102	170 lag	30	2.74	72	20° lead
45	4.94	-90	160	45	2.74	90	20
60	5.49	-90	170	60	2.81	90	20
70	7.54	-90	180	90	3.02	108	180° lag
110	7.41	-102	40	120	1.74	72	200° lag
120	3.77	-102	40	135	1.37	90	210
135	2.74	-90	60	150	1.51	114	120
150	3.77	-90	90	180	3.07	180	65° lead
160	7.96	-90	120	200	2.74	-120	70
200	6.58	-90	65 lead	225	2.40	-90	70
210	5.01	-90	65	240	2.61	-78	70
225	4.66	-90	65	270	2.95	0	70
290	4.12	-84	45 lag	300	1.37	60	120
315	2.26	-90	45	315	1.10	90	135
340	5.9	-90	45	330	1.17	120	165

r = 4.0 inches				r = 5.0 inches			
θ°	J A/m^2 x 10^4	ϕ°	β°	θ°	J A/m^2 x 10^4	ϕ°	β°
0	1.1	42	30° lead	0	0.82	72	45° lead
30	1.71	78	20	30	1.44	90	30
45	1.85	90	20	45	1.58	90	30
60	1.85	96	20	60	1.58	90	30
90	1.37	126	20	90	0.96	90	40
120	0.96	-48	120° lag	120	0.48	90	100
135	0.96	-90	90	135	0.55	90	135
150	0.96	-48	90	150	0.55	90	170
180	1.03	-144	60° lead	180	1.17	78	135° lag
200	1.51	-120	60	200	1.65	90	120
225	1.65	-90	60	225	1.85	90	120
240	1.65	-90	60	240	1.78	90	155
270	1.1	-180	90° lag	270	1.1	90	135
300	6.82	-144	90	300	0.55	90	160° lead
315	0.82	-90	80	315	0.55	90	135
330	0.82	-135	120	330	0.55	90	110 lead

θ°	J A/m^2 x 10^4	ϕ°	β°	θ°	J A/m^2 x 10^4	ϕ°	β°
0	1.1	42	30° lead	0	0.82	72	45° lead
30	1.71	78	20	30	1.44	90	30
45	1.85	90	20	45	1.58	90	30
60	1.85	96	20	60	1.58	90	30
90	1.37	126	20	90	0.96	90	40
120	0.96	-48	120° lag	120	0.48	90	100
135	0.96	-90	90	135	0.55	90	135
150	0.96	-48	90	150	0.55	90	170
180	1.03	-144	60° lead	180	1.17	78	135° lag
200	1.51	-120	60	200	1.65	90	120
225	1.65	-90	60	225	1.85	90	120
240	1.65	-90	60	240	1.78	90	135
270	1.1	-180	90° lag	270	1.1	90	135
300	0.82	-144	90	300	0.55	90	160° lead
315	0.82	-90	80	315	0.55	90	135
330	0.82	-135	120	330	0.55	90	110° lead

Model = 2-phase; f = 400 hz; Input current = 100 A/phase; Probe used = No 2; Phase B in position

r = 0.0 inch				r = 1.0 inch			
θ	J A/m^2 x 10^4	ϕ°	β°	θ°	J A/m^2 x 10^4	ϕ°	β°
45°	3.56	0	5° lead	10	6.17	-48°	85° lag
	3.64	30	30	30	5.35	-72	90
	3.91	60	63	45	5.08	-90	100
	4.11	90	90	60	5.21	-114	110
	4.11	120	120	80	6.17	-150	135
	3.84	150	150	90	5.76	-	
	3.77	180	190	280	6.04	0	65
	3.97	210	145° lag	300	5.01	48	45
	4.18	240	120	315	4.46	90	0
	4.25	270	90	330	4.53	138	20° lead
	4.05	300	65	350	5.76	168	30
	3.77	330	36				

Model = 2-phase; f = 400 hz; phase sequence = ABDC

r = 2.0 inches				r = 3.0 inches			
θ°	J A/m^2 x 10^4	ϕ°	β°	θ°	J A/m^2 x 10^4	ϕ°	β°
20	10.29	84	100° lead	0	2.6	0	120° lead
30	5.49	84	90	20	2.4	60	100
45	4.0	90	90	30	2.3	78	100
60	4.0	90	80	45	2.2	90	90
70	4.7	96	65	60	2.2	102	80
290	12.3	90	20	70	2.26	114	80
300	5.8	90	10	90	2.26	180	45
315	3.91	90	0	270	2.7	-180	135° lag
330	4.60	90	20° lag	290	2.3	-120	190° lead
340	5.76	90	45	300	2.2	-102	185
				315	2.2	-90	180
				330	2.2	-72	170
				340	2.26	-60	155

r = 4.0 inches				r = 5.0 inches			
θ°	J A/m^2 x 10^4	ϕ°	β°	θ°	J A/m^2 x 10^4	ϕ°	β°
0	1.37	72	80° lead	0	0.96	90	10° lead
20	1.37	78	80		1.1	90	36
30	1.37	90	90		1.23	90	45
45	1.51	90	90		1.3	90	54
60	1.51	90	100		1.23	90	63
70	1.51	90	100		1.17	90	70
90	1.37	114	120		1.1	90	90
270	1.37	-72	110		1.23	-90	90
290	1.4	-78	150		1.37	-90	110
300	1.51	-90	160		1.4	-90	125
315	1.58	-90	170		1.51	-90	135
330	1.51	-90	180		1.4	-90	150
340	1.58	-66	180		1.37	-90	160

VARIATION OF CURRENT DENSITY J with Depth z Below Surface of Model

Probe = № 3; Input Current = 100 A/phase

3-electrode model $\theta = 60^\circ$; $\phi = 90^\circ$; r = 2.0 inches

	frequency = 60 hz				frequency = 1000 hz	
z inches	J A/m^2 x 10^4	β°	J A/m^2 x 10^4	β°	J A/m^2 x 10^4	β°
0	1.44	45° lead	2.58	37° lead	4.80	0°
0.2	1.44	45	2.15	18	3.55	18° lag
0.4	1.44	45	1.87	0	2.70	27
0.6	1.29	45	1.51	12° lag	1.90	54
0.8	1.29	40	1.29	23	1.40	72
1.0	1.15	30	1.00	36	1.10	90
1.2	1.15	27	0.93	54	0.90	99
1.4	1.08	27	0.79	63	0.80	108
1.6	1.0	27	0.79	72	0.70	120
1.8	1.0	27	0.72	75	0.62	124
2.0	1.0	27	0.72	75	0.55	126
2.1 (=max)	0.93	27	0.72	75	0.50	130

Model = 3-phase; Electrode Current = 100 A/phase; Frequency = 60 hz; Probe used = Nº 1; Phase B in position $\theta = 0^{\circ}$; Phase Sequence ABC; Phase angle B with respect to Voltage V_{BN}

	r = 0.0 inch				r = 1.0 inch		
θ°	J A/m^2 x 10^4	ϕ°	β°	θ°	J A/m^2 x 10^4	ϕ°	β°
45°	1.6	0	135° lead	10	3.5	174	0
	1.6	30	120	20	3.2	156	9° lead
	1.6	69	85	30	2.8	138	18
	1.6	90	60	40	2.5	120	20
	1.6	120	23	50	2.4	108	27
	1.6	144	0	60	2.4	90	36
	1.6	150	20° lag	70	2.4	78	45
	1.6	180	45	80	2.7	72	50
	1.6	210	75	90	3.0	60	54
	1.6	240	100	100	3.5	48	54
	1.6	270	130	110	3.9	24	60
	1.6	300	160				
	1.6	330	190				

Model = 3-phase; Electrode Current = 100 A/phase; Frequency = 60 hz; Probe used = Nº 1; Phase B is position; $\theta = 0^{\circ}$; Phase Sequence ABC; Phase angle β with respect to voltage V_{BN}

	r = 2.0 inches			r = 3.0 inches		
θ°	J A/m^2 x 10^4	ϕ°	β°	J A/m^2 x 10^4	ϕ°	β°
0	-			2.8	0	0
10				2.5	24	0
20	7.0	103	0	1.8	42	9° lead
30	3.3	102	9° lead	1.4	60	27
40	2.3	102	18	1.3	78	27
50	1.8	102	27	1.2	90	30
60	1.8	96	40	1.1	90	30
70	1.9	90	45	1.2	102	36
80	2.3	102	54	1.2	114	36
90	3.5	102	54	1.4	120	36
100	7.4	108	60	1.8	144	54
110				2.4	162	54
120				2.8	180	60

	r = 4.0 inches			r = 4.5 inches		
θ°	J A/m^2 x 10^4	ϕ°	β°	J A/m^2 x 10^4	ϕ°	β°
0	0.5	0	0	0.3	0	0
10	0.6	60	45° lead	0.4	90	60° lead
20	0.6	84	45	0.45	90	50
30	0.7	90	36	0.6	90	40
40	0.7	90	36	0.6	90	36
50	0.7	90	36	0.6	90	36
60	0.75	90	30	0.6	90	36
70	0.7	90	36	0.6	90	36
80	0.7	90	36	0.6	90	36
90	0.7	90	36	0.6	90	36
100	0.7	132	36	0.45	90	36
110	0.6	150	45	0.4	120	18
120	0.5	180	60	0.3	138	0

Model = 3-phase; Electrode current = 100 A/phase; Frequency = 400 hz;

Probe used = № 1; Phase B in position $\theta = 0^{\circ}$; Phase sequence ABC

Phase angle β with respect to V_{BN}

	r = 4.0 inches			r = 5.0 inches		
θ°	J A/m^2 x 10^4	ϕ°	β°	J A/m^2 x 10^4	ϕ°	β°
0	1.1	0	9° lead	0.6	0	0
10	1.2	42	36	1.0	60° lead	60° lead
20	1.4	66	36	1.2	84	54
30	1.45	84	36	1.2	90	45
40	1.5	90	36	1.4	90	45
50	1.5	90	36	1.4	90	40
60	1.4	90	36	1.4	90	40
70	1.4	102	36	1.35	90	36
80	1.3	108	36	1.25	96	36
90	1.2	120	36	1.15	114	36
100	1.1	132	36	1.0	114	36
110	1.0	150	45	0.8	96	0
120	0.8	180	75	0.8	72° lag	45° lag

Model = 3 phase; Electrode current = 100 A/phase; Frequency = 400 hz; Probe used = N^{o} 1; Phase B in position $\theta = 0^{\circ}$; Phase sequence ABC; Phase angle β with respect to V_{BN}

	r = 0.0 inch				r = 1.0 inch		
θ°	J A/m^2 x 10^4	ϕ°	β°	θ°	J A/m^2 x 10^4	ϕ°	β°
60°	3.4	0	150° lead	10	6.5	168	9° lead
	3.4	30	125	20	5.5	150	22
	3.4	60	100	30	4.7	138	30
	3.4	90	70	40	4.4	126	36
	3.4	120	50	50	4.2	108	45
	3.4	150	0	60	4.1	90	54
	3.4	180	35° lag	70	4.3	90	54
	3.4	210	60	80	4.6	84	54
	3.4	240	90	90	5.2	72	60
	3.4	270	125	100	6.2	66	60
	3.4	300	150	110	7.0	48	60
	3.4	330	185				
	3.4	360	210				

	r = 2.0 inches			r = 3.0 inches		
θ°	J A/m^2 x 10^4	ϕ°	β°	J A/m^2 x 10^4	ϕ°	β°
0				2.7	0	0
10				2.65	30	18° lead
20	6.7	90	5° lead	2.4	54	24
30	4.0	96	27	2.2	72	36
40	3.4	90	36	2.0	84	40
50	3.1	90	45	1.9	90	40
60	3.1	90	45	1.9	90	45
70	3.1	90		1.9	90	50
80	3.4	90		1.9	108	54
90	4.0	90		2.0	120	54
100	6.7	90		2.3	138	60
110				2.6	162	60
120				2.8	180	63

(Model = 3 phase; Electrode current = 100 A/phase; Frequency = 400 hz.)

Variation of current density J with Input current I and frequency f.

3-electrode model

$r = 3.0$ inches; $\theta = 0^{\circ}$; $\phi = 0^{\circ}$

I Amps	$J \times 10^4$ 60 hz	$J \times 10^4$ 400 hz	$J \times 10^4$ 1000 hz	$J \times 10^4$ 2000 hz	$J \times 10^4$ 4000 hz
40	0.8	1.0	1.6	2.6	5.0
60	1.2	1.6	2.6	3.8	
80	1.6	2.1	3.5	5.0	
100	1.8	2.4	3.8	6.25	
120	2.2	2.9	4.5		
140	2.6	3.4	5.2		
160	3.0	3.9			
200	3.6	4.8			

Variation of current density J with Input current I and frequency f.

4-electrode model

$r = 1.0$ inch; $\theta = 30^{\circ}$

I Amps	$J \times 10^4$ 60 hz	$J \times 10^4$ 100 hz	$J \times 10^4$ 400 hz	$J \times 10^4$ 1000 hz	$J \times 10^4$ 2000 hz	$J \times 10^4$ 3000 hz
40	1.51	1.51	2.33	3.7	5.76	8.23
60	2.13	2.2	3.43	5.42	8.5	
80	2.74	2.9	4.4	7.13	11.11	
100	3.5	2.57	5.49	8.78		
120	4.11	4.32	7.27	10.42		
140	4.8	4.94	7.68	12.34		
180	6.17	6.51	10.01			

GLOSSARY OF MAIN TERMS

SYMBOL	NAME	UNIT
A	Surface Area	Metre^2
B	Flux Density	Weber/metre^2
C_I	Current Scaling Factor	-
C_J	Current Density Scaling Factor	-
C_s	Size Scaling Factor	-
D	Electric Flux Density	Coulomb/metre^2
E	Electric Field Intensity	Volts/metre
f	Frequency	Hertz
F	Force	Newton
g	Acceleration due to Gravity	Metre/sec^2
H	Magnetic Field Intensity	Amperes/metre
I	Current	Amperes
J	Current Density	Amperes/metre^2
ℓ	Length	Metre
N_R	Reynolds Number	-
N_F	Froude Number	-
P	Power	Watts
p	Instantaneous Power	Watts
q	Surface Charge Density	Coulomb/metre^2
Q	Charge	Coulomb

SYMBOL	NAME	UNIT
R_C	Radius of Electrode Circle	Metre
R_F	Radius of Furnace	Metre
T	Temperature	^oC
t	Time	Second
v	Voltage	Volts
V	Velocity	Metre/sec
W	Work	Joule
α	Temperature Coefficient of Conductivity	$^oC^{-1}$
β	Phase Angle	Degrees
γ	Surface Tension	Newton/metre
δ	Skin Depth	Metre
ϵ	Permittivity	Farads/metre
θ	Cylindrical Co-ordinate	Radians
μ	Permeability	Henry/metre
ν	Viscosity	Newton-sec/metre^2
σ	Electrical Conductivity	Mho/metre
ϕ	Angular Position	Radians
ω	Angular Velocity	Radians/sec
η	Intrinsic Impedance	Ohm

REFERENCES

1. H.A. Mulcahy and G.H. Samuel, "Lake Ontario Steel's Computer Controlled Electric Arc Meltshop," Blast Furnace and Steel Plant, Vol. 58, pp. 201-205, November 1970.

2. United States Steel Company, The Making, Shaping and Treating of Steel. Pittsburgh: Herbick and Held, 1970, pp. 553-555.

3. Committee, Physical Chemistry of Steelmaking, A.I.M.E., Electric Furnace Steelmaking, Vol. 1. New York: Interscience Publishers, 1963, p. 7.

4. W.E. Schwabe, "Ultra High Power Arc Furnaces," Iron and Steel Engineer, Vol. 46, September 1969.

5. H.F. Walther, "Induction Stirring Provides Better Control of Operating Techniques," Journal of Metals, Vol. 6, pp. 21-23, January 1954.

6. J.A. Ciotto, "A New Era in Melting," Journal of Metals, Vol. 23, pp. 30-35, April 1971.

7. R.T.H. Alden, P.E. Burke, P.P. Biringer, "M.H.D. Pumping in Channel Furnaces," I.E.E.E. Winter Power Meeting, New York, Paper No. 70 CP 209-PWR, January 1970.

8. R.T.H. Alden, "Flow in a Channel Furnace," Ph.D. Thesis, University of Toronto, 1968.

9. A.S. Mikulinskii, "Criteria of Electric Ore-Smelting Furnaces," Electric Technology U.S.S.R., Vol. 2, pp. 256-271, March 1961.

10. G.A. Sisoyan, "The Current Distribution in the Baths of Ore-Smelting Furnaces," Electric Technology U.S.S.R., Vol. 3, pp. 460-475, February 1961.

11. J.D. Lavers, "Current, Force and Velocity Distribution in the Coreless Induction Furnace," Ph.D. Thesis, University of Toronto, 1970.

12. W.D. Stephenson, Elements of Power Systems Analysis. New York: McGraw-Hill, 1962, pp. 76-77.

13. W.F. Hughes and J.A. Brighton, Fluid Dynamics. New York: McGraw-Hill, 1967, pp. 64-67.

14. P.E. Burke and R.T.H. Alden, "Current Density Probes," Trans. I.E.E.E., Vol. PAS-88, pp. 181-184, February 1969.

15. W.E. Schwabe, "Fundamentals of Heat Distribution and Refractory Wear," Iron and Steel Engineer, Vol. 38, pp. 1048-1054, December 1961.

16. W.E. Schwabe, "Arc Heat Transfer and Refractory Erosion in Electric Steel Furnaces," A.I.M.E., Electric Furnace Proceedings, Vol. 20, pp. 195-206, 1960.

17. E. Della Torre and V. Longo, The Electromagnetic Field. Boston: Allyn and Bacon Inc., 1969, pp. 619-623.

18. W.H. Hayt, Jr., Engineering Electromagnetics. New York: McGraw-Hill, 1967, pp. 325-330.

19. E.R. Landry, "Recent Developments in Electric Arc Furnace Technology," Canadian Mining and Metallurgical Bulletin, Vol. 60, pp. 923-928, August 1967.

20. J.T. Davies and E.K. Rideal, Interfacial Phenomena. New York: Academic Press Inc., 1961, pp. 98-100.

21. J.J. Bikerman, Surface Chemistry for Industrial Research. New York: Academic Press Inc., 1948, pp. 411-415.

22. Staff, Journal of Metals, "New Electroslag Remelting Facility at Carpenter Technology in Reading, Pa.," Journal of Metals, Vol. 24, pp. 20-22, January 1972.